

REPORT DOCUMENTATION PAGE				Form Approved OMB No. 0704-0188	
The public reporting burden for this collection of information is estimated to average 1 hour per response, including the time for reviewing instructions, searching existing data sources, gathering and maintaining the data needed, and completing and reviewing the collection of information. Send comments regarding this burden estimate or any other aspect of this collection of information, including suggestions for reducing the burden, to Department of Defense, Washington Headquarters Services, Directorate for Information Operations and Reports (0704-0188), 1215 Jefferson Davis Highway, Suite 1204, Arlington, VA 22202-4302. Respondents should be aware that notwithstanding any other provision of law, no person shall be subject to any penalty for failing to comply with a collection of information if it does not display a currently valid OMB control number.					
PLEASE DO NOT RETURN YOUR FORM TO THE ABOVE ADDRESS.					
1. REPORT DATE (DD-MM-YYYY) 25-07-2011		2. REPORT TYPE Final		3. DATES COVERED (From - To) 06/01/2007 - 05/31/2011	
4. TITLE AND SUBTITLE (GameChanger) Multifunctional Design of Hybrid Composites of Load Bearing Antennas				5a. CONTRACT NUMBER	
				5b. GRANT NUMBER FA 9550-07-1-0462	
				5c. PROGRAM ELEMENT NUMBER	
				5d. PROJECT NUMBER	
6. AUTHOR(S) J.L. Volakis, Y. Bayram, K. Sertel, S. Ghosh, S. Bechtel, G. Washington, M. Shtein, N. Kotov R. James, G. Carman				5e. TASK NUMBER	
				5f. WORK UNIT NUMBER	
7. PERFORMING ORGANIZATION NAME(S) AND ADDRESS(ES) The Ohio State University 1320 Kinnear Rd. Columbus, OH 43212				8. PERFORMING ORGANIZATION REPORT NUMBER 60012388-4	
9. SPONSORING/MONITORING AGENCY NAME(S) AND ADDRESS(ES) B. L. ("Les") Lee, ScD Program Manager for Mechanics of Multifunctional Materials & Microsystems Air Force Office of Scientific Research 875 N. Randolph Street, AFOSR/NA, Suite 325, Room 3112, Arlington, VA 22203 email: ByungLip.Lee@afosr.af.mil or Les.Lee@afosr.af.mil				10. SPONSOR/MONITOR'S ACRONYM(S) AFOSR/NA	
				11. SPONSOR/MONITOR'S REPORT NUMBER(S) AFRL-OSR-VA-TR-2012-0467	
12. DISTRIBUTION/AVAILABILITY STATEMENT Basic Research Report: Distribution Unlimited					
13. SUPPLEMENTARY NOTES					
14. ABSTRACT Under this AFOSR GameChanger we carried out groundbreaking research by developing methods and materials to realize small and conformal structurally integrated antennas for unmanned airborne vehicles (UAVs). We are proud to report several groundbreaking developments in all areas. Among them we (a) developed a conformal, load-bearing antenna technology by embroidering e-fibers on polymer composites, (b) Characterized performance of the e-fibers in terms of core and specific strength for load-bearing applications, (c) Developed a new principles DFT method for systematic search of ferromagnetic, low conductivity nanowires, (d) Developed a strategy for increasing permittivity and permeability proportionately using magnetic nanowires combined with conventional high contrast materials for antenna miniaturization, (e) demonstrated theoretical feasibility of laminate EM materials that alter wave propagation characteristics, critical to future miniaturization efforts, (f) Developed a multi-time scaling model and algorithm for coupling mechanical and EM solutions in real time, critical to multiphysics coupled EM-Structural analysis, (g) Extended low-frequency domain decomposition algorithm to 2-D passive and characterized more complex/intricate details on large platforms					
15. SUBJECT TERMS load-bearing antennas, conformal antennas, miniature antennas, e-textiles, e-fibers, embroidered antennas, flexible RF electronics on polymers, ferromagnetics, multiferroics, multiphysics computational tools, nanowires, laminate electromagnetic materials for miniaturization, domain decomposition multiphysics analysis methods, piezoelectrics and field generation.					
16. SECURITY CLASSIFICATION OF:			17. LIMITATION OF ABSTRACT		18. NUMBER OF PAGES
a. REPORT Unclassified	b. ABSTRACT unclassified	c. THIS PAGE			19a. NAME OF RESPONSIBLE PERSON
					19b. TELEPHONE NUMBER (Include area code)



# **(GameChanger) Multifunctional Design of Hybrid Composites of Load Bearing Antennas**

Grant No: FA 9550-07-1-0462

**Final Report  
June 2011**

**PI: John L. Volakis ([volakis@ece.osu.edu](mailto:volakis@ece.osu.edu))**

**POC: Dr. B.L. (“Les”) Lee ([Byung-Lip.Lee@afosr.af.mil](mailto:Byung-Lip.Lee@afosr.af.mil))**

---

## **ABSTRACT**

Under this AFOSR GameChanger we carried out groundbreaking research by developing methods and materials to realize small and conformal structurally integrated antennas for unmanned airborne vehicles (UAVs). We are proud to report several groundbreaking developments in all areas. Among them we (a) developed a conformal, load-bearing antenna technology by embroidering e-fibers on polymer composites, (b) Characterized performance of the e-fibers in terms of core and specific strength for load-bearing applications, (c) Developed a *new principles* DFT method for systematic search of ferromagnetic, low conductivity nanowires, (d) Developed a strategy for increasing permittivity and permeability proportionately using magnetic nanowires combined with conventional high contrast materials for antenna miniaturization, (e) demonstrated theoretical feasibility of laminate EM materials that alter wave propagation characteristics, critical to future miniaturization efforts, (f) Developed a multi-time scaling model and algorithm for coupling mechanical and EM solutions in real time, critical to multiphysics coupled EM-Structural analysis, (g) Extended our new domain decomposition algorithm to 3-D space and characterized more complex/intricate details on large platforms such as e-fibers embroidered on UAV platforms. In addition to this report, our ground breaking work under this program has been published in over 120 journal papers and over 70 conference summaries.

<b>SUMMARY OF ACCOMPLISHMENTS.....</b>	<b>3</b>
ANTENNAS AND RF SYSTEMS: .....	3
MATERIALS AND COMPOSITES: .....	3
MULTIPHYSICS/MULTISCALE ANALYSIS/DESIGN/OPTIMIZATION:.....	3
INTEGRATION AND TRANSITION: .....	3
<b>PROF. VOLAKIS' GROUP SUMMARY:.....</b>	<b>4</b>
E-FIBER EMBROIDERED ON POLYMER COMPOSITES .....	9
<b>PROF. ROJAS' GROUP SUMMARY .....</b>	<b>18</b>
<b>PROF. KOTOV'S GROUP SUMMARY .....</b>	<b>32</b>
RESEARCH SUMMARY.....	41
<b>PROF. SHTEIN'S GROUP SUMMARY.....</b>	<b>42</b>
<b>PROF. GHOSH'S GROUP SUMMARY .....</b>	<b>44</b>
<b>PROF. BECHTEL 'S GROUP SUMMARY .....</b>	<b>54</b>
<b>PROF. CARMAN'S GROUP SUMMARY .....</b>	<b>61</b>
RESEARCH SUMMARY.....	62
ANALYTICAL WAVE PROPAGATION MODELING: .....	63
DEVELOPMENT OF EFFECTIVE LAMINATE PROPERTIES: .....	68
FABRICATION, CHARACTERIZATION AND TESTING OF ME MATERIALS.....	70
<b>PROF. JAMES' GROUP SUMMARY.....</b>	<b>77</b>

## Summary of Accomplishments

### *Antennas and RF Systems:*

- Developed embroidered E-fiber – polymers for conformal, load bearing applications
- Developed , built and characterized 3-D volumetric E-fiber spiral antenna in collaboration with U of Michigan.
- Extended the 2-D Domain Decomposition Algorithms to 3-D domain and demonstrated their convergence for nanowires embedded within composites.

### *Materials and Composites:*

- Optimized process for e-fiber fabrication
- Characterized performance of e-fibers in regards core material and specific strength, conductance, twist multiplier etc.
- Developed conductive textiles based on CNT and copper sputtering on Kevlar
- Fabricated thin film magneto-electric structures
- Shown theoretical feasibility of laminate ME materials to significantly alter wave propagation characteristics
- Developed numerical techniques to characterize magnetic semiconductors and electromagnetic materials.
- Developed strategy for increasing  $\epsilon_r$   $\mu_r$  proportionately using magnetic nanowires combined with conventional high dielectric constant materials
- Developed low loss design principles by prediction of breakdown of the single domain state in nanowires
- Developed a new first principles DFT method for systematic search for ferromagnetic, low conductivity nanostructures, based on the concept of objective structures

### *Multiphysics/Multiscale Analysis/Design/Optimization:*

- Developed Coupled Electro-Magnetic and Dynamic Response codes
- Developed a multi-time scaling model and algorithm for coupling mechanical and EM solutions in real time
- Introduced high-performance parallel computational framework
- Multi-Scale-Super-Element which exploits shape functions derived from semi-analytical solutions in improving accuracy and enabling parameter studies for design and optimization problems

### *Integration and Transition:*

- Develop prediction formulae for dielectric constants as a function of temperature and stress (Correlated these parameters to antenna resonance and predicted resonance shift)
- Developed model for antenna performance under various conditions

## **Prof. Volakis' Group Summary:**

### **Students:**

Zheyu Wang (Ph.D., 2<sup>nd</sup> year), Tao Peng (Ph.D., 5<sup>th</sup> year),  
I. Tzanidis (Ph.D., completed Ph.D.)

### **Researchers:**

Yakup Bayram, Lanlin Zhang, Kubilay Sertel

## **Journal Papers Submitted/Published**

1. E. Apaydin, Y. Zhou, S. Koulouridis, J.L. Volakis and D.J. Hansford, "Composite Polymer Printing for RF Applications," submitted to *IEEE Trans. Microw. Theory Tech.*.
2. T. Peng, K. Sertel and J.L. Volakis, "Fully Overlapping Domain Decomposition Method for the Finite Element Modeling of Small Features," submitted to and under review at *IEEE Trans. Antenn. Propag.*.
3. S.E. Morris, Y. Bayram, J.L. Volakis and M. Shtein, "High-Strength, Metalized Fibers for Conformal Load Bearing Antenna Applications," to appear in *IEEE Trans. Antenn. and Propag.*, 2011.
4. T. Peng, S. Koulouridis and J.L. Volakis, "Miniaturization of Conical Helical Antenna via Optimized Coiling," accepted for publication at *J. Appl. Comput. Electrom.*.
5. I. Tzanidis, C.-C. Chen and J.L. Volakis, "Low Profile, Cavity-Backed Spiral on a Thin Ferrite Ground Plane for High Power Operation at 220-500 MHz," *IEEE Trans. Antenn. Propag.* vol. 58, no. 11, pp. 3715-3720, Nov. 2010.
6. Y. Zhou, Y. Bayram, F. Du, L. Dai and J.L. Volakis, "Polymer-Carbon Nanotube Sheets for Conformal Load Bearing Antennas," *IEEE Trans. Antenn. Propag.*, vol. 58, no. 7, pp. 2169-2175, Jul. 2010.
7. Y. Bayram, Y. Zhou, J.L. Volakis, B.-S. Shim, S. Xu, J. Zhu, N.A. Kotov and J.L. Volakis, "E-Textile Conductors and Polymer Composites for Conformal Lightweight Antennas," *IEEE Trans. Antenn. Propag.*, vol. 58, no. 8, pp. 2732-2736, Aug. 2010.
8. B.A. Kramer, C.-C. Chen, M. Lee and J.L. Volakis, "Fundamental Limits and Design Guidelines for Miniaturizing Ultra-Wideband Antennas," *IEEE Antenn. Propag. Magazine*, vol. 51, no. 4, pp. 57-69, Aug. 2009.
9. S. Koulouridis and J.L. Volakis, "A Novel Planar Conformal Antenna Designed with Splines," *IEEE Antenn. Wirel. Propag. Letters*, vol. 8, pp. 34-36, Apr. 2009.
10. F. Erkmen, C.-C. Chen and J.L. Volakis, "Impedance Matched Ferrite Layers as Ground Plane Treatments to Improve Antenna Wideband Performance," *IEEE Trans. Antenn. Propag.*, vol. 57, no. 1, pp. 263-266, Jan. 2009.
11. S. Koulouridis and J.L. Volakis, "L-band Circularly Polarized Small Aperture Thin Textured Patch Antenna," *IEEE Antenn. Wirel. Propag. Letters*, vol. 7, pp. 225-228, 2008.
12. L. Zhang, G. Mumcu, S. Yarga, K. Sertel, J.L. Volakis and H. Verweij, "Fabrication and Characterization of Anisotropic Dielectrics for Low-Loss Microwave Applications," *J. Mater. Sci.*, vol. 43, no. 5, pp. 1505-1509, 2008.
13. B.A. Kramer, C.-C. Chen and J.L. Volakis, "Size Reduction and a Low-Profile Spiral Antenna using Inductive and Dielectric Loadings," *IEEE Antenn. Wirel. Propag. Letters*, vol. 7, pp. 22-25, 2008.

14. F. Erkmén, C.-C. Chen and J.L. Volakis, "UWB Magneto-Dielectric Ground Plane for Low Profile Antenna Applications," *IEEE Antenn. Propag. Magazine*, vol. 50, no. 4, pp. 211-216, Aug. 2008.
15. S. Koulouridis, D. Psychoudakis and J.L. Volakis, "Multi-Objective Optimal Antenna Design Based on Volumetric Material Optimization," *IEEE Trans. Antenn. Propag.*, vol. 55, no. 3, pp. 594-603, Mar. 2007.

### Conference Papers Submitted/Published

1. Z. Wang, L. Zhang, Y. Bayram and J.L. Volakis, "Multilayer Printing of Embroidered RF Circuits on Polymer Composites," *IEEE International Symposium on Antennas and Propagation*, Spokane, WA, July, 2011.
2. T. Peng, K. Sertel and J.L. Volakis, "Higher Order Fully Overlapping Domain Decomposition Method," to be presented at *URSI-GASS 2011*, Istanbul, Turkey, Aug., 2011.
3. T. Peng, K. Sertel and J.L. Volakis, "The Convergence of Fully Overlapping Domain Decomposition Method," to be presented at *URSI-GASS 2011*, Istanbul, Turkey, Aug., 2011.
4. T. Peng, K. Sertel and J.L. Volakis, "Fully Overlapping Domain Decomposition Method with  $h$ -refinement for Finite Element Modeling of Small Features in Large Domains," to be presented at *IEEE International Symposium on Antennas and Propagation*, Spokane, WA, July, 2011.
5. L. Zhang, Z. Wang, Y. Bayram, J.L. Volakis, "Nanostructured Materials for Conformal RF Applications," to be presented at *IEEE International Symposium on Antennas and Propagation*, Toronto, Canada, July 2010.
6. Z. Wang, Y. Bayram, L. Zhang, J.L. Volakis, "Embroidered E-Fiber-Polymer Composites for Conformal and Load Bearing Antennas," to be presented at *IEEE International Symposium on Antennas and Propagation*, Toronto, Canada, July, 2010.
7. Y. Bayram, Feng Du, L. Dai, J.L. Volakis, "Surface Conditioned Carbon Nanotube Conductive Sheet for Flexible and Conformal Antennas," to be presented at *IEEE International Symposium on Antennas and Propagation*, Toronto, Canada, July, 2010.
8. T. Peng, K. Sertel and J.L. Volakis, "Fully Overlapping Domain Decomposition Method for Robust FEM Modeling of Fine Details in Large Host Media," *URSI National Radio Science Meeting*, Toronto, Canada, July, 2010.
9. Y. Zhou, Y. Bayram, L. Dai and J.L. Volakis, "Conformal Load-Bearing Polymer-Carbon Nanotube Antennas and RF Front-Ends," *IEEE APS/URSI International Symposium*, Charleston, SC, June 2009.
10. Y. Zhou, Y. Bayram, L. Dai, J.L. Volakis, "Conductive Polymer-Carbon Nanotube Sheets for Conformal Load Bearing Antennas," *URSI National Conference*, Boulder, CO, Jan., 2009
11. J.L. Volakis, K. Sertel, Y. Bayram "25 Years of Progress in Integral and Hybrid Finite Element Methods for Electromagnetics: from Analysis to Design," *Applied Computational Electromagnetics Conference*, Monterey, CA, March 2009
12. T. Peng, K. Sertel and J.L. Volakis, "Fully Overlapping Domain Decomposition Methods," *2009 USNC/URSI National Radio Science Meeting*, Charleston, SC, June, 2009.
13. T. Peng, K. Sertel and J.L. Volakis, "Fully Overlapping Domain Decomposition Method for Electromagnetic-Thermo-Mechanical Multi-Physics Computation," *10<sup>th</sup> US National Congress on Computational Mechanics*, Columbus, OH, July, 2009.

14. T. Peng, K. Sertel and J.L. Volakis, "A Fully Overlapping Domain Decomposition for Fast Optimization of Small Antennas in Large Scale Composite Media," *2009 Computational Electromagnetics International Workshop*, Izmir, Turkey, July, 2009.
15. T. Peng, K. Sertel and J.L. Volakis, "Fully Overlapping Domain Decomposition Method for Modeling Detailed Antenna Structures Embedded in Composite Host Media," *International Conference on Electromagnetics in Advanced Applications*, September, 2009.
16. I. Tzanidis, C.-C. Chen, J. L. Volakis, "Smaller UWB Conformal Antennas for VHF/UHF Applications with FerroDielectric Loadings," *APS-USNC/URSI, Session 424*, San Diego, CA, July 2008.
17. I. Tzanidis, S. Koulouridis, K. Sertel, D. Hansford and J.L. Volakis, "Characterization of Low-Loss Magnetodielectric Composites for Antenna Size Reduction," *APS-USNC/URSI, Session 522*, San Diego, CA, July 2008.
18. T. Peng, K. Sertel and J.L. Volakis, "Overlapping Domain Decomposition Finite Element Method for Modeling Intricate Detail in Natural and Engineered Host Media," *The 9th International Workshop on Finite Elements for Microwave Engineering*, Hamburg, Germany, May, 2008.
19. Y. Bayram, Y. Zhou, J.L. Volakis, B-S Shim and N. Kotov, "Conductive Textiles and Polymer-Ceramic Composites for Novel Load Bearing Antennas," *IEEE APS/URSI International Symposium*, San Diego, CA, July, 2008.
20. S. Koulouridis and J.L. Volakis, "Passive and Active Circuit Matching for VHF Antennas", *USNC-URSI, Session BS10*, Boulder, Co., Jan., 2008.
21. J.L. Volakis, K. Sertel and S. Ghosh, "Multiphysics Tools for Load Bearing Antennas Incorporating Novel Materials", *2<sup>nd</sup> European Conference on Antennas and Propagation (EuCAP 2007)*, Edinburgh, UK, Nov., 2007.
22. E. Apaydin, D. Hansford, S. Koulouridis and J.L. Volakis, "Integrated RF Circuits Design and Packaging in High Contrast Ceramic-Polymer Composites," *2007 IEEE Antennas and Propagation Society Conference*, Honolulu, Hawaii, USA, June, 2007.
23. I. Tzanidis, C.-C. Chen, D. Hansford and J.L. Volakis, "Spiral Antenna Miniaturization Using Variable Magnetic Material Loading", *USNC/URSI National Radio Science Meeting*, Ottawa, ON, Canada, July, 2007
24. I. Tzanidis, C.-C. Chen and J.L. Volakis, "Antenna miniaturization using impedance-matched ferrites", *2007 Antenna Measurement and Techniques Association (AMTA)*, St Louis, MO, November, 2007.

## Research Summary

A key development under the Gamechanger program is a new breakthrough technology based on embroidering E-fibers on polymer substrates for conformal and loadbearing antennas. As is already known, polymers provide for conformal, flexible, light-weight substrates that can be readily reinforced for load-bearing antennas on small UAVs and body worn applications. Electrically conductive fibers, comprised of thin metal coated polymer strands (Zylon, Kevlar etc.), are extremely flexible. They are also easy to stitch onto polymer substrates forming an embroidering structure. Also, the strands are extremely conductive (comparable with traditional conductors). Therefore, there is no noticeable compromise on the antenna performance and efficiency.

In this technology, polymer-ceramic composites serve as the host media (see Figure 1). E-fibers are then embroidered on the polymer to realize planar and volumetric antennas. Similarly, these fibers can also be used to form a grid ground plane for structural integration with the platform. In other words, these conductive and extremely strong fibers can be stitched into the platform for higher structural stability. An optional layer of non-conductive fiber such as Kevlar or Zylon can also be embedded inside the polymer composite to enhance structural ruggedness of the overall antenna structure (see Figure 1).

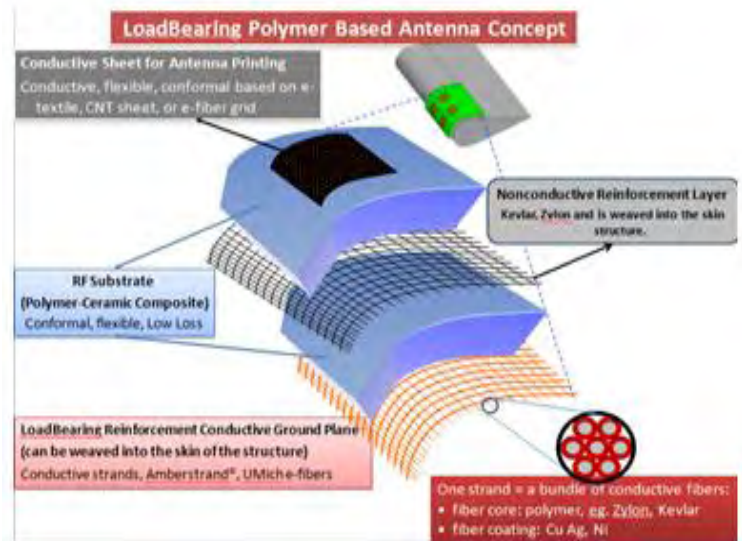


**Figure 1 Embroidered E-fiber polymer composite for load-bearing conformal antennas**

A key component of this technology is its low-cost, scalable and automated fabrication process for embroidering e-fibers on polymer composites. This is a game-changing technology whose realization will provide a new paradigm in load-bearing electronics and RF front ends. At this moment, we have only demonstrated the potential of the E-fiber embroidering technology. The next obvious and critical step is to control printing precision and realize multilayer low-loss (high efficiency) front end antenna arrays with electronic back-ends.

The unique aspects of our e-fiber embroidering technology are:

- Straightforward and easy to scale fabrication in room temperature
- Flexible, light-weight conformal, load bearing and extremely durable structure
- Chemically configurable polymer composite for higher permittivity and permeability metamaterials for antenna miniaturization

- Printed E-fiber can be flexed without concern about detachment and performance deterioration due to vibration and stretching.

In the final year of the GameChanger program, we continued to work closely with Max Shtein of University of Michigan to develop volumetric antennas using copper coated Kevlar yarns stitched into polymer substrate (see **Error! Reference source not found.**). Our previous efforts in coating Kevlar with copper resulted in a highly conductive yarn weaved into a polymer substrate. The final weaved antenna is extremely flexible and conformal to any surface of interest.

**Error! Reference source not found.** displays the

performance of a stitched volumetric spiral antenna with that of a traditional one made of copper wires on a ceramic substrate. We notice the remarkably good performance at frequencies above 700 MHz. At lower frequencies, the weaved e-fiber antenna experiences lower gain, primarily due to resistive losses on the copper coated Kevlar. In other words, at lower frequencies, more actual length of the wire is active to achieve radiation, leading to higher resistive losses. Such losses become less pronounced at higher frequencies since the antenna resonance is achieved using relatively shorter e-fiber lengths. Clearly higher conductivity is needed for the copper coated Kevlar for low frequency applications.

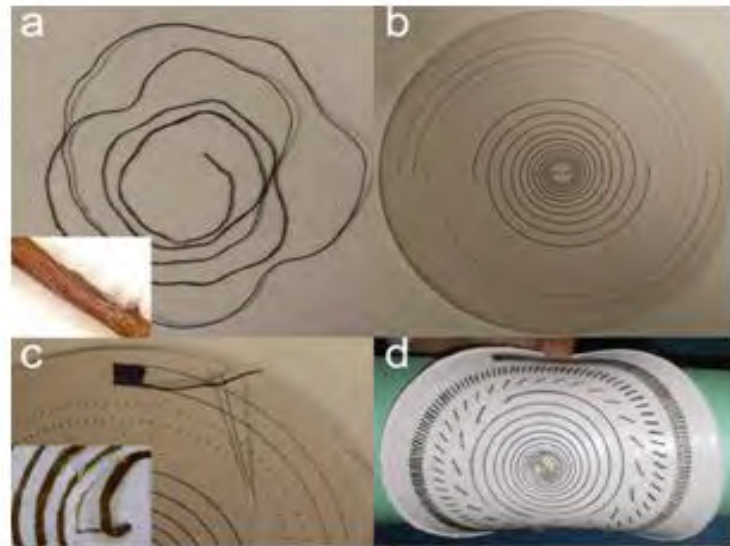


**Figure 2 Volumetric spiral antenna printed by U of Michigan (a) sample of encapsulated conductive yarn. (b) patterned PDMS substrate. (c) example of weaving and gluing (inset) (d) completed flexible, woven antenna.**

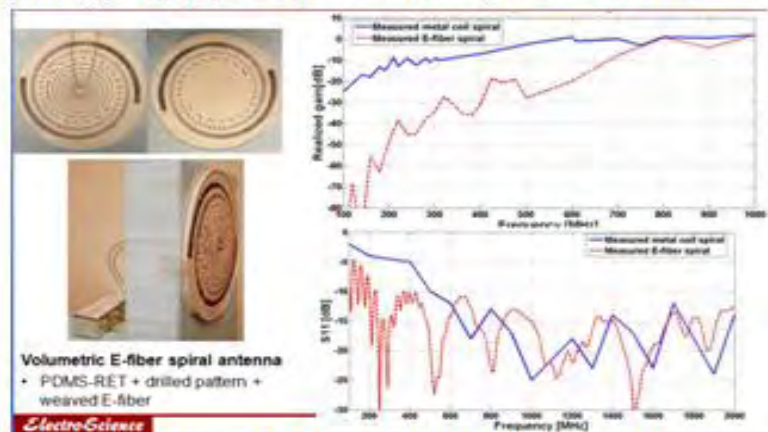


**Figure 3 RF performance of the stitched volumetric spiral antenna compared with that of metallic ceramic antenna**

In a parallel effort, we made remarkable progress in domain decomposition methods for fast and convergent computations associated with domains involving antenna details, particularly feeds or small wire and surface features. Last year, we demonstrated our novel fully overlapping domain

decomposition approach based on 2-dimensional (2D) geometries. Using radiation and scattering examples, we illustrated its superior accuracy and fast convergence. Particularly, our overlapping DDM was found suitable for problems involving multi-scale modeling of composite structures and embedded antennas. It achieves fast convergence by decoupling the ultra-dense mesh for small features from the homogeneous background mesh. In the last year of the program, we are happy to report the extension of the overlapping DDM to 3-dimensional (3D) problems. Technical details on this achievement are provided in the subsequent section.

## Embroidered E-fiber Technology

### *E-Fiber Embroidering on Polymer Composites*

To demonstrate the embroidering concept, we used Amberstrand<sup>®</sup> silver-coated Zylon fibers as the E-fiber conductor (see Figure 3). This e-fiber had a resistance of  $0.8 \Omega/\text{m}$  in addition to superior mechanical strength and flexibility due to the core Zylon fiber. As for the RF substrate, we employed polydimethylsiloxane (PDMS) mixed with rare-earth titanate ceramics (RET). The PDMS-RET composite was comprised of 90 vol% of PDMS and 10 vol% of RET. With this composite, we achieved a dielectric constant of  $\epsilon_r=4.15$  and a low loss tangent of  $\tan \delta < 0.01$ .

We developed a fabrication process to integrate the e-fibers onto the polymer substrate (see Figure 3). The substrate is also reinforced by non-conductive fabric layers to improve its load-bearing capability as shown in Figure 1. By employing the process in Figure 3, we fabricated a sample patch antenna and the details of the fabrication process will be presented at the conference. Although the E-fiber patch does not have a physically continuous conductive surface, it can be regarded as an electrically continuous surface since it was tightly knitted. The resolution of the e-fiber mesh was much less than  $1/20$  of the wavelength of operation.

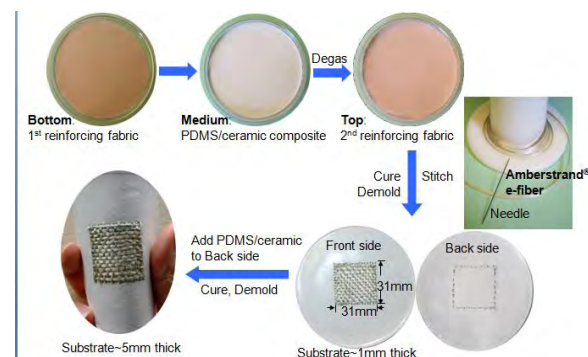


Figure 3 E-fiber Polymer Substrate Fabrication process

As displayed in Figure 1, an additional e-fiber surface can also be used to form the ground plane. Further, non-conductive fibers such as Kevlar, Zylon can be employed in the middle layer to strengthen the substrate and allow for load bearing capability.

### *E-fiber Automated Embroidery Process*

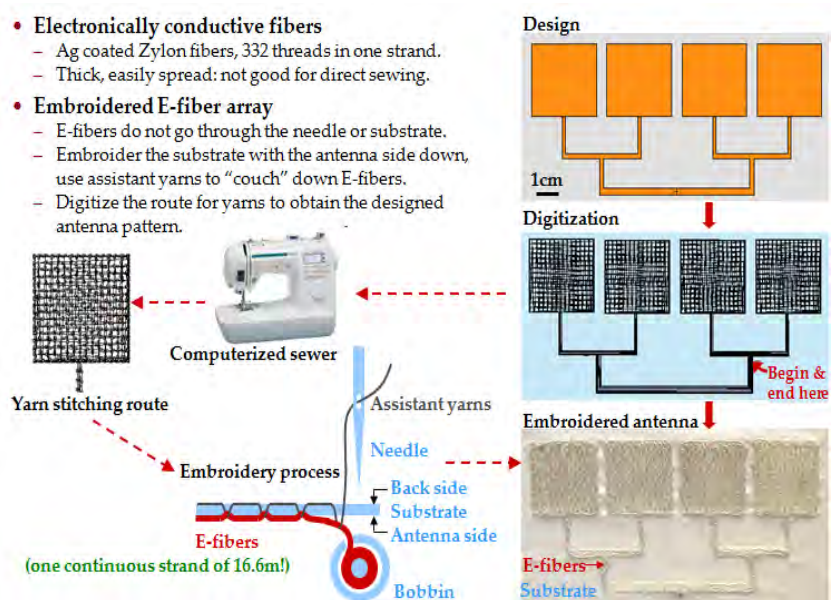


Figure 2 E-fiber Embroidery Process

We closely worked with embroidery experts to identify the best feasible stitching technique for the type of e-fiber we have. It's important to note that the stitching yarn used for sewing and embroidering are specially made by twisting the fiber into more robust form to be able to accommodate large number of frictions during the process. Given that our e-fiber is a silver coated fiber, any friction during the stitching process will degrade RF performance by reducing the fiber's conductivity. We therefore, identified the *bobbin* stitching technique as the ideal approach for embroidering e-fiber on the polymer substrate.

The above embroidery process is very scalable and computer automated as shown in Figure 2. The process starts with exporting the antenna design from widely used RF software tools such as HFSS, FEKO etc. to graphics form. This is next fed into a digitization software used for embroidering. This software identifies the stitches needed to make this pattern as accurate as possible. The digitations file is next imported to a computerized embroidery or sewing machine for final printing. This resulted in a pattern printed on a thin layer of polymer of textile for further integration into polymer with the process shown in Figure 3.

### ***E-fiber RF Patterns Fabrication Process***

As shown in Figure 6, the embroidered RF patterns are integrated on polymer substrate during the fabrication process. It starts with the mixing of PDMS composite in room temperature , followed by partially curing process of the polymer mixture under elevated temperature. The mixture is next tapecasted to form the substrate with smooth surface. Meanwhile, the backside of the embroidered E-fiber textile pattern was cleaned up for the next printing process. As depicted in Fig. 6, the E-fiber pattern was carefully flattened on top of the partially cured substrate, followed by a fully curing. We fabricated a 50 $\Omega$  polymer-based embroidered microstrip line. Final configuration of this microstrip was highly flexible with strong adhesion between the E-fiber textile and the PDMS. The entire fabrication process is low cost and straight-forward, making it a versatile printing method for various planar circuit and antenna specification.

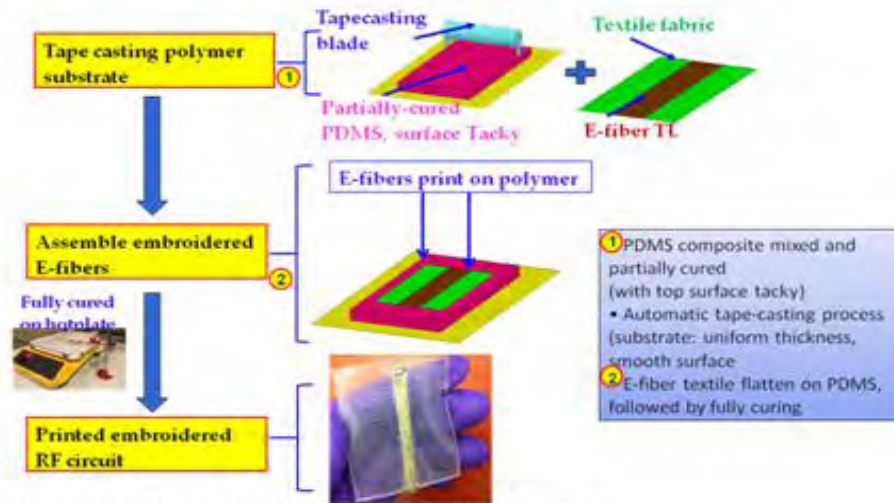


**Figure 6 E-fiber RF patterns Fabrication Process**

### ***E-fiber RF Performance Evaluation***

We next looked into evaluating performance of embroidered transmission line and antennas on polymer substrates.

#### ***A. E-Fiber Transmission Line Performance***

The RF performance of the embroidered E-fibers was evaluated using the  $50\Omega$  transmission line (TL) structure. As shown in Fig. 7, three samples were fabricated on PDMS substrates. They are composed of (A) E-fiber TL and copper ground plane (GP), (B) E-fiber TL and E-fiber ground plane, and (C) Copper TL and copper ground plane. Their S-parameters were measured using an Agilent N5230A network analyzer. As shown in Fig. 8, while sample (A) and (C) had the same copper ground plane, the insertion loss ( $S_{21}$ ) of the sample (A) composed of E-fiber TL was  $< 0.18\text{dB/cm}$  up to 4 GHz, only  $0.04\text{dB/cm}$  higher than that of the sample (C) of copper TL. In addition, sample (A) exhibited good impedance match up to 6GHz. This result demonstrated the high conductivity of the embroidered E-fibers and low loss property of the flexible PDMS substrate at RF frequencies.

Meanwhile, sample (B) showed a low insertion loss  $< 0.21\text{dB/cm}$  up to 4GHz, about  $0.07\text{dB/cm}$  higher than that of the sample (C). It also exhibited a good impedance match up to 5GHz. However, compared with sample (A), sample (B) had a higher  $|S_{21}|$  which indicates a slightly increased loss. This is possibly attributed to the power dispersion due to the physical discontinuity of the embroidered E-fiber ground plane.

#### ***B. Planar E-Fiber Patch Antenna Performance***

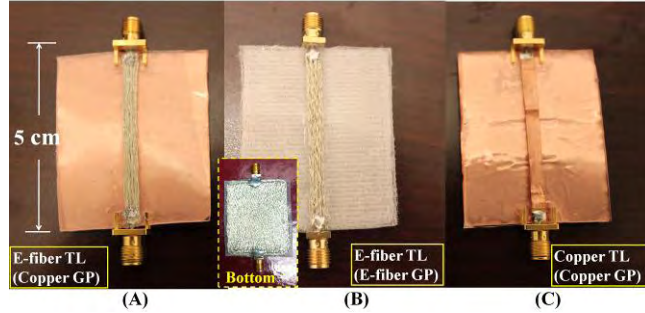


**Figure 7** Three transmission line samples (A) E-fiber TL and E-fiber ground plane, (B) E-fiber TL and copper ground plane, and (C) Copper TL and copper ground plane.

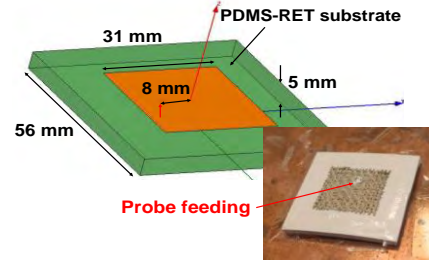


**Figure 9** Simulation model and fabricated E-fiber patch antenna

Referring to Figure 9, we fabricated a  $31\text{mm} \times 31\text{mm}$  e-fiber patch on a  $56\text{mm} \times 56\text{mm}$  PDMS substrate. The polymer substrate had a dielectric constant of  $\epsilon_r=3.8$  and loss tangent of  $\tan\delta=0.015$  at 2.2 GHz (resonance frequency). As shown in Figure 10, the measured gain was 5.7 dB, viz. only 0.2 dB lower than the simulated value corresponding to a perfect electric conductor (PEC) patch. This clearly demonstrates the remarkable performance of the e-fiber conductors.

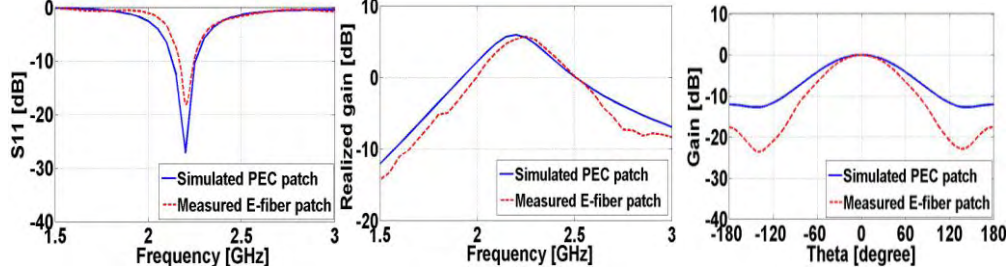


**Figure 10** (a) Return loss ( $S_{11}$ ) (b) Realized gain (c) Radiation pattern

### C. E-Fiber Patch on a Cylindrical Surface

To demonstrate performance the e-fiber patch's on a conformal surface, the patch was mounted on a cylinder surface (see Figure 11). Referring to the Figure for the measured return loss ( $S_{11}$ ), the gain and the radiation pattern of the bent E-fiber patch, we observe excellent agreement between the measurements and simulations. As expected, the curved patch has lower gain and this is predicted by the measurements and simulations. Measurements and simulations have a mere 1dB discrepancy in the gain as this is related to complexity of this setup for the simulations.

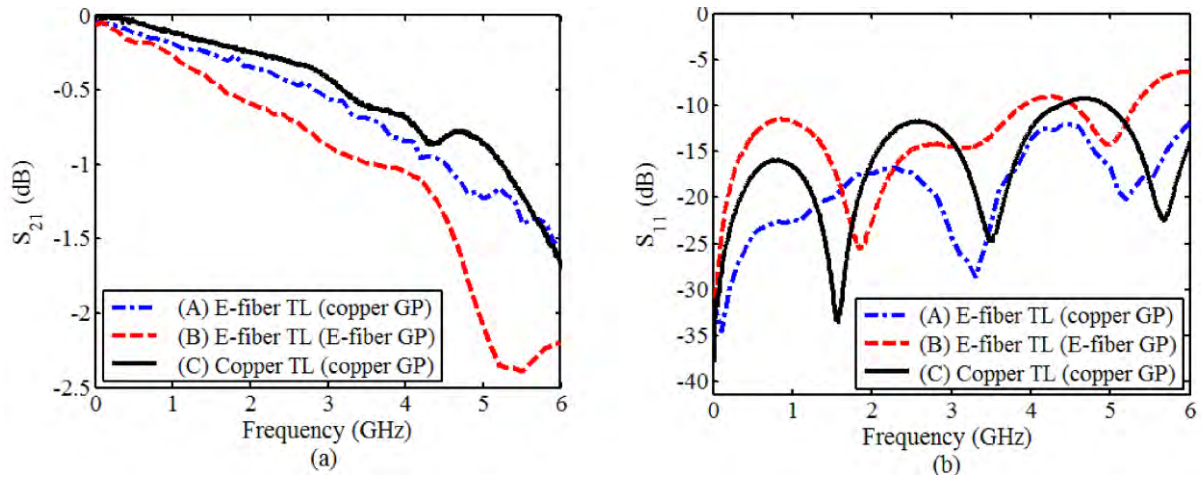


**Figure 8** Measured S-parameters of three transmission line samples: (a) measured  $S_{21}$  (b) measured  $S_{11}$ .

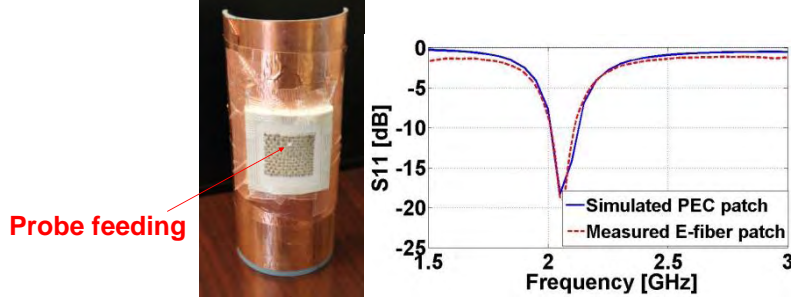


Figure 11 Fabricated e-fiber patch antenna mounted on cylinder and the return loss

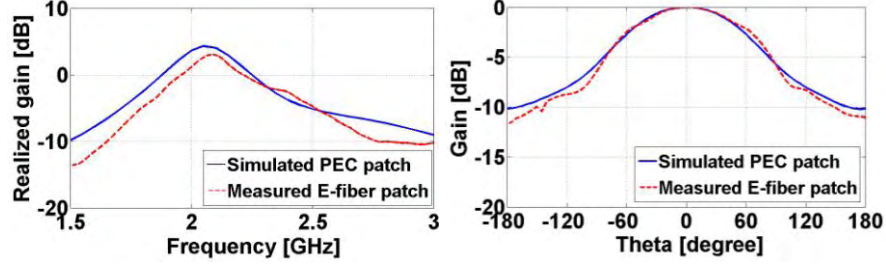


Figure 12 Measurement RF Performance of a Cylinder Mounted e-fiber patch antenna

#### D. Embroidered E-Fiber Patch Array

A  $4 \times 1$  E-fiber array antenna was fabricated, measured, and compared with the measured copper antenna and simulated PEC antenna of the same design (see Fig.13). As shown in Fig.14, the E-fiber antenna had a resonance frequency of 2.31GHz and the realized gain of 7.0 dB. This resonance frequency matched very well with that of the copper and PEC antennas, and the realized gain was only 1dB lower. On the other hand, the discrepancy in the resonance frequency between the three arrays was possibly introduced by the discontinuous conductive textile structure that leads to a slightly frequency shift.

Next, the performance of the conformal E-fiber array antenna on the curvilinear surface were measured similar to that of the conformal E-fiber patch antenna. For comparison, a Cu array antenna was fabricated by prefixing it on the conformal substrate (see Fig.15). The measurement results of E-fiber patch array were in good agreement with both copper array and simulation, as shown in Fig. 16. The realized gain of E-fiber array was 4.6dB, 1dB lower than that of the Cu array. In addition, the increased spacing among the patch elements during bending led to the difference between the radiation patterns of the conformal and flat array antennas.

The remarkable results of the E-fiber transmission line, patch antenna, and array antennas confirmed the feasibility of the proposed embroidered E-fiber technology for emerging conformal and flexible RF electronics. Moreover, the entire fabrication process was time and cost efficient, and has a great scale-up potential for industrial fabrications and applications.

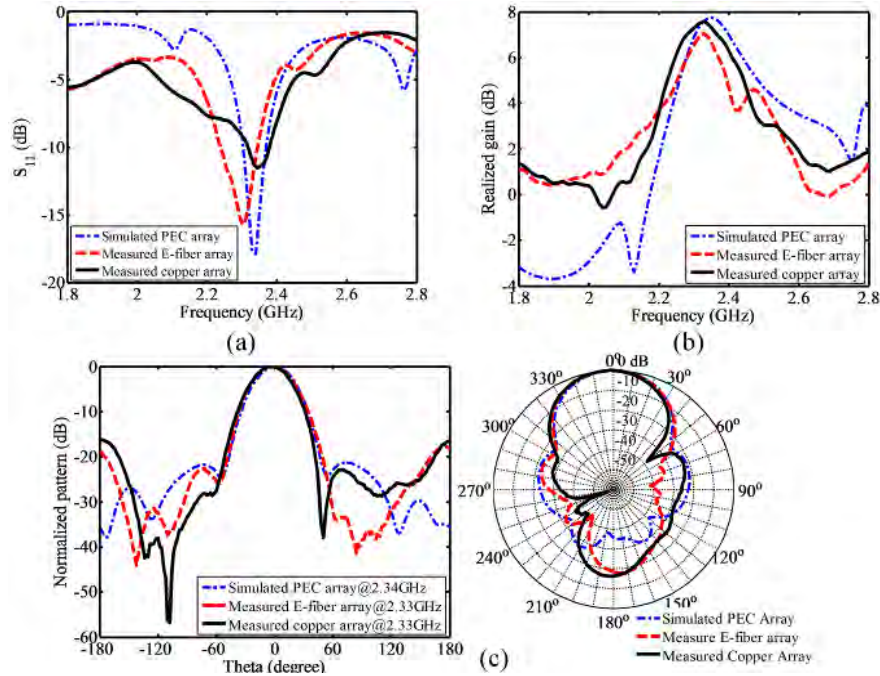


**Figure 14 Measured RF performance of the planar E-fiber antenna array: (a)  $S_{11}$ ; (b) realized gain; (c) H-plane radiation pattern**

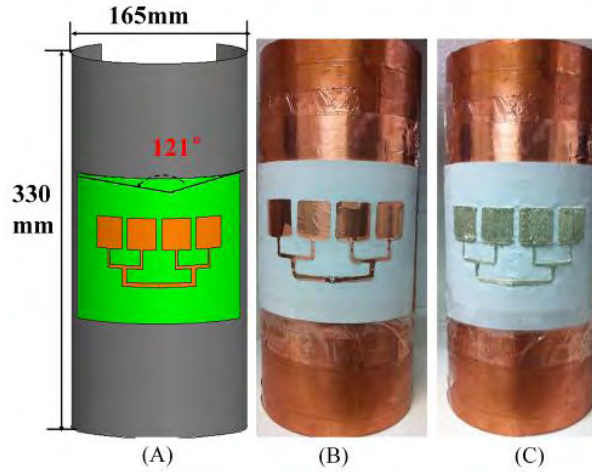


**Figure 4 E-fiber array antenna samples mounted on curvilinear surface (A) HFSS simulation, (B) E-fiber array, and (C) Copper array**

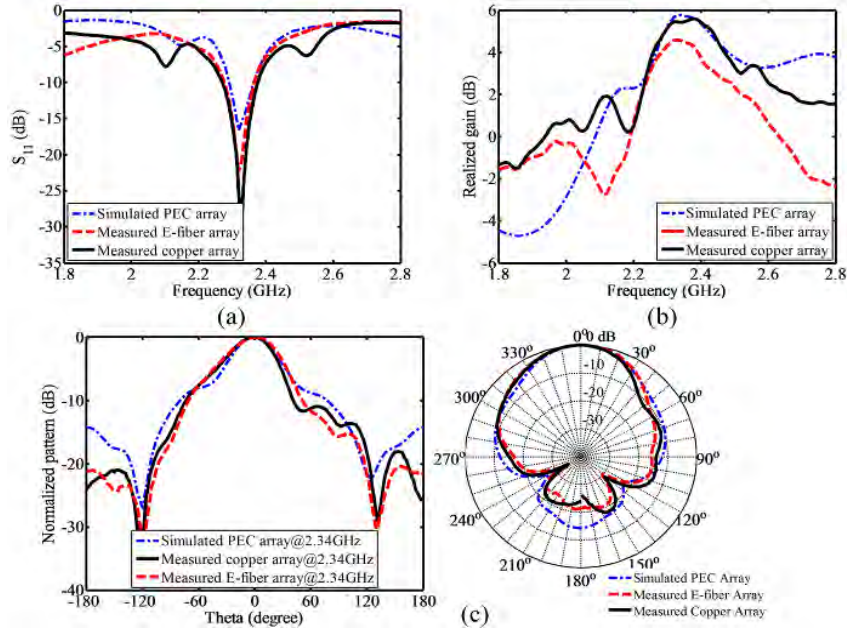


**Figure 5 Measured RF performance of the E-fiber antenna array mounted on curvilinear surface: (a)  $S_{11}$ ; (b) realized gain; (c) H-plane radiation pattern**

## Fully Overlapping Domain Decomposition (DDM) for Modeling Intricate Details within Large Media

In previous years, we proposed a new fully overlapping domain decomposition algorithm for the finite element modeling of intricate details embedded within large non-metallic media. This final year, we further demonstrated the validity and efficiency of this novel approach using  $h$ -refinement convergence. Also, higher order basis functions and higher order transmission conditions were shown to greatly improve the accuracy and flexibility of our method.

The  $h$ -refinement and DDM iterative convergence of the proposed fully overlapping domain decomposition method are compared with those of the conventional non-overlapping scheme, using a canonical PEC spherical scattering problem. In Figure 17, the scattering sphere, with radius  $R$ , is small compared to wavelength ( $R = \lambda/8$ ). It is shown in Figure 17(a) that fully overlapping DDM approach converges with respect to refined mesh density in almost exactly the same rate as non-overlapping scheme and direct finite element method. However, much faster iterative convergence and much less iterative time can be achieved using the fully overlapping DDM method as shown in Figure 17(b).

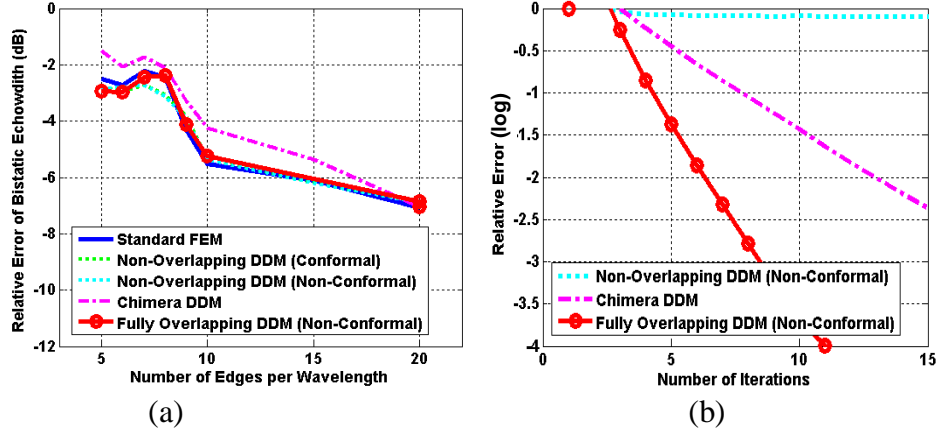


Figure 17: (a) h-refinement convergence; (b) iterative convergence; for a PEC spherical scattering problem ( $R = \lambda/8$ ).

Up till now, we have presented the properties of the fully overlapping domain decomposition approach using first order Nedelec edge elements and first order Robin transmission conditions. Similar to direct finite element method or non-overlapping DDM, higher precision can be achieved by using higher order edge elements and transmission conditions. Furthermore, the detail domain boundary can be placed very close ( $r_1 \ll \lambda/4$ ) or even touching the antennas when using higher order transmission conditions. For instance, in antenna *in-situ* design and optimizations, we frequently need to place the antenna on large non-metallic platforms. In these scenarios, the detail domain boundary would be touching the antenna itself. Next, we demonstrate the accuracy and iterative convergence of an antenna in free space, but with touching detail domain boundary as illustrated in Figure 18-19. Then, an antenna on platform problem is simulated using fully overlapping DDM and compared to the HFSS simulations in Figure 20.

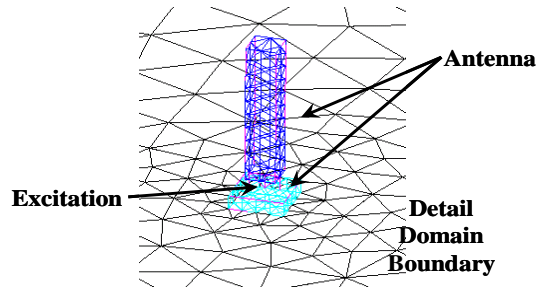


Figure 18: The meshing of a dipole antenna with touching detail domain boundary.

In Figure 19(a), iterative convergence is plotted as well as the input impedance comparison with HFSS simulations at a low frequency. The magnitude of the electrical fields is plotted in Figure 19(b). We note that there are some evanescent discontinuities residing on the touching detail domain boundary, probably due to the completely non-conformal meshing in the detail and background domains.

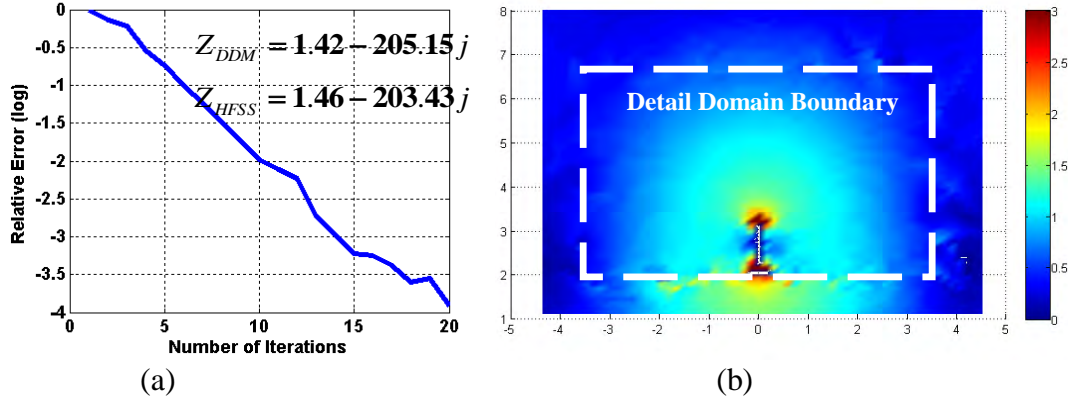


Figure 19: (a) iterative convergence and impedance comparison; (b) magnitude of the electrical fields; of the dipole in free space, but with touching detail domain boundary.

In Figure 20, an antenna placed on a PEC platform is simulated using fully overlapping DDM approaches at a low frequency (30 MHz). The antenna input impedance and directivities in  $\hat{x}-\hat{z}$  and  $\hat{y}-\hat{z}$  planes are compared to HFSS simulations. Better accuracy can be expected by increasing meshing density and radiation truncation boundary.

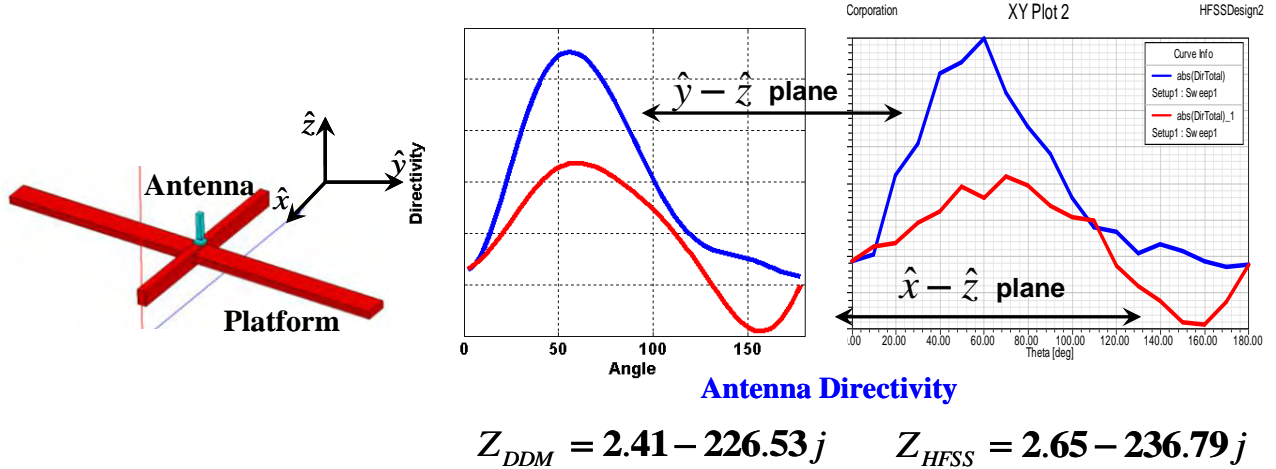


Figure 20: The directivity and input impedance comparison between fully overlapping DDM and HFSS simulations in simulating a dipole on a PEC platform at 30 MHz.

In conclusion, fully overlapping DDM possesses the property of faster convergence, good accuracy and supreme modeling flexibility. It is naturally suitable for parallel computing and antenna *in situ* design optimizations. The accuracy of the approach is illustrated by the *h*-refinement convergence, which shows the error of our fully overlapping DDM can be controlled in almost exactly the same rate as conventional FEM. Moreover, significant faster iterative convergence distinguishes our approach from traditional non-overlapping DDM. Finally, as a demo example, an antenna on a platform structure is simulated using fully overlapping DDM and compared to the standard HFSS results.

## **Prof. Rojas' Group Summary**

### **Students:**

1. Jun Seok Lee Ph.D, 3rd year, has been working in our group since April 2008, passed PhD candidacy exam
2. Idahosa A. Osaretin Ph.D, 4th year student, has been working in our group since June 2008, passed PhD candidacy exam

### **Journal Papers (submitted/to be submitted)**

1. J. S. Lee and R. G. Rojas, "Improved On-wafer Material Characterization Method for Magnetic/Dielectric Thin Films," To be submitted to the IEEE Transactions on Instrumentation and Measurement, 2010
2. J. S. Lee and R. G. Rojas, "Electromagnetic Characterization Method for On-Wafer Anisotropic Thin-Film Materials," To be submitted to the IEEE Transactions on Instrumentation and Measurement, 2010
3. I. A. Osaretin and R.G. Rojas, "Theoretical Model for the Magnetoelectric Effect in Magnetostrictive/Piezoelectric Composites," Submitted to Physical Review B
4. I. A. Osaretin and R. G. Rojas, "Realization of a Theoretical Model for the Transverse Magnetoelectric Effect in Magnetostrictive/Piezoelectric Composites using Field Boundary Conditions," Submitted to Physical Review B.
5. I. A. Osaretin and R. G. Rojas, "Effects of the Orientation of Biasing Fields on Magnetoelectric Coupling in Magnetostrictive/Piezoelectric composites," In preparation for submission to the Journal of Applied Physics.

### **Refereed Conference Papers**

1. J. S. Lee and R. G. Rojas, "Electromagnetic Characterization Method for On-Wafer Magnetic Dielectric Thin Film Materials," EuCAP 2010, Spain, April, 2010
2. J. S. Lee and R. G. Rojas, "Electromagnetic Material Characterization of On-Wafer Anisotropic Thin-Film Materials," accepted at AP-S/URSI 2010, to be presented in Canada, July, 2010
3. A. Osaretin and R. G. Rojas, "Magnetic Semiconductors for Millimeter-wave Nonreciprocal Device Applications," International Union of Radio Science (URSI) National meeting, Boulder CO, January, 2010
4. Osaretin and R. G. Rojas, "Planar Bianisotropic Waveguides for Application in Microwave Devices," European Conference on Antennas and Propagation (EuCAP), Barcelona, Spain, April 2010
5. Osaretin and R. G. Rojas, "Implementation and Modeling of Bianisotropic Media with Magnetoelectric Laminated Composites and Application to Non-reciprocal Devices," Accepted for the IEEE International Symposium on Antennas and Propagation and CNC/USNC/URSI Radio Science Meeting, Toronto, Canada, July 2010

## Research Summary

---

### Modeling of Electromagnetic Properties of Magnetoelectric Thin Films:

We present some breakthroughs in the numerical and theoretical modeling of magnetoelectric media. Our initial investigation was the implementation of planar waveguide structures using magnetoelectric media. This investigation was necessary to understand electromagnetic wave propagation in magnetoelectric media, and then to help propose microwave devices based upon the propagation phenomenon. Electromagnetic wave propagation within magnetoelectric, or bianisotropic materials in general, have been investigated since the late 1960s, and though there seems to be a host of potential microwave and millimeter wave applications, there has been little progress in terms of applications because of the lack of progress in the actual implementation of this material. Bianisotropic media represents materials where the electric and magnetic fields are coupled in its constitutive relations, as shown in (1) below.

$$\begin{aligned}\mathbf{D} &= \bar{\bar{\epsilon}}\mathbf{E} + \bar{\bar{\xi}}\mathbf{H} \\ \mathbf{B} &= \bar{\bar{\mu}}\mathbf{H} + \bar{\bar{\zeta}}\mathbf{E}\end{aligned}\quad (1)$$

The permittivity, permeability and magnetoelectric parameters are usually 3x3 matrices. This fact makes it rather difficult to obtain analytic solutions for electromagnetic waves travelling in planar structures. Implementation of magnetoelectric material by many groups, including Prof. Carmen at UCLA, has introduced renewed interest in the material.

In previous reviews, we had presented a numerical modeling tool to obtain solutions to electromagnetic wave propagation in complex materials. Using this tool, implemented using COMSOL multiphysics software, we are able to observe the propagation characteristics for a magnetoelectric thin film in a planar waveguide structure. In this research study, the material characteristics of the substrate are very important. We assumed the magnetoelectric material will have magnetic characteristics as is the case with either the piezomagnetic or magnetostrictive materials used in the realization of the magnetoelectric effect. The permittivity and permeability of the media used in this study is given as (DC magnetic bias along z-axis):

$$\bar{\bar{\epsilon}} = \epsilon_0 \begin{bmatrix} 5-j & 1+6j & 0 \\ -(1+6j) & 5-j & 0 \\ 0 & 0 & -(10-5j) \end{bmatrix}, \quad \bar{\bar{\mu}} = \mu_0 \begin{bmatrix} 0.9-j0.05 & -(0.08+j0.005) & 0 \\ 0.08+j0.005 & 0.9-j0.05 & 0 \\ 0 & 0 & 1-j0.05 \end{bmatrix} \quad (2)$$

Simulation of the planar bianisotropic waveguide is done using lossless bianisotropic tensors ( $\bar{\bar{\xi}}, \bar{\bar{\zeta}}$ ). This implies that the tensors are Hermitian in form, and the magnetoelectric tensors have the relationship  $\bar{\bar{\xi}} = \bar{\bar{\alpha}}$  and  $\bar{\bar{\zeta}} = \bar{\bar{\alpha}}^+$ . The theoretical values for the magnetoelectric tensor (ME), which represent the magnetic point group 2, m', or 2/m', used in this study are given as:

$$\bar{\bar{\alpha}} = \frac{1}{c_0} \begin{bmatrix} 3 & j0.15 & 0 \\ -j0.15 & 3 & 0 \\ 0 & 0 & 2.7 \end{bmatrix} \quad (3)$$

The above ME matrix has values that are probably too high and difficult to achieve with bulk or layered materials. However, it is shown here to investigate electromagnetic effects that could be achieved with these materials. We investigated a microstrip line as shown in Fig. 1a. This planar structure consists of two layers where the bottom layer is the magnetoelectric medium and the second layer is a low loss dielectric (insulator). The dielectric layer is used to allow a better

portion of the wave to propagate in the dielectric layer than in the bianisotropic layer where attenuation of the wave may be greater. However, this set up also allows for the propagation phenomena existing in the bianisotropic media to show up in the entire structure.

Simulation of the microstrip line was done at 25GHz. The dimensions of the line are given as  $B=0.067\lambda$ ,  $D=0.058\lambda$ , and  $W=0.167\lambda$ . Figure 1b shows the time average power flow in the z-direction (propagating out of page). Numerical analysis of the structure shows a field displacement phenomenon. This phenomenon, although with a DC magnetic field bias along direction of propagation, is similar to that which occurs in ferrites and magnetized semi-conductors, when the magnetic bias is transverse to the propagation direction and the plane of the thin films. Such field displacement effect is used in several nonreciprocal microwave and millimeter wave devices.

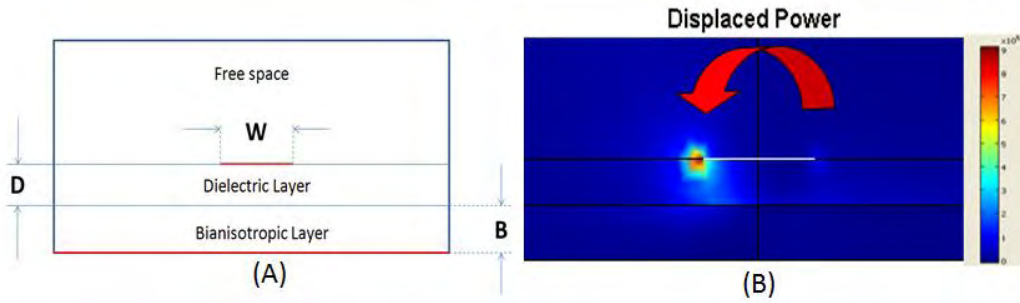


Fig. 1: Schematic diagram of the microstrip line is shown in (A). The red lines in the figure represent perfect electric conductors (PEC). (B) Simulated result for the magnetoelectric microstrip line. Observe propagation along left edge of microstrip.

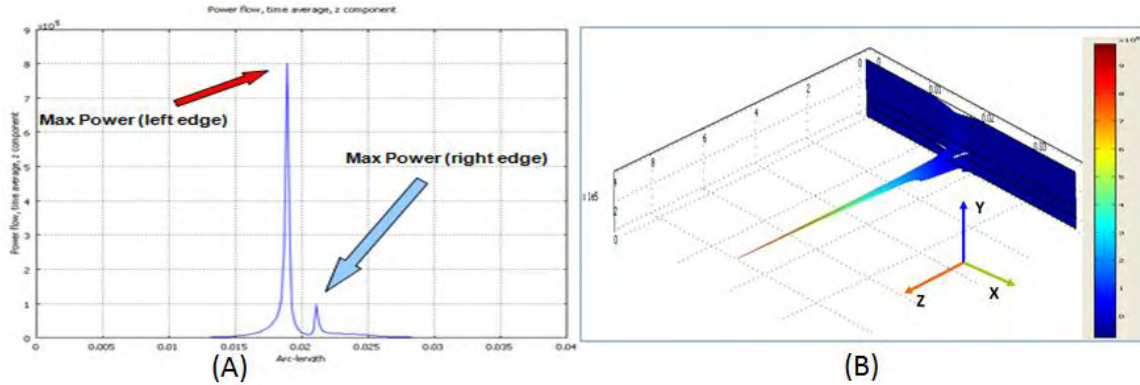


Fig. 2: (A) Time average power flow across the face of the planar structure. Maximum power density along each edge of the microstrip line. (B) 2D surface plot of the propagation fields along one edge of the microstrip.

It can be observed that there is increased power propagation along one edge of the microstrip line, with much less power propagating on the other end. This magnetoelectric microstrip line configuration can be easily applied to the design of 2-port isolator or a 3-port circulator. The displaced power observed in the structures stems from the displaced fields within the structure, resulting from the material properties of the media. The magnetoelectric thin film with a DC magnetic field bias serves as a nonreciprocal media causing the displacement of the electric and magnetic field components towards the right part of the structure. A subdomain power integration of each half (left and right) of the magnetoelectric microstrip structure shows that

99% of the power is displaced towards the left edge of the line. This confirms that a nonreciprocal field displacement effect is possible with thin magnetoelectric films biased along the direction of propagation.

An important part of the investigation into practical electromagnetic applications of the ME media is the theoretical model of the media used in numerical simulations. Harshe, [G. Harshe, J.P Dougherty and R.E. Newnham, “Theoretical Modeling of Multilayer Magnetoelectric Composites, *Int. Journal of Appl. Electromag. in Mater.* **4**, 1993] obtained theoretical models for the longitudinal ME voltage coefficient of multilayer composites composed of lead zirconate titanate (PZT) and ferrite layers (Cobalt and Nickel Ferrite). However, there were large deviations between the ME voltage coefficient obtained via theoretical modeling, and corresponding experimental values of fabricated structures. The experimental results were comparable to those reported in literature, but the theoretical results were several times higher. Reasons for the poor agreement between theoretical and experimental results include poor interface coupling between the layers and the application of boundary conditions used to obtain the model. Since then, other works have looked into obtaining theoretical models that account for the mismatch at the composite’s bonding interface. This was done using an interface coupling parameter that models the strain transfer relationship between the piezoelectric and magnetostrictive phases. The ME voltage coefficients obtained in these works had similar trends as the experimental data, however, there still remained large deviation in the overall magnitude of the ME voltage coefficients, as theoretical results remained several times higher than experimental values.

In contrast to previous work, we apply fundamental electromagnetic wave boundary conditions on the fields within the composite structure. We introduce new theoretical models for the ME effect in a piezoelectric/magnetostrictive bilayer that better approximates the experimental results. The model is obtained by solving the constitutive equations of each layer for the all fields present, and then applying a field averaging method, along with boundary conditions on the components of the fields at the composite interface, to obtain a homogenized layer. The layer is characterized in terms of its effective permeability, effective permittivity and the effective ME susceptibility tensor with constitutive equations of the form shown in (1).

We have successfully modeled the ME media for each of the three basic configurations as can be observed in Fig. 3. We have improved the agreement with measured data obtained in the work done by Harshe. We summarize here the constitutive relationship for each of these cases. First, for the longitudinal case, we have the media poled and biased in the 3 direction. The homogenized constitutive relationship is obtained as

$$\begin{bmatrix} D_x \\ D_y \\ D_z \end{bmatrix} = \begin{bmatrix} 0 & 0 & 0 \\ 0 & 0 & 0 \\ 0 & 0 & \alpha_{zz}^H \end{bmatrix} \begin{bmatrix} H_x \\ H_y \\ H_z \end{bmatrix} + \begin{bmatrix} \epsilon_{xx} & 0 & 0 \\ 0 & \epsilon_{yy} & 0 \\ 0 & 0 & \epsilon_{zz} \end{bmatrix} \begin{bmatrix} E_x \\ E_y \\ E_z \end{bmatrix} \quad \begin{bmatrix} B_x \\ B_y \\ B_z \end{bmatrix} = \begin{bmatrix} 0 & 0 & 0 \\ 0 & 0 & 0 \\ 0 & 0 & \alpha_{zz}^E \end{bmatrix} \begin{bmatrix} E_x \\ E_y \\ E_z \end{bmatrix} + \begin{bmatrix} \mu_{xx} & \mu_{xy} & 0 \\ \mu_{yx} & \mu_{yy} & 0 \\ 0 & 0 & \mu_{zz} \end{bmatrix} \begin{bmatrix} H_x \\ H_y \\ H_z \end{bmatrix} \quad (4)$$

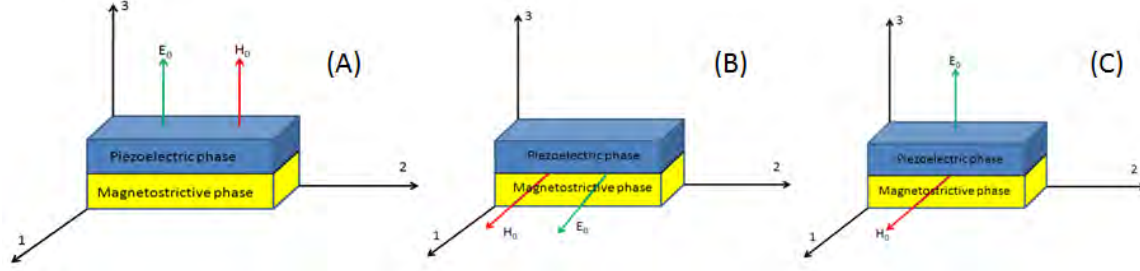


Fig. 3: Orientation of biasing fields for the magnetoelectric media in terms of the poling (electric) and biasing (magnetic) fields. (A) Longitudinal; (B) In-plane longitudinal; (C) Transverse. Each orientation produces a different form of the constitutive relationship.

Using the magnetoelectric susceptibility tensor, we can compute the magnetoelectric voltage coefficient. Plots of the calculated ME voltage coefficient is shown in Fig. 4. We also consider the effects of strain/stress coupling between the piezoelectric and magnetostrictive material. We make use of an interface coupling parameter,  $k$ , to model the strain transfer between phases. An interface coupling factor of one ( $k=1$ ) implies perfect coupling and thus complete strain transfer between phases. It is important to note that one cannot expect a perfect coupling at the interface since the phases are not joined at a microscopic level. In most cases, some form of adhesive is used to hold the phases together.

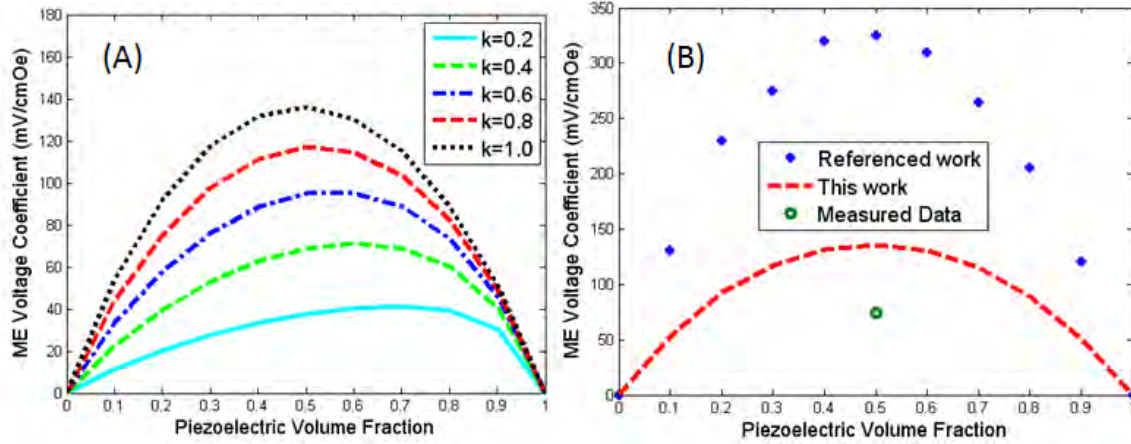


Fig. 4: Plots of the longitudinal ME voltage coefficients for PZT-CFO bilayer. (A) shows the effect of the interface coupling parameter between phases. (B) compares our theoretical model to measured results and previous theoretical model by Bichurin et al.

The theoretical model here obtained better characterizes the ME voltage coefficient of piezoelectric and magnetostrictive bilayers. This new theoretical model realized here significantly reduces the deviation between the magnitude of previous theoretical models and experimental data, while maintaining established trends of the ME voltage coefficient. The measured value of the ME media for an equal volume composition of the piezoelectric and magnetostrictive phases was 74 mV/cmOe obtained by Harshe. Our theoretical model gives a value of 140 mV/cmOe for perfect coupling between phases compared to 340 mV/cmOe from previous models. Additional studies on the coupling possible between phases can lead to the actual value of the coupling coefficient,  $k$ , for any two phases. From our theoretical model, we can approximate the interface coupling between phases as  $k=0.58$ . The theoretical model includes expressions for the effective permeability, permittivity, and ME susceptibility tensor of

the bilayer. These expressions obtained will allow for better investigation of the ME composite towards potential device applications. The theoretical model also accounts for the bond mismatch at the interface of the layers, which is important in the physical realization of an ME composite with a high ME voltage coefficient. Detailed information on the theoretical model is available in the journal papers submitted as part of this research effort.

Theoretical modeling for the transverse ME effect was also completed. In this orientation, the direction of the magnetic field bias is changed from the 3-direction to the 1-direction, as observed in Fig. 3. The media remains poled in the 3-direction. The constitutive relationship for the transverse ME effect is given as

$$\begin{bmatrix} D_x \\ D_y \\ D_z \end{bmatrix} = \begin{bmatrix} 0 & 0 & 0 \\ 0 & 0 & 0 \\ \alpha_{zx}^H & 0 & 0 \end{bmatrix} \begin{bmatrix} H_x \\ H_y \\ H_z \end{bmatrix} + \begin{bmatrix} \epsilon_{xx} & 0 & 0 \\ 0 & \epsilon_{yy} & 0 \\ 0 & 0 & \epsilon_{zz} \end{bmatrix} \begin{bmatrix} E_x \\ E_y \\ E_z \end{bmatrix} \quad \begin{bmatrix} B_x \\ B_y \\ B_z \end{bmatrix} = \begin{bmatrix} 0 & 0 & \alpha_{xz}^E \\ 0 & 0 & 0 \\ 0 & 0 & 0 \end{bmatrix} \begin{bmatrix} E_x \\ E_y \\ E_z \end{bmatrix} + \begin{bmatrix} \mu_{xx} & 0 & 0 \\ 0 & \mu_{yy} & \mu_{yz} \\ 0 & \mu_{zy} & \mu_{zz} \end{bmatrix} \begin{bmatrix} H_x \\ H_y \\ H_z \end{bmatrix} \quad (5)$$

Similar to the longitudinal case, plots the magnetoelectric voltage coefficient for a PZT-Nickel ferrite (NFO) bilayer can be seen in Fig. 5.

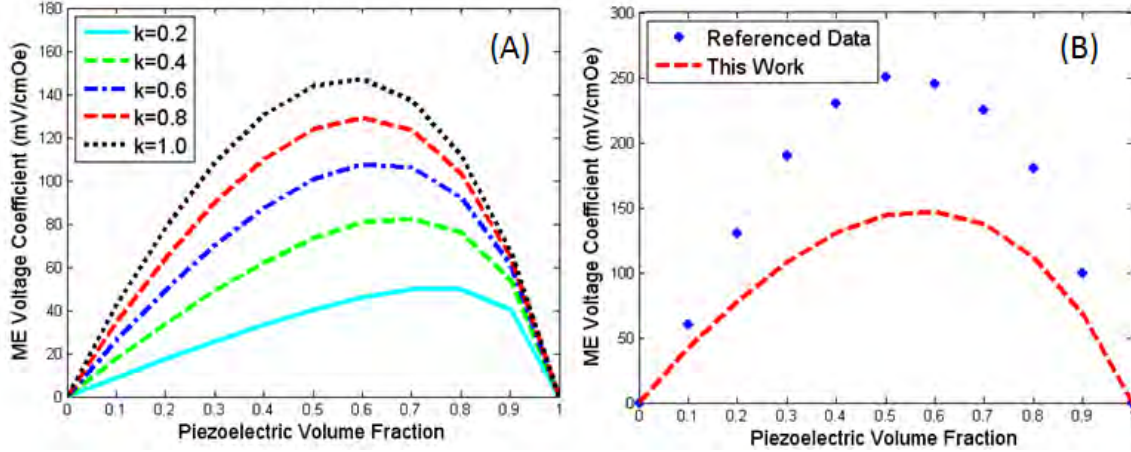


Fig. 5: Plots of the transverse ME voltage coefficients for a PZT-NFO bilayer. (A) shows the effect of the interface coupling parameter between phases. (B) compares our theoretical model to previous theoretical model by Bichurin et al. Note that our model shows a lower ME voltage coefficient as is consistent with measured values.

The results of the modeling are consistent with the behavior of the ME media from previous theoretical models. However, the magnitude of the ME voltage coefficient for our theoretical model is much lower than previous models. This is also consistent with comparisons of previous theoretical results to measured data available for the ME media. The theoretical model obtained for the transverse ME effect includes expressions for the effective permeability, permittivity, and ME susceptibility tensor of the bilayer. From the ME susceptibility tensor, the ME voltage coefficient is obtained. The transverse ME effect produces a higher ME susceptibility compared to that of the longitudinal case. This is based solely on the material property of the media and hence the greater resultant effect of the magnetic field bias in the 1-direction of the media.

Finally, we obtained a homogenized form for the constitutive relationship of the in-plane magnetoelectric media. In this orientation, the media is poled and biased in the 1-direction (see Fig. 3). As was done for each of the ME orientations, we obtained the homogenized effective permeability, permittivity, and ME susceptibility tensor of the media. Using this information we obtained the constitutive relationship of the media as shown below.

$$\begin{bmatrix} D_x \\ D_y \\ D_z \end{bmatrix} = \begin{bmatrix} \alpha_{11}^H & 0 & 0 \\ 0 & 0 & 0 \\ 0 & 0 & 0 \end{bmatrix} \begin{bmatrix} H_x \\ H_y \\ H_z \end{bmatrix} + \begin{bmatrix} \epsilon_{11} & 0 & 0 \\ 0 & \epsilon_{22} & 0 \\ 0 & 0 & \epsilon_{33} \end{bmatrix} \begin{bmatrix} E_x \\ E_y \\ E_z \end{bmatrix} \quad \begin{bmatrix} B_x \\ B_y \\ B_z \end{bmatrix} = \begin{bmatrix} \alpha_{11}^E & 0 & 0 \\ 0 & 0 & 0 \\ 0 & 0 & 0 \end{bmatrix} \begin{bmatrix} E_x \\ E_y \\ E_z \end{bmatrix} + \begin{bmatrix} \mu_{11} & 0 & 0 \\ 0 & \mu_{22} & \mu_{23} \\ 0 & \mu_{32} & \mu_{33} \end{bmatrix} \begin{bmatrix} H_x \\ H_y \\ H_z \end{bmatrix} \quad (6)$$

In summary, we have obtained a complete theoretical model for the magnetoelectric effect in piezoelectric and magnetostrictive bilayers. The model includes expressions for the homogenized effective permeability, permittivity, and ME susceptibility tensor of the bilayer. We also have been able to complete numerical modeling of a theoretical magnetoelectric media using planar waveguide structures. We have observed possible applications using the non-reciprocal

propagation phenomena of the structure. However, the magnetoelectric susceptibility

obtained from the theoretical modeling of the PZT-ferrite bilayers is of small magnitude such that similar effects in waveguide structures have not been duplicated. We are currently investigating the use of materials with higher piezoelectric and piezomagnetic coupling coefficients to influence an increase in the magnetoelectric susceptibility of the media.

### Magnetic Semiconductors for Non-reciprocal Device Applications:

Magnetic semiconductors have an anisotropic permeability and permittivity under a DC magnetic field bias. The shape of the permeability and permittivity tensors depend on the direction of the DC magnetic field bias. Assuming a Z-directed DC magnetic field bias, the permeability and permittivity of the magnetic semiconductor is given by

$$\bar{\bar{\mu}} = \mu_0 \begin{bmatrix} \mu & j\kappa & 0 \\ -j\kappa & \mu & 0 \\ 0 & 0 & 1 \end{bmatrix}, \quad \bar{\bar{\epsilon}} = \epsilon_0 \begin{bmatrix} \epsilon_1 & -j\epsilon_3 & 0 \\ j\epsilon_3 & \epsilon_1 & 0 \\ 0 & 0 & \epsilon_2 \end{bmatrix} \quad (7)$$

The value of the tensor components depends on the material characteristics of the media, as well the magnitude of the DC magnetic field bias. There are three basis configurations based upon the propagation and bias directions: Faraday, Perpendicular, and Voigt. Analytic solutions are obtained for all three cases in unbounded media. The results obtained from the analytical solutions show that magnetic semiconductors behave similar to materials with solely anisotropic permeability or permittivity. However, the propagation constants for the magnetic semiconductor contain more design variables that would surely be useful as more applications are discovered.

The magnetic semiconductor modeled here is a high mobility GaAs/AlGaAs heterostructure doped with Manganese. This magnetic semiconductor was chosen for its high mobility, which holds at sub-room temperature (77K). Currently, there are not any high mobility magnetic semiconductors with Curie temperature at room temperature. An obvious disadvantage in using magnetic semiconductors or semiconductors in general, in planar waveguide structures is the ohmic dissipation that is introduced into the structure. For this reason, we utilize an insulating low loss dielectric layer ( $\epsilon_r = 2.7$ ) to help alleviate this problem (see Fig 6). The dielectric layer is a propagation channel which holds a majority of the electromagnetic waves in the structure. Using the properties of the magnetic semiconductor and the magnitude of the external DC

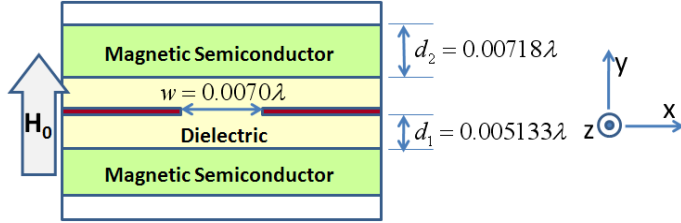


Figure 6: Model of magnetic semiconductor slotline. DC magnetic field bias is 0.3T in the Y-direction.

magnetic field bias as 0.3T in the Y-direction, we obtain the permittivity and permeability of the material as follows:

$$\bar{\bar{\epsilon}} = \epsilon_0 \begin{bmatrix} 30.5 - j19 & 0 & -7.9 - j93.7 \\ 0 & -236 - j202 & 0 \\ 7.9 + j93.7 & 0 & 30.5 - j19 \end{bmatrix}, \quad \bar{\bar{\mu}} = \mu_0 \begin{bmatrix} 0.957 & 0 & j0.15 \\ 0 & 1 & 0 \\ -j0.15 & 0 & 0.957 \end{bmatrix} \quad (8)$$

Simulation of the planar structure was carried out at 30GHz using COMSOL multiphysics solver. We observe a displacement of the power propagating along the slot, towards one edge (see Fig. 7(a)). The reason for the observed field displacements comes from the interaction between the Hall currents, produced by the application of the external DC magnetic fields to the magnetic semiconductor, and the electric fields propagating in the structure. To see if the magnetic semiconductor provides larger displacement than a non-magnetic semiconductor, we compare the power displaced in the structure to that of an often used GaAs semiconductor. This semiconductor has similar elemental base as the magnetic semiconductor heterostructure. The material characteristics of the semiconductor are given as: carrier concentration  $n = 2 \times 10^{20} \text{ cm}^{-3}$ ; the electron mobility  $\mu_e = 20 \text{ m/V} \cdot \text{s}$  at 77K; static dielectric constant  $\epsilon_{s0} = 13.1$ ; the effective mass  $m^* = 0.063$ . A comparison of the results comparing the nonreciprocal phenomenon in both substrates is shown in Fig. 7. We observe that there is significant improvement in the displaced power.

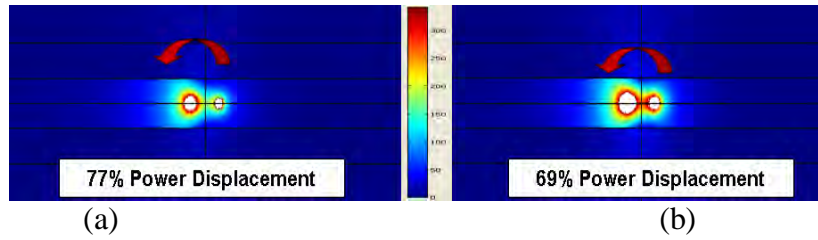


Figure 7: Comparison of the power displacement in a magnetic semiconductor slotline to a semiconductor slotline: (a) Magnetic Semiconductor, (b) Semiconductor

The phenomena shown here is readily applicable to non-reciprocal devices such as isolators and circulators. A 3D numerical model for a 3 port circulator currently under development is shown Fig. 8.

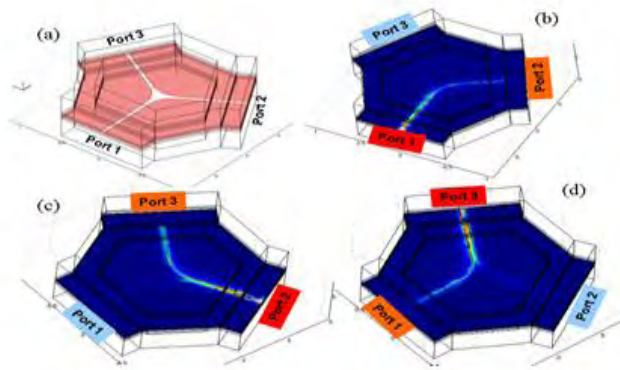


Figure 8: 3-port circulator design based upon magnetic semiconductor slotline. (a) 3D simulation model; (b) excitation at port 1; (c) excitation at port 2; (d) excitation at port 3

### Characterization of EM Properties of On-Wafer Magnetic/Dielectric thin-films

**Error analysis:** Our newly developed method for magnetic dielectric on-wafer thin-film characterization is discussed here. This method requires the generation of various test on the test wafer. However, the generated fixtures will always have some errors due to the imperfection of the fabrication process. In our method, microstrip or other planar transmission lines can be used; however, this discussion is limited to microstrip lines. Since the width of the microstrip line plays a very important role, it is imperative to present an error analysis in terms of this parameter. Keeping in mind that two different widths of the microstrip line are used in our method, we generated two sets of random numbers for the microstrip line widths. In this analysis, we used an electromagnetic simulation tool to study the errors in measuring the permittivity and permeability due to errors in the microstrip line width. In the simulation, we used two microstrip transmission lines which had line widths of  $500\ \mu\text{m}$  and  $600\ \mu\text{m}$ , respectively (see Fig. 9). Two sets of random numbers were generated. The first set had a mean of  $500\ \mu\text{m}$  and a standard deviation of  $\pm 2.5\ \mu\text{m}$ . Similarly, the second set had a mean of  $600\ \mu\text{m}$  and a standard deviation of  $\pm 3\ \mu\text{m}$ . Fig. 10 shows simulated results with a standard error analyses for both  $\epsilon'_r$  and  $\mu'_r$ . The red, blue, and green curves represent average values, upper 95% limit, and lower 95% limit, respectively. We used standard error given by  $SE = s/\sqrt{n}$  where  $s$  is the sample standard deviation and  $n$  is the sample size. Also, the upper and lower 95% limits are given by: 95% confidence limits  $= \bar{x} \pm (SE \times 1.96)$  where  $\bar{x}$  is the sample mean. The maximum and minimum variations of  $\epsilon'_r$  for the upper and lower 95% limits are 0.182 and 0.180, respectively. Also, the maximum and minimum variations of  $\mu'_r$  for the upper and lower 95% limits are 0.205 and 0.2012, respectively. The expected maximum and minimum errors of extraction value of  $\epsilon'_r$  with respect to the exact value of 3 in the upper and lower 95% confidence limits are 3.73% and 2.78%, respectively. The expected extraction error with respect to the exact  $\mu'_r$  value of 2 has 15.13% for the maximum error and 4.10% for the minimum error. The results of the error analysis for the extraction of  $\epsilon'_r$  and  $\mu'_r$  show that our newly developed magnetic dielectric characterization method can yield extracted values for both  $\epsilon'_r$  and  $\mu'_r$  with approximately 10% error even if the test structures have fabrication errors.

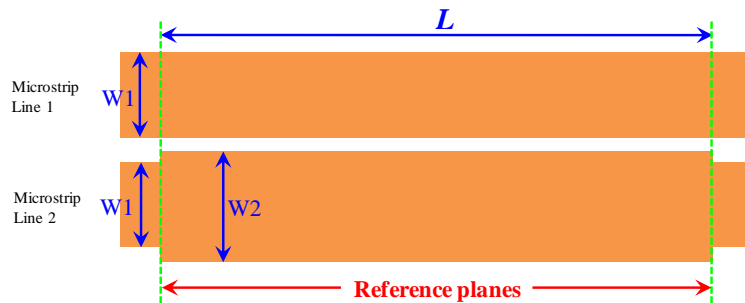


Fig. 9: Test set of microstrip lines with different line widths ( $W1 = 500\ \mu\text{m}$  and  $W2 = 600\ \mu\text{m}$ )

Another consideration is a standard error analysis of the material loss. Fig. 11 shows the simulated results with standard error analysis for both  $\epsilon''_r$  and  $\mu''_r$  (the exact values of  $\epsilon''_r$  and  $\mu''_r$  are 0.015 and 0.01, respectively). This analysis includes all possible variables in both DUTs and the TRL calibration kits. Although this analysis includes all the variables, the maximum and minimum variations for the upper and lower 95% confidence limits are very small. For  $\epsilon''_r$ , the maximum and minimum variations are 0.000426 and 0.000254, respectively. Also, the maximum and minimum variations for  $\mu''_r$  are 0.000847 and 0.000495, respectively. The variations in  $\mu''_r$  are larger than they were for the  $\epsilon''_r$  analysis case; however, the sizes of the variations were still small.

**Anisotropic thin-film characterization:** The accurate characterization of the electromagnetic properties ( $\epsilon$  and  $\mu$ ) of new, on-wafer thin films is crucial for accessing their potential use in the design of microwave devices, antennas, and a variety of sensors. Furthermore, many of the new materials being developed are anisotropic, and conventional techniques for isotropic material characterization methods cannot be used. The method developed in our research is based on the mapping of an anisotropic region in the Z-plane into an isotropic region in the W-plane.

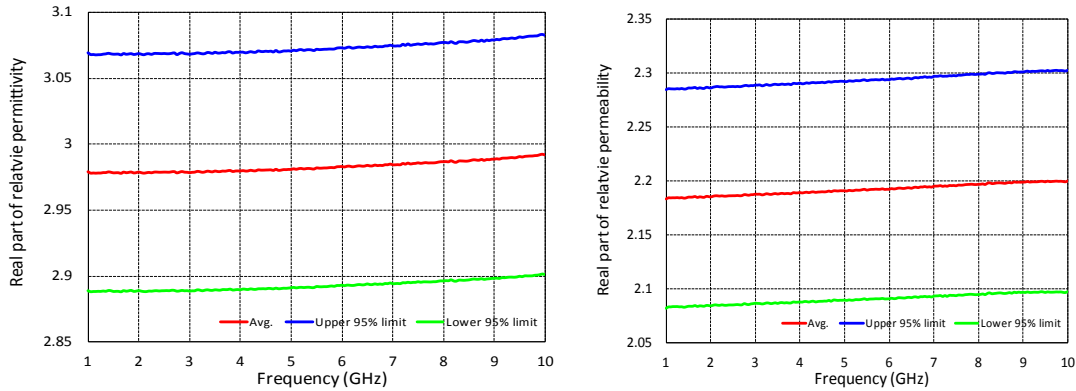


Fig. 10: Simulated results for the real parts of permittivity (left) and permeability (right) with standard error analysis ( $\epsilon'_r = 3$  and  $\mu'_r = 2$  are the exact values). Errors introduced in both DUT's and TRL calibration kits

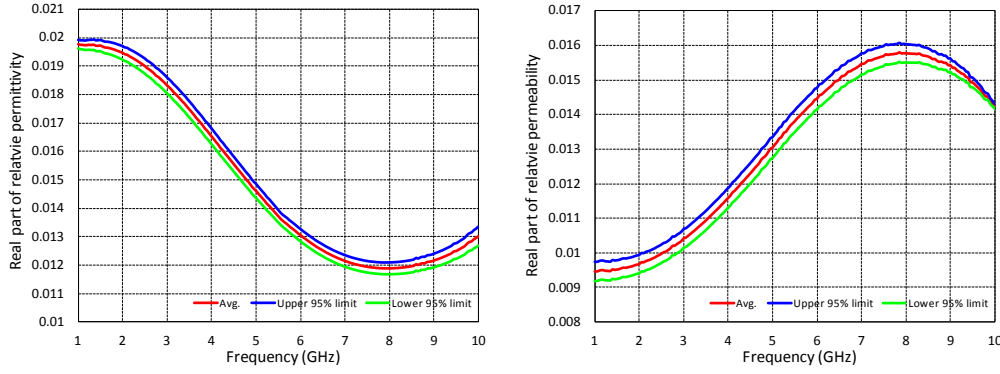


Fig. 11. Simulated results for the imaginary parts of permittivity (left) and permeability (right) with standard error analysis. Red curves on both plots are the average values of  $\epsilon''_r$  and  $\mu''_r$ . Blue and Green curves represent the upper and lower 95% limits, respectively. ( $\epsilon''_r=0.015$  and  $\mu''_r=0.01$  are the exact values).

Fig. 12 shows a cross section of the microstrip in the Z-plane and the W-plane. The effective permittivity can be determined from the measurements of microstrip lines, however, the effective permittivity is a function of both  $\epsilon_g$  and  $H_e$  which are two unknowns. Thus, it is necessary to measure two different microstrip lines

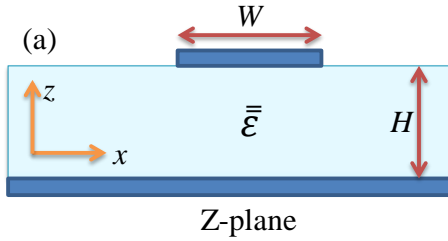


Fig.12: Cross section of (a) microstrip on isotropic substrate

to find two different effective permittivity values, then it is possible to solve the unknowns, such as  $\epsilon_g$  and  $H_e$ . From the determined  $\epsilon_g$  and  $H_e$ , the anisotropic material permittivity can be found.

$$\epsilon = \begin{bmatrix} \epsilon_x & 0 & 0 \\ 0 & \epsilon_y & 0 \\ 0 & 0 & \epsilon_z \end{bmatrix} \quad \text{where} \quad \begin{cases} \epsilon_x = \epsilon_y \neq \epsilon_z & \text{for uniaxial anisotropic} \\ \epsilon_x \neq \epsilon_y \neq \epsilon_z & \text{for biaxial anisotropic} \end{cases} \quad (9)$$

Since the optical axes of the anisotropic material (not known) and the measurement axes of the measurement system are not the same, the matrix will be in general non-diagonal. Fig. 13 shows the angles between the  $xyz$  and the  $x'y'z'$  system where  $\theta$  is the rotation angle along the  $z$ -axis and that  $\phi$  is the rotation angle of the  $x$ -axis.

For uniaxial anisotropic material, the permittivity tensor can be found from the measured effective permittivity of two different microstrip lines because in-plane permittivity tensor elements are same ( $\epsilon_x=\epsilon_y$ ). However, it is necessary to consider two different propagation directions on the in-plane ( $x$ - $y$  plane) optical axes. One is the  $x$ -axis propagation, and another is the  $y$ -axis propagation. Each propagation direction can be considered as a microstrip line on a uniaxial anisotropic substrate problem.

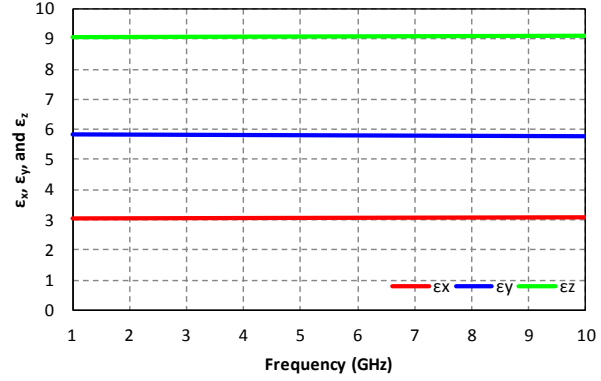


Fig. 14. Simulation result for biaxial anisotropic substrate ( $\epsilon_{xx}=3$ ,  $\epsilon_{yy}=6$  and  $\epsilon_{zz}=9$ )

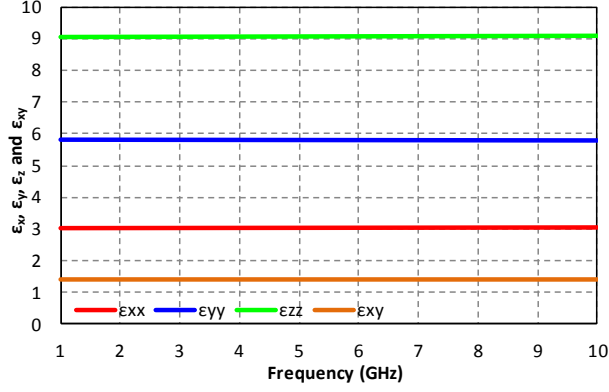
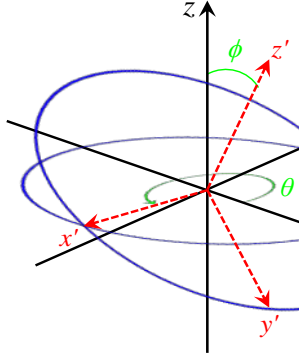


Fig. 13. Misalignment angle (system) and the measurement including  $\epsilon_{xy}$  ( $\epsilon_{xx}=3$ ,  $\epsilon_{yy}=6$ ,  $\epsilon_{zz}=9$ , and  $\epsilon_{xy}=1.5$  are the actual values in the simulation) in the simulation

We tested our method using electromagnetic simulation tools with arbitrary biaxial anisotropic substrate with  $\epsilon_x=3$ ,  $\epsilon_y=3$ , and  $\epsilon_z=9$ . In this simulation, it is assumed that the optical axes of the biaxial anisotropic substrate are known. Fig. 14 shows the simulated result for characterization of biaxial anisotropic substrate. The variation of extracted  $\epsilon_x$  was from 3.044 to 3.081 over the frequency range of 1 GHz to 10 GHz. Also, the extracted values of  $\epsilon_y$  and  $\epsilon_z$  varied from 5.770 to 5.832 and 9.059 to 9.105, respectively. All the extraction results were below 5% of the relative error.

We discussed both uniaxial and biaxial anisotropic material characterization using microstrip lines. The main assumption of the previous analysis was that we knew the optical axes of anisotropic materials. If we still assume that the  $z$ -axis is one optical axis. the permittivity tensor will have non-zero off-diagonal elements and the permittivity tensor is given by:

$$\epsilon = \begin{bmatrix} \epsilon_{xx} & \epsilon_{xy} & 0 \\ \epsilon_{yx} & \epsilon_{yy} & 0 \\ 0 & 0 & \epsilon_{zz} \end{bmatrix} \quad (10)$$

We simulated test structures on an anisotropic substrate that had  $\epsilon_{xx} = 3$ ,  $\epsilon_{yy} = 6$ ,  $\epsilon_{zz} = 9$ , and  $\epsilon_{xy} = 1.5$  with a thickness of 100  $\mu\text{m}$ . Fig. 15 shows the extracted results for  $\epsilon_{xx}$ ,  $\epsilon_{yy}$ ,  $\epsilon_{zz}$ , and  $\epsilon_{xy}$ . The extracted value of  $\epsilon_{xx}$  varied from 3.025 to 3.047 over the frequency range of 1 GHz to 10 GHz. The minimum and maximum errors were 0.846% and 1.571%, respectively. The extracted result for  $\epsilon_{yy}$  varied from 5.817 to 5.792, and  $\epsilon_{zz}$  varied from 9.056 to 9.094. Let us consider the simulated result for off-diagonal element,  $\epsilon_{xy}$ . The extracted value of  $\epsilon_{xy}$  varied from 1.406 to 1.407 over the frequency range of 1 GHz to 10 GHz. The minimum and maximum errors were 6.229% and 6.266%, respectively.

**On-wafer characterization of sapphire film:** A good example of anisotropic thin-film material is a sapphire wafer. The dielectric constants of sapphire are 11.6 for the parallel to the  $c$ -axis and 9.4 for the perpendicular to the  $c$ -axis. Fig. 16 shows a conventional unit cell of a single crystal sapphire with the orientation of  $C$ -plane and  $R$ -plane. The permittivity tensor of  $C$ -plane sapphire wafer is given by:

$$\overline{\overline{\varepsilon}}_C = \begin{bmatrix} 9.4 & 0 & 0 \\ 0 & 9.4 & 0 \\ 0 & 0 & 11.6 \end{bmatrix} \quad (11)$$

The permittivity tensor of *C*-plane sapphire wafer has same form of uniaxial anisotropic permittivity tensor. The permittivity tensor of *R*-plane sapphire wafer can be easily calculated to be:

$$\overline{\overline{\varepsilon}}_R = \begin{bmatrix} 9.4 & 0 & 0 \\ 0 & 10.97 & -0.99 \\ 0 & -0.99 & 10.03 \end{bmatrix} \quad (12)$$

Although, we know the permittivity tensor of *R*-plane sapphire theoretically, it is impossible to build test structures on the wafer perfectly aligned with the optical axes and the measurement axes. Thus, there is a misalignment between the optical axes and the measurement axes. As a result, the permittivity tensor of *R*-plane sapphire wafer will have non-zero off-diagonal elements. For example, if a microstrip line lies on *R*-plane sapphire wafer with in-plane misalignment

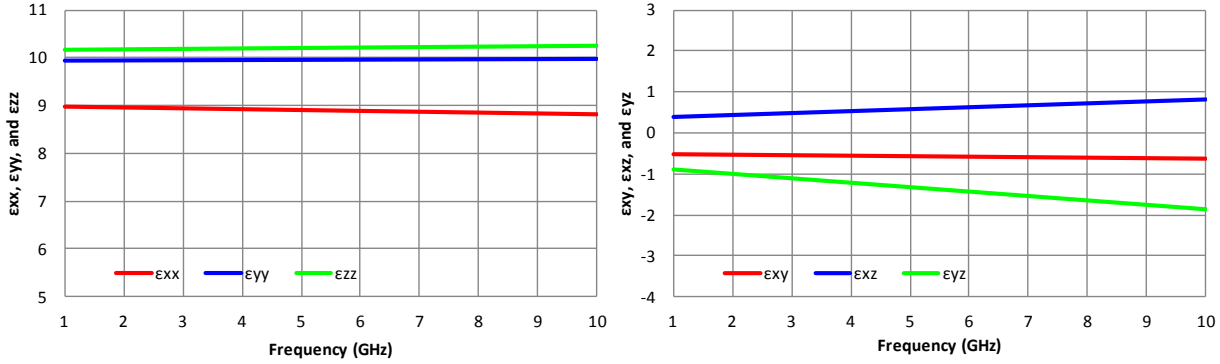


Fig. 17. Simulated results for *R*-plane sapphire wafer with misalignment angles:  $\varepsilon_{xx}=9.6801$ ,  $\varepsilon_{yy}=10.6882$ ,  $\varepsilon_{zz}=10.0316$ ,  $\varepsilon_{xy}=-0.6007$ ,  $\varepsilon_{xz}=0.4206$ , and  $\varepsilon_{yz}=-0.9021$  are the actual values

angle of  $25^\circ$ , the permittivity tensor becomes:

$$\overline{\overline{\varepsilon}} = \begin{bmatrix} 9.6801 & -0.6007 & 0.4206 \\ -0.6007 & 10.6882 & -0.9021 \\ 0.4206 & -0.9021 & 10.0316 \end{bmatrix} \quad (13)$$

We tested our method for characterization of anisotropic material (sapphire) with misalignment angles using electromagnetic simulation tools. In this simulation, we used the permittivity tensor in (13) and Fig. 17 shows the extracted results for all the tensor elements. The extracted value of  $\varepsilon_{xx}$  varied from 8.977 to 8.817 over the frequency range of 1 GHz to 10 GHz. The extracted result for  $\varepsilon_{yy}$  varied from 9.941 to 9.976 and  $\varepsilon_{zz}$  varied from 10.167 to 10.252. The relative errors for the extracted results of diagonal elements are lower

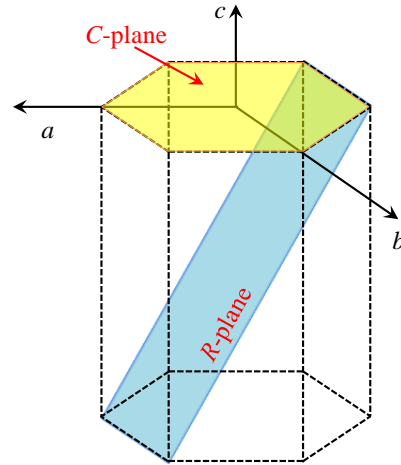


Fig. 16. Orientation of *C*-plane and *R*-plane in the conventional unit cell of a single crystal sapphire ( $a$ ,  $b$ , and  $c$  are the optical axes of sapphire crystal)

than 9%. The extracted results for off-diagonal elements were also close to the exact values in the simulation.

## Prof. Kotov's Group Summary

### Students:

Peter Ho (Ph.D, graduated), Edward Jan (graduated), Dr. Jian Zhu (3rd year)

**Researchers:** Dr. Bong Sup Shim, Dr. Matthew Di Prima, Dr. Shimei Xu

### Journals Papers Submitted/Published

1. S. Srivastava, A. Santos, K. Critchley, K.-S. Kim, P. Podsiadlo, K. Sun, J. Lee, C. Xu, G. D. Lilly, S. C. Glotzer, and N. A. Kotov, Light-Controlled Self-Assembly of Semiconductor Nanoparticles into Twisted Ribbons, *Science*, 2010, 327, 1355 (2010); 1355-1359.
2. G. Daniel Lilly, Yanbin Chen, Xiaoqing Pan and Nicholas A. Kotov, Effect of CdSe Nanoparticles on the Growth of Te Nanowires: Greater Length and Tortuosity and Nonmonotonic Concentration Effect, *J. Phys. Chem. C*, 2010, 114 (6), pp 2428–2433
3. Ming Yang, Kai Sun and Nicholas A. Kotov, Formation and Assembly–Disassembly Processes of ZnO Hexagonal Pyramids Driven by Dipolar and Excluded Volume Interactions, *J. Am. Chem. Soc.*, 2010, 132 (6), pp 1860–1872
4. Jaebeom Lee, Azamat Orazbayev, Alexander O. Govorov and Nicholas A. Kotov
5. *Solvent Effect in Dynamic Superstructures from Au Nanoparticles and CdTe Nanowires: Experimental Observation and Theoretical Description*, *J. Phys. Chem. C*, 2010, 114 (3), pp 1404–1410.
6. Nicholas A. Kotov, Fraud, h-index and Pasternak, *ACS Nano*, 2010, in press (Editorial).
7. Paul Podsiadlo, Ming Qin, Meghan Cuddihy, Jian Zhu, Kevin Critchley, Eugene Kheng, Amit K. Kaushik, Ying Qi, Hyoung-Sug Kim, Si-Tae Noh, Ellen M. Arruda, Anthony M. Waas and Nicholas A. Kotov, Highly Ductile Multilayered Films by Layer-by-Layer Assembly of Oppositely Charged Polyurethanes for Biomedical Applications; *Langmuir*, 2009, 25 (24), pp 14093–14099
8. Ana Sanchez-Iglesias, Marek Grzelczak, Benito Rodriguez-Gonzalez, Ramon A. Alvarez-Puebla, Luis M. Liz-Marzan and Nicholas A. Kotov, Gold Colloids with Unconventional Angled Shapes, *Langmuir*, 2009, 25 (19), pp 11431–11435
9. Bong Sup Shim, Jian Zhu, Edward Jan, Kevin Critchley, Szushen Ho, Paul Podsiadlo, Kai Sun and Nicholas A. Kotov Multiparameter Structural Optimization of Single-Walled Carbon Nanotube Composites: Toward Record Strength, Stiffness, and Toughness, *ACS Nano*, 2009, 3 (7), pp 1711–1722

10. Sudhanshu Srivastava, Paul Podsiadlo, Kevin Critchley, Jian Zhu, Ming Qin, Bong Sup Shim and Nicholas A. Kotov, Single-Walled Carbon Nanotubes Spontaneous Loading into Exponentially Grown LBL Films, *Chem. Mater.*, 2009, 21 (19), pp 4397–4400
11. Libing Wang, Wei Chen, Dinghua Xu, Bong Sup Shim, Yingyue Zhu, Fengxia Sun, Liqiang Liu, Chifang Peng, Zhengyu Jin, Chuanlai Xu and Nicholas A. Kotov, Simple, Rapid, Sensitive, and Versatile SWNT–Paper Sensor for Environmental Toxin Detection Competitive with ELISA, *Nano Lett.*, 2009, 9 (12), pp 4147–4152
12. Edward Jan, Jeffrey L. Hendricks, Vincent Husaini, Sarah M. Richardson-Burns, Andrew Sereno, David C. Martin and Nicholas A. Kotov, Layered Carbon Nanotube-Polyelectrolyte Electrodes Outperform Traditional Neural Interface Materials, *Nano Lett.*, 2009, 9 (12), pp 4012–4018
13. T. P. Vinod, Ming Yang, Jinkwon Kim and Nicholas A. Kotov, Self-Guided One-Sided Metal Reduction in Te Nanowires Leading to Au–Te Matchsticks, *Langmuir*, 2009, 25 (23), pp 13545–13550
14. Nicholas A. Kotov, Politics and Nanotechnology in the Health Care Industry, *ACS Nano*, 2009, 3 (10), pp 2855–2856 (Editorial)
15. Jungwoo Lee, G. Daniel Lilly, R. Christopher Doty, Paul Podsiadlo, Nicholas A. Kotov In vitro Toxicity Testing of Nanoparticles in 3D Cell Culture, *Small*, 2009, 5 (10), pp 1213-1221
16. Jungwoo Lee, Nicholas A. Kotov, Notch Ligand Presenting Acellular 3D Microenvironments for ex vivo Human Hematopoietic Stem-Cell Culture made by Layer-By-Layer Assembly, *Small*, 2009, 5(9), 1008-1013
17. Sara Abalde-Cela, Szushen Ho, Benito Rodríguez-González, Miguel A. Correa-Duarte, Ramón A. Álvarez-Puebla, Luis M. Liz-Marzán, Nicholas A. Kotov Loading of Exponentially Grown LBL Films with Silver Nanoparticles and Their Application to Generalized SERS Detection, *Angewandte Chemie*, 2009, 121(29) pp 5430-5433
18. N. A. Kotov, J. O. Winter, I. P. Clements, E. Jan, B. P. Timko, S. Campidelli, S. Pathak, A. Mazzatenta, C. M. Lieber, M. Prato, R.V. Bellamkonda, G. A. Silva, N. W. S. Kam, F. Patolsky, L. Ballerini, Nanomaterials for Neural Interfaces, *Advanced Materials*, 2009, 21, 1–35.
19. Nicholas A. Kotov, The Collective Behavior of Nanoscale Building Blocks, *ACS Nano*, 2009, 3 (6), pp 1307–1308 (Editorial)
20. Podsiadlo, P.; Arruda, E. M.; Kheng, E.; Waas, A. M.; Lee, J.; Critchley, K.; Qin, M.; Chuang, E.; Kaushik, A. K.; Kim, H.-S.; Qi, Y.; Noh, S.-T.; Kotov, N.A. LBL

Assembled Laminates with Hierarchical Organization from Nano- to Microscale: High-Toughness Nanomaterials and Deformation Imaging, *ACS Nano*, 2009, 3(6), 1564;

21. Chen, W.; Bian, A.; Agarwal, A.; Liu, L.; Shen, H.; Wang, L.; Xu, C.; Kotov, N. A. Nanoparticle Superstructures Made by Polymerase Chain Reaction: Collective Interactions of Nanoparticles and a New Principle for Chiral Materials. *Nano Letters* 2009, 9 (5), pp 2153–2159
22. Kam, N. W. S.; Jan, E.; Kotov, N. A. Electrical Stimulation of Neural Stem Cells Mediated by Humanized Carbon Nanotube Composite Made with Extracellular Matrix Protein. *Nano Letters* 2009, 9(1), 273-278.
23. Sullenbarger, B.; Bahng, J. H.; Gruner, R.; Kotov, N. A.; Lasky, L. C. Prolonged continuous in vitro human platelet production using three-dimensional scaffolds. *Experimental Hematology*, 2009, 37(1), 101-110.
24. Design of Polyurethane-Clay Nanocomposites prepared using Layer-by-Layer
25. Manufacturing Technique, Amit K. Kaushik, Paul Podsiadlo, Ming Qin, Anthony M. Waas, Nicholas A. Kotov, and Ellen M. Arruda, *Macromolecules*, 2009, 42 (17), pp 6588–6595
26. Nicholas A. Kotov, Francesco Stellacci *Frontiers in Nanoparticle Research: Toward Greater Complexity of Structure and Function of Nanomaterials*, *Advanced Materials*, 2008, 20 (22), pp 4221-4222i
27. Srivastava, Sudhanshu; Kotov, Nicholas A.. Composite Layer-by-Layer (LBL) Assembly with Inorganic Nanoparticles and Nanowires. *Accounts of Chemical Research* 2008, 41(12), 1831-1841.
28. Kotov, Nicholas A.; Stellacci, Francesco. *Frontiers in nanoparticle research: toward greater complexity of structure and function of nanomaterials*. *Advanced Materials* 2008, 20(22), 4221-4222.
29. Tang, Zhiyong; Podsiadlo, Paul; Shim, Bong Sup; Lee, Jungwoo; Kotov, Nicholas A.. The effect of stabilizer density on transformation of CdTe nanoparticles induced by Ag cations. *Advanced Functional Materials* 2008, 18(23), 3801-3808.
30. Kotov, Nicholas A.; Tang, Zhiyong. One- and two-dimensional assemblies of nanoparticles: mechanisms of formation and functionality. *Annual Review of Nano Research* 2008, 2 345-375.
31. Vozar, Steven; Poh, Yeh-Chuin; Serbowicz, Thomas; Bachner, Matthew; Podsiadlo, Paul; Qin, Ming; Verploegen, Eric; Kotov, Nicholas; Hart, A. John. Automated spin-assisted layer-by-layer assembly of nanocomposites. *Rev. Sci. Instrum.* 2009, 80, 023903

32. Szushen Ho, Kevin Critchley, G. Daniel Lilly, Bongsup Shim, Nicholas A. Kotov, Free flow electrophoresis for the separation of CdTe nanoparticles, *J. Mater. Chem.*, 2009, **19**, 1390 – 1394.
33. J. E. Nichols, J. Cortiella, J. Lee, J. A. Niles, M. Cuddihy, S. Wang, J. Bielitzki, A. Cantu, R. Mlcak, E. Valdivia, R. Yancy, M. L. McClure, and N. A. Kotov In vitro analog of human bone marrow from 3D scaffolds with biomimetic inverted colloidal crystal geometry, *Biomaterials*, 2009, 30 (6), p.1071-1079.
34. Park, Heung-Shik; Agarwal, Ashish; Kotov, Nicholas A.; Lavrentovich, Oleg D. Controllable Side-by-Side and End-to-End Assembly of Au Nanorods by Lyotropic Chromonic Materials. *Langmuir* 2008, 24(24), 13833-13837.
35. Shim, Bong Sup; Chen, Wei; Doty, Chris; Xu, Chuanlai; Kotov, Nicholas A.. Smart Electronic Yarns and Wearable Fabrics for Human Biomonitoring made by Carbon Nanotube Coating with Polyelectrolytes. *Nano Letters*, 2008, 8(12), 4151-4157.
36. Popovtzer, Rachela; Agrawal, Ashish; Kotov, Nicholas A.; Popovtzer, Aron; Balter, James; Carey, Thomas E.; Kopelman, Raoul. Targeted Gold Nanoparticles Enable Molecular CT Imaging of Cancer. *Nano Letters*, 2008, 8(12), 4593-4596.
37. Lee, Jaebeom; Kim, Hyong-Jun; Chen, Ting; Lee, Kangwon; Kim, Ki-Sub; Glotzer, Sharon C.; Kim, Jinsang; Kotov, Nicholas A.. Control of Energy Transfer to CdTe Nanowires via Conjugated Polymer Orientation. *Journal of Physical Chemistry*, (2009), 113(1), 109-116.
38. Loh, K. J.; Lynch, J. P.; Shim, B. S.; Kotov, N. A.. Tailoring piezoresistive sensitivity of multilayer carbon nanotube composite strain sensors. *Journal of Intelligent Material Systems and Structures*, 2008, 19(7), 747-764.
39. N'Gom, Moussa; Ringnalda, Jan; Mansfield, John F.; Agarwal, Ashish; Kotov, Nicholas; Zaluzec, Nestor J.; Norris, Theodore B. Single Particle Plasmon Spectroscopy of Silver Nanowires and Gold Nanorods. *Nano Letters*, 2008, 8(10), 3200-3204.
40. J. V. Williams, P. E. Savage, N. A. Kotov, A Rapid Hot-injection Method for the Improved Hydrothermal Synthesis of CdSe Nanoparticles, *Industrial & Engineering Chemistry Research*, 2009
41. D. Taylor, M. Michel, R. C. Sekol, J. M. Kizuka, N. A. Kotov, and L. T. Thompson, Fuel Cell Membrane Electrode Assemblies Fabricated by Layer-By-Layer Electrostatic Self Assembly Techniques, *Advanced Functional Materials*, 2008, 18(21) 3154.
42. Podsiadlo, P.; Michel, M.; Lee, J.W.; Verploegen, E.; Wong S. K., N. ; Lee, J.; Qi, Y.; Hart, A.; Hammond, P.; Kotov, N.A. Exponential Growth of LBL Films with Incorporated Inorganic Sheets, *Nano Letters*, 2008, 8(6) 1762-1770.

43. Podsiadlo, P.; Kaushik, A.; Shim, B.S.; Agarwal, A.; Tang, Z.; Waas, A.; Arruda, E.; Kotov, N. A., Can Nature's Design be Improved Upon? High Strength Transparent Nacre-Like Nanocomposites; *Journal of Physical Chemistry C*, 2008, 112(46), 14359-14363.
44. E. Jan, S. J. Byrne, M. Cuddihy, A. M. Davies, Y. Volkov, Y.K. Gun'ko, N. A. Kotov, High-Content Screening as a Universal Tool for Fingerprinting of Cytotoxicity of Nanoparticles, *ACS Nano* , 2008, 2(5), 928-938.
45. Agarwal, A.; Lilly, G.; Govorov, A.; Kotov, N.; Optical Emission and Energy Transfer in Nanoparticle-Nanorod Assemblies: Potential Energy Pump System for Negative Refractive Index Materials, *Journal of Physical Chemistry C*, 2008, 112(47), 18314-18320.
46. Chamberland, D. L.; Agarwal, A.; Kotov, N.; Fowlkes, J. B.; Carson, P. L.; Wang, X. Photoacoustic tomography of joints aided by an etanercept-conjugated gold nanoparticle contrast agent-an ex vivo preliminary rat study. *Nanotechnology* 2008, 19(9), 095101/1-095101/7.
47. Srivastava, S.; Ball, V.; Podsiadlo, P.; Lee, J.; Ho, .; Kotov, N. A.. Reversible Loading and Unloading of Nanoparticles in "Exponentially" Growing Polyelectrolyte LBL Films. *Journal of the American Chemical Society* 2008, 130(12), 3748-3749.
48. Jung Woo Lee, Meghan J. Cuddihy and Nicholas A. Kotov, Three-Dimensional Cell Culture Matrices: State of the Art, *Tissue Engineering B*, 2008, 14(1), 61-86.
49. Meghan J. Cuddihy and Nicholas A. Kotov, Poly(lactic-co-glycolic acid) Bone Scaffolds with Inverted Colloidal Crystal Geometry, *Tissue Engineering*, 2008, 14(10) 1639-1649.
50. Lilly, G. D.; Lee, J.; Sun, K.; Tang, Z.; Kim, K.-S.; Kotov, N. A.. Media Effect on CdTe Nanowire Growth: Mechanism of Self-Assembly, Ostwald Ripening, and Control of NW Geometry. *Journal of Physical Chemistry C*, 2008, 112(2), 370-377.
51. Podsiadlo, P.; Sinani, V. A.; Bahng, J. H.; Kam, N. W. S.; Lee, J.; Kotov, N. A.. Gold Nanoparticles Enhance the Anti-Leukemia Action of a 6-Mercaptopurine Chemotherapeutic Agent. *Langmuir* 2008, 24(2), 568-574.
52. Sullenbarger, B., Bangh J., Rivera, B., Bzdafka, L., Golemlbiewski, M., Kotov, N. A. Lasky, L. 3D and bioreactor expansion of human embryonic stem cells as a prelude to use in blood cell production, *Transfusion*, 2007 47 (3), pp. 40A-40A Suppl. S SEP.
53. A. Agarwal A., Huang S. W., O'Donnell M., Day K.C., Day M., Kotov N., Ashkenazi S. Targeted gold nanorod contrast agent for prostate cancer detection by photoacoustic imaging, *Journal of Applied Physics*, 2007, 102, 064701

54. Podsiadlo P., Kaushik A. K., Arruda E. M., Waas A. M., Shim B. S., Xu J., Nandivada H., Pumplin B. G., Lahann J., **Ramamoorthy A.**, Kotov N. A., Ultrastrong and Stiff Layered Polymer Nanocomposites, *Science*, 2007, 318, 80-83.
55. Shanbhag S., Tang Z., Kotov N.A., Self-Organization of Te Nanorods into V-shaped Assemblies: A Brownian Dynamics Study and Experimental Insights, *ACS Nano*, 2007, 1, 2, 126-133.
56. Michel M., Taylor A., Sekol R, Podsiadlo P., Thompson L.; Kotov N. A. High Performance, Nanostructured Membrane Electrode Assemblies for Fuel Cells Made by Layer-By-Layer Assembly of Carbon Nanocolloids, *Advanced Materials*, 2007, 19(22), 3859.
57. Bong Sup Shim, Zhiyong Tang, Matthew P. Morabito, Nicholas A. Kotov, Integration of conductivity, transparency and mechanical strength in highly homogeneous LBL Composites of SWNT, *Chemistry of Materials*, 2007, 19(23), 5467-5474.
58. Shim, B. S., Podsiadlo P., Lilly D., Agarwal A., Tang Z., Ho S., Ingle P., Patterson D., Lu W., Kotov N. A., Nanostructured Thin Films made by Dewetting Method Of Layer-By-Layer Assembly, *Nano Letters* 2007, 7(11), 3266-3273.
59. Govorov A. O., Lee, J., Kotov N. A., Theory of plasmon-enhanced Förster energy transfer in optically-excited semiconductor and metal nanoparticles, *Physics Review B*, 2007, 76, 12, 125308/1-125308/16
60. Geeta Mehta, Mark J. Kiel, Sean J. Morrison, Jung Woo Lee, Nicholas Kotov, Jennifer J. Linderman, Shuichi Takayama; Polyelectrolyte-Clay-Protein Layer Films on Microfluidics PDMS Bioreactor Surfaces for Primary Murine Bone Marrow Culture, *Adv. Funct. Mater.*, 2007, 17, 2701-2709.
61. Loh, K. J.; Lynch, J. P.; Shim, B. S.; Kotov, N. An Optimization of Multilayer Carbon Nanotube-Polymer Composite Strain Sensors, *Journal of Intelligent Material Systems and Structures*, 2008, 19, p.747.
62. Kim, Kang; Huang, Sheng-Wen; Ashkenazi, Shai; O'Donnell, Matthew; Agarwal, Ashish; Kotov, Nicholas A.; Denny, Michael F.; Kaplan, Mariana J. Photoacoustic imaging of early inflammatory response using gold nanorods. *Applied Physics Letters* 2007, 90(22), 223901/1-223901/3
63. Liu Y., Wang S., Krouse J., Kotov N. A., Eghtedari M., Vargas G., Motamedi M., Rapid aqueous photo-polymerization route to polymer and polymer-composite hydrogel 3D inverted colloidal crystal scaffolds, *Journal of Biomedical Materials Research Part A*, 2007, 83A(1), 1-9.

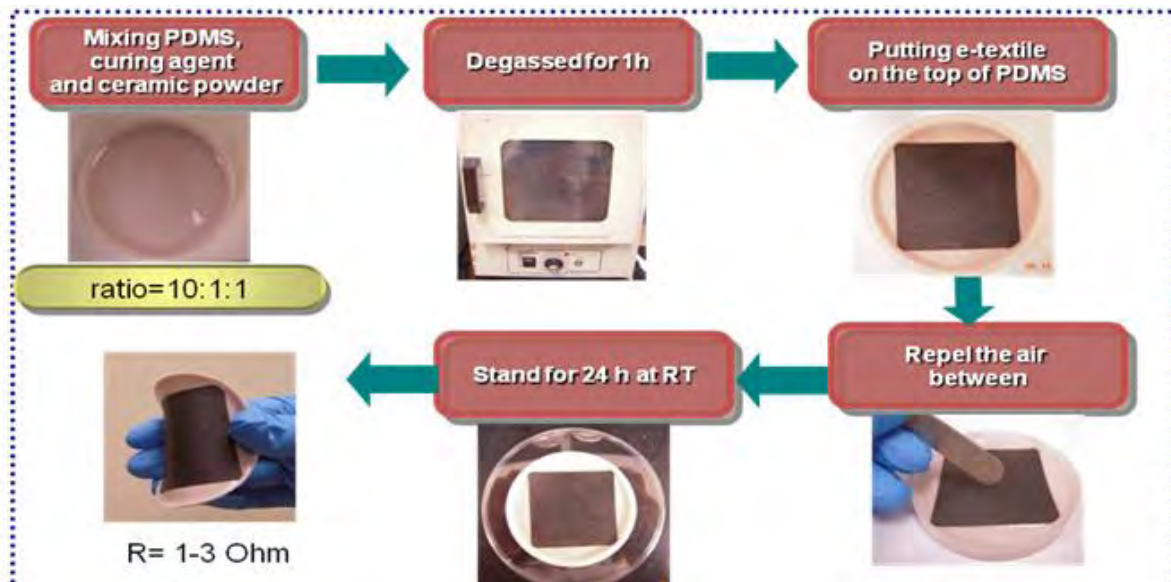
64. Zhenli Zhang, Zhiyong Tang, Nicholas A. Kotov, Sharon Glotzer, Simulations and Analysis of Self-Assembly of CdTe Nanoparticles into Wires and Sheets, *Nano Letters*, 2007 7(6), 1670-1675
65. Podsiadlo, Paul; Sui, Lang; Elkasabi, Yaseen; Burgardt, Peter; Lee, Jaebeom; Miryala, Ashwini; Kusumaatmaja, Winardi; Carman, Mary R.; Shtein, Max; Kieffer, John; Lahann, Joerg; Kotov, Nicholas A.. Layer-by-Layer Assembled Films of Cellulose Nanowires with Antireflective Properties. *Langmuir* 2007, 23(15), 7901-7906.
66. Mohammad Eghtedari, Andre Conjusteau, John A. Copland, Nicholas A. Kotov, Alexander Oraevsky, Massoud Motamedi, High Sensitivity of In Vivo Detection of Gold Nanorods Using a Laser Optoacoustic Imaging System, *Nano Letters*, 2007 7(7), 1914-1918.
67. K. Kim, Kang; S.-W. Huang, S. Ashkenazi, M. O'Donnell, A. Agarwal, N. A. Kotov, M. F. Denny, M. J. Kaplan, Photoacoustic imaging of early inflammatory response using gold nanorods, *Applied Physics Letters* 2007, 90(22), 223901/1-223901/3.
68. Paul Podsiadlo, Zhiyong Tang, Bong Sup Shim, Nicholas A. Kotov, Counterintuitive Effect of Molecular Strength and Role of Molecular Rigidity on Mechanical Properties of Layer-By-Layer Assembled Nanocomposites, *Nano Letters*, 2007, 7(5), 1224-1231
69. P. Podsiadlo, Z. Liu, D. Paterson, P. B. Messersmith, N. A. Kotov, Fusion of Seashell
70. Nacre and Marine Bioadhesive Analogs: High-Strength Nanocomposite by Layer-by-Layer Assembly of Clay and L-3,4-Dihydroxyphenylalanine Polymer, *Advanced Materials*, 2007, 19(7), 949-955.
71. Jan, Edward, Kotov, Nicholas A. Successful Differentiation of Mouse Neural Stem Cells on Layer-by-Layer Assembled Single-Walled Carbon Nanotube Composite, *Nano Letters*, 2007, 7(5), 1123-1128.
72. Jaebeom Lee, Pedro Hernandez, Jungwoo Lee, Alexander O. Govorov, Nicholas A. Kotov, Exciton-plasmon interactions in molecular spring assemblies of nanowires and wavelength-based protein detection, *Nature Materials*, 2007, 6(4), 291-295.
73. Skirtach, Andre G.; De Geest, Bruno G.; Mamedov, Arif; Antipov, Alexei A.; Kotov, Nicholas A.; Sukhorukov, Gleb B. Ultrasound stimulated release and catalysis using polyelectrolyte multilayer capsules. *Journal of Materials Chemistry* 2007, 17(11), 1050-1054.
74. De Geest, B. D., Skirtach A. G.; Mamedov, A.A.; Antipov, A. A.; Kotov N. A.; De Smedt, S. C.; Sukhorukov, G. B.; Ultrasound-Triggered Release from Multilayered Capsules, *Small*, 2007 3(5), 804-808.

75. Juandria V. Williams, Ying Wang, Phillip E. Savage and Nicholas A. Kotov, Synthesis of CdSe Nanocrystals in High-temperature Water, *Industrial & Engineering Chemistry Research* 2007, 46(13), 4358-4362
76. Pappas, T. C.; Wickramanyake, W. M. S.; Jan, E.; Motamedi, M.; Brodwick, M.; Kotov, N. A. Nanoscale Engineering of a Cellular Interface with Semiconductor Nanoparticle Films for Photoelectric Stimulation of Neurons. *Nano Letters* 2007 7(2), 513-519.
77. Loh, K. J.; Kim, J.; Lynch, J. P.; Kam, N. W. S. Kotov, N. A. Multifunctional Layer-by-Layer Carbon Nanotube-Polyelectrolyte Thin Films for Strain and Corrosion Sensing, *Smart Mater. Struct.* 16 2007, 429-438

#### **Conferences Papers Submitted/Published**

1. Edward Jan, N. A. Kotov. Neural Implants from Carbon Nanotubes, MRS Meeting, Boston, 2009
2. N. A. Kotov, Jung Woo Lee, M.C. Cuddihy, Development of 3D Cell Scaffolds, MICOT, April 2009
3. N. A. Kotov, Jung Woo Lee, M.C. Cuddihy, Development of 3D Cell Scaffolds, Michigan Toxicology Society Meeting, May 2009.
4. M.C. Cuddihy, N. A. Kotov, Jung Woo Lee, , Tissue Engineering in 3D Cell Scaffolds, MichBio, April 2009
5. Jung Woo Lee, M.C. Cuddihy, N. A. Kotov, Development of 3D Cell Scaffolds, CHI Tissue Engineering August 2009.,
6. Anyaogu, K. C.; Kotov, N.A. New Technology of Transparent Armor Based on Polymer Composites. Institute for Defense and Government Advancement's 4th Annual Military Armor Protection. McLean, Virginia, June 2009.
7. Anyaogu, K. C.; Kotov, N.A. Advanced Materials for Military Applications: Potentials of Nanotechnology in Armor Technology. Institute for Defense and Government Advancement's 9th Annual Next Generation Materials for Defense. Washington, DC, November 2009.
8. Anyaogu, K. C.; Kotov, N.A. New Materials for Military Vehicles: Potentials of Nanotechnology in Armor Technology. Institute for Defense and Government Advancements 8th Annual Light Armored Vehicles & Stryker Summit. Vienna, Virginia, November 2009.
9. Ye, J. Y.; N'Gom, M.; Chang, Y. C.; Agarwal, A.; Kotov, N.; Baker, J. R.; Norris, T. B., Correlation Spectroscopy of Third-Harmonic Generation by Single Nanorods. In *Conference on Lasers and Electro-Optics*, Baltimore, MD, 2009.
10. Park, H. S.; Lavrentovich, O.; Agarwal, A.; Kotov, N., Self-assembled Au nanorods-polymer composites. In *American Physical Society*, Pittsburgh, PA, 2009.
11. N'gom, M.; Ye, J. Y.; Norris, T. B.; Agarwal, A.; Kotov, N., Enhanced Surface Third Harmonic Generation from Gold Nanorods. In *Conference on Lasers and Electro-Optics*, Baltimore, MD, 2009.
12. Fontana, J.; Palffy-Muhoray, P.; Agarwal, A.; Kotov, N., The Alignment of Gold Nanorods in Macroscopic Domains. In *American Physical Society*, Pittsburgh, PA, 2009.

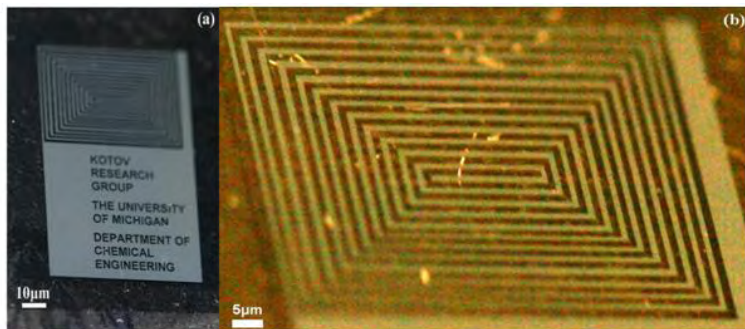
13. Agarwal, A.; Lilly, G. D.; Govorov, A. O.; Kotov, N. A., Optical Emission and Energy Transfer in Nanoparticle- Nanorod Assemblies: Potential Energy Pump System for Negative Refractive Index Materials. In *Materials Research Society*, Boston, MA, 2009.
14. Agarwal, A.; Kotov, N. A., Polyurethane Gold Nanorod Chiral Nanocomposites. In *Materials Research Society*, Boston, MA, 2009.
15. Formation and Assembly-Disassembly Processes of ZnO Hexagonal Pyramids Driven by Dipolar and Excluded Volume Interactions (Ming Yang, Kai Sun and Nicholas A. Kotov)
16. Gold on the Corner of ZnO Hexagonal Pyramids (Ming Yang and Nicholas A. Kotov)
17. June 2009: Gordon Research Conference, "Supramolecules & Assemblies, Chemistry of Products and Processes via Self-Assembly" Sudhanshu Srivastava, N. A. Kotov.
18. November 2009: AIChE Conference, "Self-Assembly of Semiconductor Nanoparticles Mimicking Biomolecules" Sudhanshu Srivastava
19. November 2009: AIChE Conference, "Exponential" Layer-by-Layer Polymer Films for Loading and Assembly of Nanoscale Materials" Sudhanshu Srivastava
20. November 2009: AIChE Conference, "Self-Assembly of CdTe Nanoparticles with DNA and Proteins" Sudhanshu Srivastava
21. December 2009: Materials Research Society, "Light-Controlled Self-Assembly of Semiconductor Nanoparticles into Twisted Ribbons" Sudhanshu Srivastava
22. December 2009: Materials Research Society, "Layer-by-Layer "Exponential" Polymer Films for Loading, Unloading and Assembly of Nanoscale Materials" Sudhanshu Srivastava
23. Jian Zhu, Bong Sup Shim, Nicholas A. Kotov. "Ultrastrong, Conductive and Transparent Composites through Layer-by-Layer Assembly of Sulfonated polyetheretherketone stabilized Single-Walled Carbon Nanotubes and Hydroethyl Cellulose", Nov 2009, AIChE Annual Meeting
24. June 2009: Gordon Research Conference, "Carbon Nanotube Nanostructures E. Jan, N. A. Kotov.
25. N. A. Kotov MRS Meeting Boston 2009, Self-Organization of Nanoparticles. December 1,
26. N. A. Kotov MURI Meeting Kent State University , Chiral Nanostructures, November 21, 2009
27. N. A. Kotov AFOSR meeting, July 21, 2009. Ultrastrong Composites.
28. N. A. Kotov, Nanoparticles and Plasmonic structures, Dresden, April 17 2009.
29. N. A. Kotov MRS Meeting, San Francisco, April 2009, Neural Implants from Carbon nanotubes.
30. N. A. Kotov, International Workshop on Nanowires of Semiconductors, May 2009.



### Research Summary

The following major research breakthroughs were made in this project.

1. The method of the production of conducting textiles was developed (Figure 1).
2. Conductivity of the SWNT composites reached  $5 \times 10^5 \text{ S/cm}$ .
3. High frequency conductivity was evaluated and found identical to that at low frequencies.
4. Direct write approach to antenna preparation was achieved (Fig.2)
5. Textiles and fibers with the conductivity of copper were developed.



## Prof. Shtein's Group Summary

Michigan: e-fibers – Shtein (PI),  
Morris (Ph.D. Student)

### Posters:

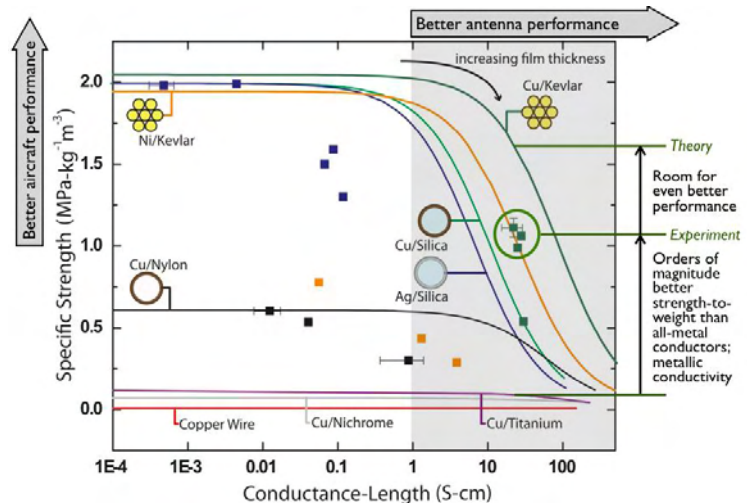
1. S.E. Morris, K. Pipe, M. Shtein, "High Strength Metallized Fibers and Yarns", MRS, Dec 2009
2. S.E. Morris, M. Shtein, "High-strength electrically conductive fibers and yarns for OLED-based solid-state lighting", Michigan AVS Symposium, May 2010

### Papers:

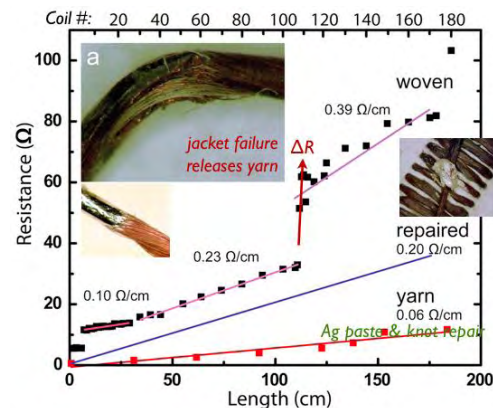
1. S.E. Morris, et al., "High-Strength, Metalized Fibers for Conformal Load Bearing Antenna Applications" IEEE Antennas and Propagation Trans, 2011

We had 3 major accomplishments:

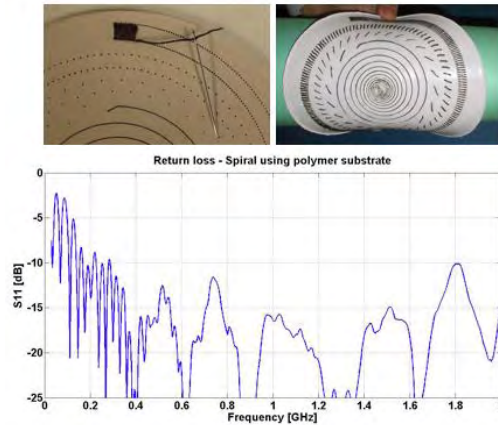
- 1) We quantitatively mapped the theoretical limits of multi-functional performance (strength-to-weight versus electrical conductivity) of the e-fibers relevant for UAV structural antenna applications
- 2) We produced copper-coated, multi-strand kevlar fibers exhibiting extremely high strength-to-weight ratios in combination with metallic conductivity
- 3) We successfully realized for the first time a flexible, stretchable, woven broadband antenna using these e-fibers.



Our calculations (**Fig. MS1**) show that such multi-filament geometries should be vastly superior to conventional all-metal wires when multi-functionality is desired, such as in structurally integrated antennas for small UAV applications. Copper coated on multi-strand Kevlar fibers yields excellent performance (i.e. sufficiently high conductivity for an antenna, and retains the high strength-to-weight ratio of the substrate fiber), while use of higher strength substrates, such as Nylon is expected to yield even better performance.



Using copper-coated kevlar fibers, we demonstrated for the first time a woven, flexible and stretchable, broadband antenna. We quantified the effect of weaving on the electrical and mechanical characteristics of the e-fibers (**Fig. MS2**). We discovered that considerable mechanical stress placed on the e-fiber during the weaving process can result in a decrease of electrical conductivity, as well as breakage. We developed an encapsulating strategy to maintain fiber integrity throughout the weaving process, and also showed that the fiber can be repaired in situ if breakages occur.



Subsequently, when the woven antennas were tested by OSU, the frequency response (**Fig. MS3**) of the broadband antenna clearly showed the great potential of the multi-material fiber architecture, expected to yield vastly improved performance over conventional conductors for load-bearing applications.

This work resulted in a poster presentation at the Fall 2009 MRS meeting (poster was nominated for an award), and a joint publication with the Bayram and Volakis groups at OSU (in preparation).

## **Prof. Ghosh's Group Summary**

### **Graduate Student Supported:**

Hyun Sik Kwon, Ph.D. student

Shu Guo, Ph.D student

### **Publications:**

#### **Journals Papers**

1. H. S. Kwon and S. Ghosh, "*A Multi-time scale Induced Coupled Electro-Magnetic Structural Dynamics Finite Element Model for RF Applications*", in preparation.
2. H. S. Kwon, P. Ramesh, G. N. Washington and S. Ghosh, "*An Experimentally Validated Finite Element Model for Deforming Antenna*", in preparation
3. S. Guo and S. Ghosh, "*Coupled Electro-Magnetic Structural Dynamics Finite Element Model for RF Applications*", in preparation.
4. S. Guo and S. Ghosh, "*A Multi-time scale Induced Coupled Electro-Magnetic Structural Dynamics Finite Element Model*", in preparation.

### **RESEARCH SUMMARY**

In this project, we have developed a coupled electromagnetic-mechanical finite element model that incorporates a large deformation low frequency mechanical vibration module in the ultra-high frequency (UHF) electromagnetic field response. In this simulation, a staggered coupling scheme is applied. In each time step, the mechanical displacement, which is assumed to be independent to electromagnetic field by ignoring the Lorentz force, is solved first. Then the electromagnetic field, which is influenced by mechanical deformation, is solved in total Lagrangian method to overcome complicated boundary shape. This scheme can obtain accurate results and also eliminate unnecessary sacrifice in calculation. In this case, the electromagnetic field in free space in which the hyper-elastic conductor is embedded is very important. But the mesh in free space can be entanglement due to the large deformation. So a mesh adaptive method, R-method is proposed in this project.

The coupling of the two disparate fields (mechanical and electro-magnetic) has a physical limitation for UHF, since the electro-magnetic wavelength from UHF is much shorter than the antenna constitution. As such, the structural dimension cannot be traversed in a period of electromagnetic field. An important objective that has been executed throughout the research is to propose a multi-time scale modeling for physical phenomena at two very different driving frequencies that result in a significant scale difference. The multi-time scale models being developed is proposed to resolve this frequency difference. Various modules developed in this task are outlined below.

#### **1. Computational Modeling of the Electro-Magnetic Fields using a Weak Form of the Maxwell's equation**

The computational modeling contains two dependent fields, mechanical vibration and electromagnetic response. To better illustrate the idea of load bearing antenna, large deformation assumption is considered in the mechanical field part. We apply Saint Venant-Kirchhoff model as the hyperelastic constitutive model

$$\underline{\underline{S}} = \lambda \cdot \text{tr}(\underline{\underline{E}}) + 2\mu \cdot \underline{\underline{E}} \quad (1.1)$$

$$W(\underline{\underline{E}}) = \frac{\lambda}{2} \cdot [\text{tr}(\underline{\underline{E}})]^2 + \mu \cdot \text{tr}(\underline{\underline{E}}^2) \quad (1.2)$$

$$\underline{\underline{S}} = \frac{\partial W}{\partial \underline{\underline{E}}} \quad (1.3)$$

$$\underline{\underline{E}} = \frac{1}{2} \left[ \frac{\partial \underline{u}}{\partial \underline{X}} + \left( \frac{\partial \underline{u}}{\partial \underline{X}} \right)^T + \left( \frac{\partial \underline{u}}{\partial \underline{X}} \right)^T \frac{\partial \underline{u}}{\partial \underline{X}} \right] \quad (1.4)$$

Here  $\underline{\underline{S}}$  is 2nd Piola-Kirchhoff stress tensor,  $\underline{\underline{E}}$  is Lagrangian Green strain tensor,  $W$  is strain energy density function,  $\underline{u}$  is the displacement,  $\lambda$  and  $\mu$  are Lamé constraints.

Construct potential energy of the mechanical field of the system as,

$$\Pi(\underline{u}) = \int_{\Omega_o} W(\underline{\underline{C}}(\underline{u})) dV - \int_{\Omega_o} \underline{u}^T \rho_o \underline{b} dV - \int_{\partial\Omega_o} \underline{u}^T \underline{t}_o dS \quad (1.5)$$

Here  $\underline{t}_o$  is the traction,  $\underline{b}$  is the body force.

Then do the variation of it, obtain the weak form of the mechanical field,

$$\delta \Pi(\underline{u}) = \int_{\Omega_o} (\delta \underline{u}^T \rho_o \underline{\dot{v}}) dV + \int_{\Omega_o} (\delta \underline{\underline{F}}^T \cdot \underline{\underline{P}}) dV - \int_{\Omega_o} (\delta \underline{u}^T \rho_o \underline{b}) dV - \int_{\partial\Omega_o} \delta \underline{u}^T \underline{t}_o dS = 0 \quad (1.6)$$

With the weak form, we discretize the domain. Fixed the right edge and apply a sinusoidal loading, as shown in Figure 1.

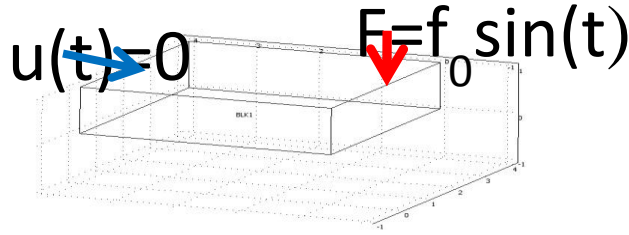
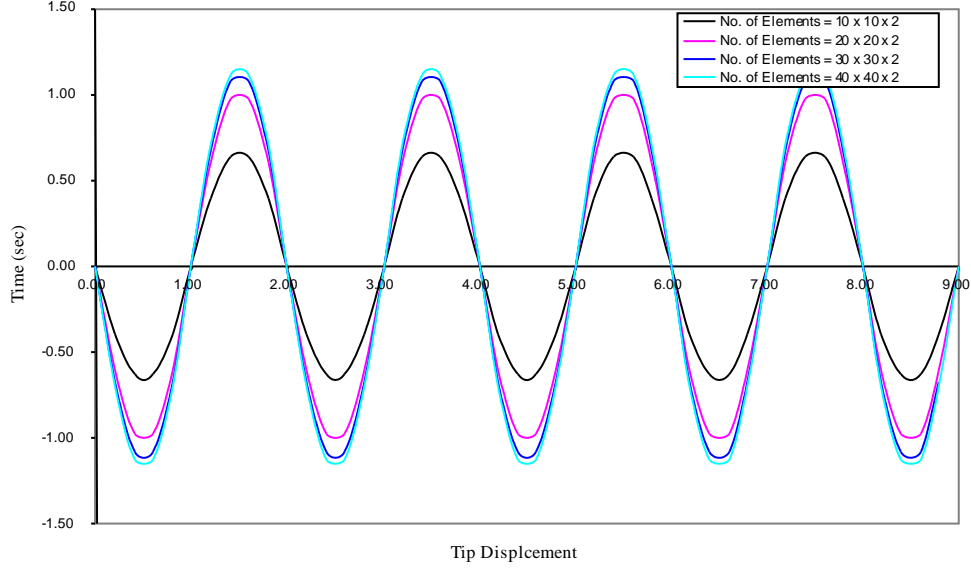


Figure 1. Mechanical excitation on conductor's edge

We note that convergence is related to the number of elements. Figure 2 gives the tip displacement convergence information. In this simulation, the most important part is to assign time dependent electromagnetic field according to mechanical excitation. To accomplish commercial software's incapability in solving multi-physics simulation, we have developed the coupled electromagnetic and mechanical finite element model not only with quasi-static assumption but also the transient problem.



*Figure 2. Tip displacement in finite element model with different number of elements*

We start with Maxwell equation,

$$\nabla \cdot (\underline{b}(\underline{x}, t)) = 0 \quad (1.7)$$

$$\nabla \cdot (\underline{d}(\underline{x}, t)) = q_e \quad (1.8)$$

$$\nabla \times \underline{h}(\underline{x}, t) = \frac{\partial \underline{d}(\underline{x}, t)}{\partial t} + \underline{j}(\underline{x}, t) \quad (1.9)$$

$$\nabla \times \underline{e}(\underline{x}, t) = -\frac{\partial \underline{b}(\underline{x}, t)}{\partial t} \quad (1.10)$$

where  $\underline{d}$  is electric flux density vector,  $\underline{e}$  is electric field intensity vector,  $\underline{b}$  is magnetic flux density vector,  $\underline{h}$  is magnetic field intensity vector,  $\underline{j}$  is electric current density vector and  $q_e$  is electric charge density. Since the model is described as a load bearing antenna, the boundary of the structure would change significantly during deformation. Thus, to achieve an efficient algorithm, total Lagrangian method is adopted. In this case, the configuration employed to calculate the electromagnetic field is always reference configuration. In order to connect current configuration, which is the deformed configuration, to reference configuration is Nanson's formula as shown following,

$$dv = JdV \quad (1.11)$$

$$\underline{n}ds = J(\underline{N} \bullet \underline{F}^{-1})dS \quad (1.12)$$

$$J = \det(\underline{\underline{F}}) \quad (1.13)$$

Here the small characters stand for the current configuration, and the capital characters stand for the reference configuration.  $\underline{n}$  is the normal vector.  $v$  and  $s$  are the volume and surface of the domain, separately. Integrate the Maxwell's equations and apply the Nanson's formula, we obtain a set of Maxwell's equations of reference configuration,

$$\nabla \cdot (\underline{B}(\underline{X}, t)) = 0 \quad (1.14)$$

$$\nabla \cdot (\underline{D}(\underline{X}, t)) = Q_e \quad (1.15)$$

$$\nabla \times \underline{H}(\underline{X}, t) = \frac{\partial \underline{D}(\underline{X}, t)}{\partial t} + \underline{J}(\underline{X}, t) \quad (1.16)$$

$$\nabla \times \underline{E}(\underline{X}, t) = -\frac{\partial \underline{B}(\underline{X}, t)}{\partial t} \quad (1.17)$$

Capital characters indicate the variables in reference configuration. Although there are no formal definitions, the relationship between the variables of current configuration and reference configuration are,

$$\underline{B}(\underline{X}, t) \equiv J \underline{\underline{F}}^{-1} \underline{b}(\underline{x}, t) \quad (1.18)$$

$$\underline{D}(\underline{X}, t) \equiv J \underline{\underline{F}}^{-1} \underline{d}(\underline{x}, t) \quad (1.19)$$

$$\underline{E}(\underline{X}, t) \equiv \left( \underline{e}(\underline{x}(\underline{X}, t), t) + \frac{d\underline{x}(\underline{X}, t)}{dt} \times \underline{b}(\underline{x}(\underline{X}, t), t) \right) \underline{\underline{F}} \quad (1.20)$$

The electromagnetic field responses affected by mechanical vibrations is observed by this simulation. For UHF case, the wavelength of the electromagnetic field is much shorter than antenna structural dimension. One period of electromagnetic field of UHF does not cover a whole structure. UHF electromagnetic field varies within an antenna structure. This means that the quasi-static assumption which is usually applied to electric mechanical device should not be considered for this particular application. Our simulation assumption is that (1) mechanical vibration and electromagnetic field are not history dependent, and (2) conductor material does not have memory, that is non-dielectric, and has no surface current and charge density. Moreover, to simplify the electromagnetic response, vector potential  $A$  and scalar potential  $\Phi$  are introduced. They are defined as,

$$\underline{E} = -\nabla \Phi - \frac{\partial \underline{A}}{\partial t} \quad (1.18)$$

$$\underline{B} = \nabla \times \underline{A} \quad (1.19)$$

If we also assume that no surface charge density exists, Maxwell's equations in reference configuration become,

$$\underline{D}(\underline{X}, t) = \varepsilon_0 J \left\{ -\underline{\nabla} \Phi - \underline{\dot{A}} - (\underline{F}^{-1} \bullet \underline{\dot{u}}) \times (\underline{\nabla} \times \underline{A}) \right\} \bullet \underline{C}^{-1} \quad (1.20)$$

$$\underline{H}(\underline{X}, t) = \left[ \left( \varepsilon_0 J \left\{ -\underline{\nabla} \Phi - \underline{\dot{A}} - (\underline{F}^{-1} \bullet \underline{\dot{u}}) \times (\underline{\nabla} \times \underline{A}) \right\} \bullet \underline{C}^{-1} \right) \times (\underline{F}^{-1} \bullet \underline{\dot{u}}) + \frac{1}{\mu_0 J} \{ (\underline{\nabla} \times \underline{A}) \bullet \underline{C} \} \right] \quad (1.21)$$

With these two governing equations of electromagnetic field coupled with mechanical excitation, the weak form si give by

$$\begin{aligned} \Pi(\delta \Phi) &= \int_{\partial V} \underline{N} \bullet \left[ \varepsilon_0 J \left\{ -\underline{\nabla} \Phi - \underline{\dot{A}} - (\underline{F}^{-1} \bullet \underline{\dot{u}}) \times (\underline{\nabla} \times \underline{A}) \right\} \bullet \underline{C}^{-1} \right] \delta \Phi dS \\ &- \int_V \left[ \varepsilon_0 J \left\{ -\underline{\nabla} \Phi - \underline{\dot{A}} - (\underline{F}^{-1} \bullet \underline{\dot{u}}) \times (\underline{\nabla} \times \underline{A}) \right\} \bullet \underline{C}^{-1} \right] \bullet (\underline{\nabla} \delta \Phi) dV = 0 \end{aligned} \quad (1.23)$$

$$\begin{aligned} \Pi(\delta \underline{A}) &= \int_V \frac{d}{dt} \left[ \varepsilon_0 J \left\{ -\underline{\nabla} \Phi - \underline{\dot{A}} - (\underline{F}^{-1} \bullet \underline{\dot{u}}) \times (\underline{\nabla} \times \underline{A}) \right\} \bullet \underline{C}^{-1} \right] \bullet \delta \underline{A} dV + \\ &- \int_{\partial V} \left( \underline{N} \times \left[ \varepsilon_0 J \left\{ -\underline{\nabla} \Phi - \underline{\dot{A}} - (\underline{F}^{-1} \bullet \underline{\dot{u}}) \times (\underline{\nabla} \times \underline{A}) \right\} \bullet \underline{C}^{-1} \right] \times (\underline{F}^{-1} \bullet \underline{\dot{u}}) + \frac{1}{\mu_0 J} \{ (\underline{\nabla} \times \underline{A}) \bullet \underline{C} \} \right) \bullet \delta \underline{A} dS \\ &- \int_V \left[ \left( \varepsilon_0 J \left\{ -\underline{\nabla} \Phi - \underline{\dot{A}} - (\underline{F}^{-1} \bullet \underline{\dot{u}}) \times (\underline{\nabla} \times \underline{A}) \right\} \bullet \underline{C}^{-1} \right) \times (\underline{F}^{-1} \bullet \underline{\dot{u}}) + \frac{1}{\mu_0 J} \{ (\underline{\nabla} \times \underline{A}) \bullet \underline{C} \} \right] \bullet (\underline{\nabla} \times \delta \underline{A}) dV \\ &+ \int_V \sigma J \left[ \left\{ -\underline{\nabla} \Phi - \underline{\dot{A}} - (\underline{F}^{-1} \bullet \underline{\dot{u}}) \times (\underline{\nabla} \times \underline{A}) \right\} \bullet \underline{C}^{-1} \right] \bullet \delta \underline{A} dV = 0 \end{aligned} \quad (1.24)$$

Here  $\varepsilon_0$  is free space permittivity,  $\mu_0$  is free space permeability,  $\underline{F}$  is the deformation gradient,  $\underline{C}$  is the right Cauchy strain tensor, and  $j$  is  $\det(\underline{F})$ ,  $\rho_0$  is material density,  $\underline{b}_0$  is a gravitational body force,  $\underline{f}_L$  is Lorentz force,  $\underline{t}$  is a surface traction. And  $\delta \Phi$  and  $\delta \underline{A}$  are arbitrary fields.

Along with the variation with respect to displacement as equation (1.6), the coupled mechanism is described completely.

To validate the governing equation of electromagnetic field, one can appeal to commercial software by switch off the mechanical excitation. Although it cannot support transient analysis, the stable value is also useful to compare. Figure 3 shows the comparison of our codes' results and COMSOL's result. The variable we are interested in are the magnetic and electric field

generated by constant current input in certain direction. Note the DOF also influence the convergences as we discussed in mechanical field.

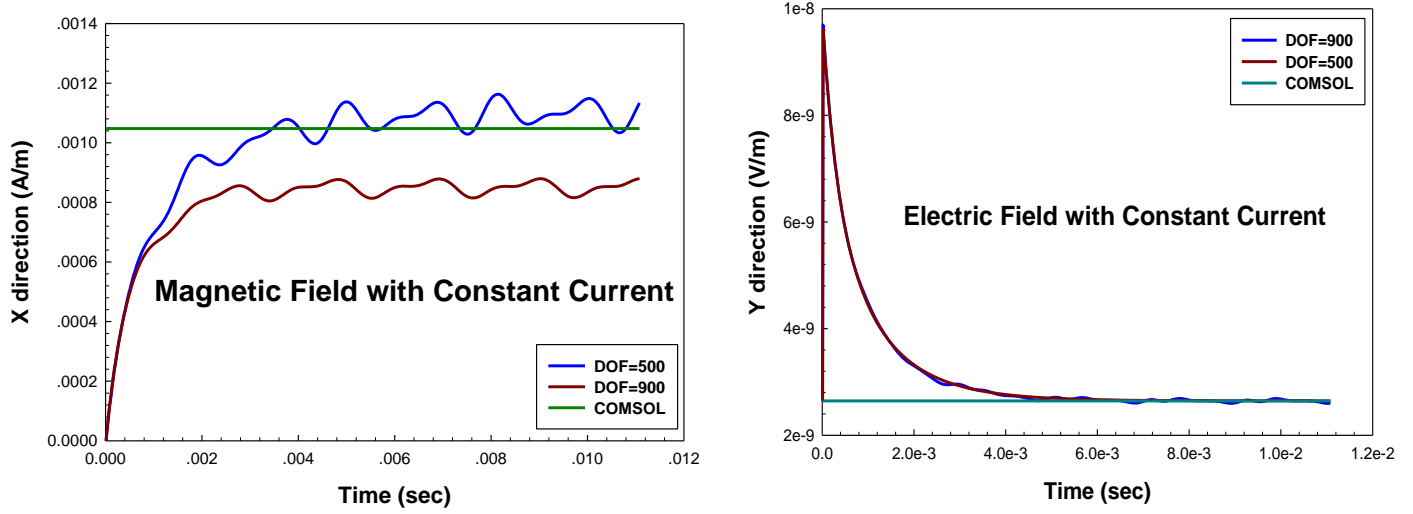


*Figure 3. Magnetic and electric field generated by constant current under sinusoidal vibration results and comparison with COMSOL*

From Figure 3, we note that the result is much closer to that of the commercial codes. And we can add the response from mechanical excitation which COMSOL cannot fully compatible. Till now, the problem of coupled electromagnetic and mechanical field simulation is complete in algorithm.

## 2. Modeling Free Space Domain Using R-method for Node Relocation

The load bearing antenna on an air foil or body of aerial undergoes mechanical vibrations caused by external excitation which moves in free space, as shown in Figure 4,

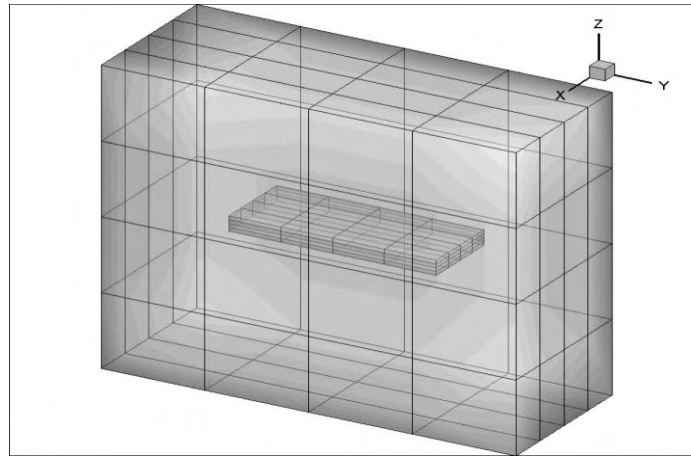


*Figure 4. Antenna structure swims in free space*

As we noted before, the governing equation for mechanical vibration is in the Lagrangian reference system, while the Maxwell equations for the electro-magnetic field are in Eulerian reference system. Directly coupling these different frameworks for coupled transient responses creates inappropriate computational domains. If governing equations in the Lagrangian and Eulerian reference systems are coupled, inaccurate data transfer can occur across the surfaces of the conducting material and free space. Thus, we have transformed Maxwell's equations in the format of Eulerian to Lagrangian type. This causes mesh entanglement when the mesh of the deforming antenna structure interferes with the static grid for the free space. This mesh distortion and entanglement leads to a negative Jacobian in the finite element transformation. This causes a failure in computations. To overcome this problem, a local node relocation method or r-method, is applied to retain mesh integrity. After one time step of computation for mechanical deformation, nodes around surfaces of conducting material are re-located according to how much nodes on surfaces of conductor move. Then, for newly located nodes of free space, nodal interpolation is conducted for scalar and vector potential variables for electromagnetic field computation. This node relocation scheme is shown in Figure 5.

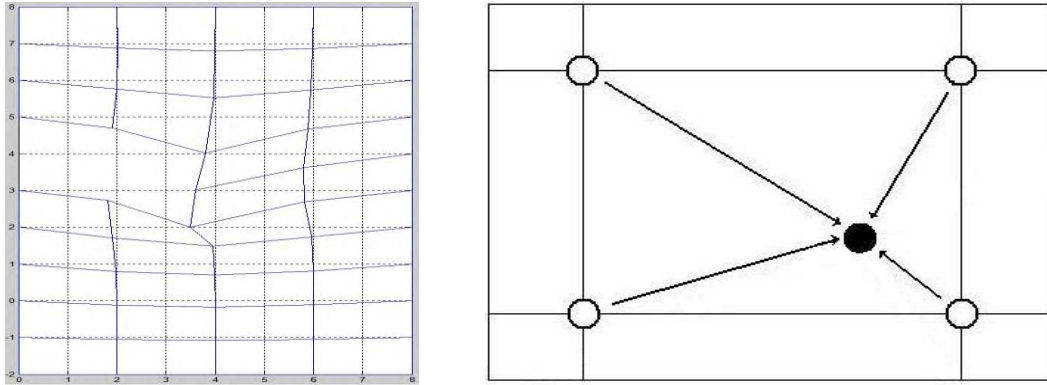


*Figure 5. Nodal re-location and interpolation: Newly located node (Solid circle) is interpolated by previous nodal information.*

### 3. Multi-Time Scale Modeling for Coupling Mechanical and Electro-Magnetic Fields

An important part of this research is multi-time scale modeling for coupling different physical phenomena governed by disparate frequency responses. It is prohibitive to simulate mechanical and electromagnetic time-responses in ultra high frequency scale for a finite element analysis modeling. To overcome this computational difficulty, the multi-time scale modeling for electromagnetic fields is proposed to separate single time response into time-averaged response, a function of coarse time scale, and fine time response, a function of coarse time and fine time scales. Time-averaged coarse time scale and fine time scale responses for electromagnetic field are simulated in each time scale respectively with a staggered method.

The idea of the multi-time scale modeling is to separate a variable, a function of  $t$  (coarse time) and  $\tau$  (fine time), into two variables. One is a function of only  $t$  and may be periodic in a coarse time scale. The other is a function of  $t$  and  $\tau$  and almost periodic in the fine time scale. Applying variable separations and respective assumptions on a governing equation separates the governing equation into two or more in accordance with an increased number of variables. After time averaging over coarse time scale, the governing equation becomes a coarse time response equation

driven by averaged fine time responses. As an example, suppose that governing equation is the second time derivative equation.

$$a_1(t) \cdot \ddot{y} + a_2(t) \cdot \dot{y} + a_3(t) \cdot y = f(t) \quad (3.1)$$

Define a scaling factor,  $\varsigma$ , a variable,  $y$ , time derivatives and a time averaging operator  $\langle \rangle$ , the relationship between them are,

$$t = \varsigma \cdot \tau, \varsigma \gg 1, y^\varepsilon(t, \tau) = M(t) + y(t, \tau) \quad (3.2)$$

The corresponding inter-scale time derivatives are given as,

$$\dot{y} = \frac{\partial y}{\partial t} + \frac{1}{\varsigma} \frac{\partial y}{\partial \tau} \quad (3.3)$$

$$\ddot{y} = \frac{\partial^2 y}{\partial t^2} + \frac{2}{\varsigma} \frac{\partial^2 y}{\partial t \partial \tau} + \frac{1}{\varsigma^2} \frac{\partial^2 y}{\partial \tau^2} \quad (3.4)$$

$$\langle y^\varepsilon(t, \tau) \rangle = \langle M(t) \rangle + \langle y(t, \tau) \rangle = M(t) + \langle y(t, \tau) \rangle \quad (3.5)$$

Now, applying equations (5) - (8) to (4), (4) yields an averaged governing equation as,

$$a_1(t) \cdot \frac{\partial^2 M(t)}{\partial t^2} + a_2(t) \cdot \frac{\partial M(t)}{\partial t} + a_3(t) \cdot M(t) = -a_2(t) \cdot \frac{\partial \langle y(t, \tau) \rangle}{\partial t} - a_3(t) \cdot \langle y(t, \tau) \rangle \quad (3.6)$$

Equation (3.6) is a coarse time response equation and is simulated with a fine time response in staggered method. We are currently working on the implementation of this algorithm for the coupled EM-ME problem.

#### 4. Code Parallelization for High Performance Computing

To carry out the FEM, an open source academic code, FEAP is utilized here. Based on this platform, we developed our own code to achieve this project. Since the coupled electromagnetic and mechanical finite element modeling contains conducting material domain as well as free space domain, it is essential to construct a code parallelization to speed up a simulation running time. For mechanical finite element model, a large deformation model is considered with Periodic vibrations and non-iterative solver is used to solve the transient problem. As the output from the Mechanical Domain is the input to the Electro-Magnetic Domain, it is extremely essential for us to adopt domain decomposition techniques in Mechanical part too. The following paragraphs deals with the procedures adopted to implement the parallel code in Mechanical Domain for a better performance.

To develop the parallel implement, a serial input file initially provided to FEAP is sub-divided into desired number of partitions depending on the number of processors to be used. For example, if we wish to run the code on 4 processors then we need to divide the entire domain into

four parts so that each processor will have its separate input file. (Par)METIS has been used for efficient domain decomposition as shown in schematic diagram.

Then we construct the solution algorithm for wide variety of applications. PETSC, a mathematical algorithm aided by MPI for communicating information between different processors for efficient performance is appealed. We have also used Prometheus which can be integrated easily with PETSC libraries, as it resulted in extensive speed up. At last, the graphical and numerical outputs of the results are executed in parallel, either. Figure 6 shows the schematic representation of the parallel computation with FEAP.

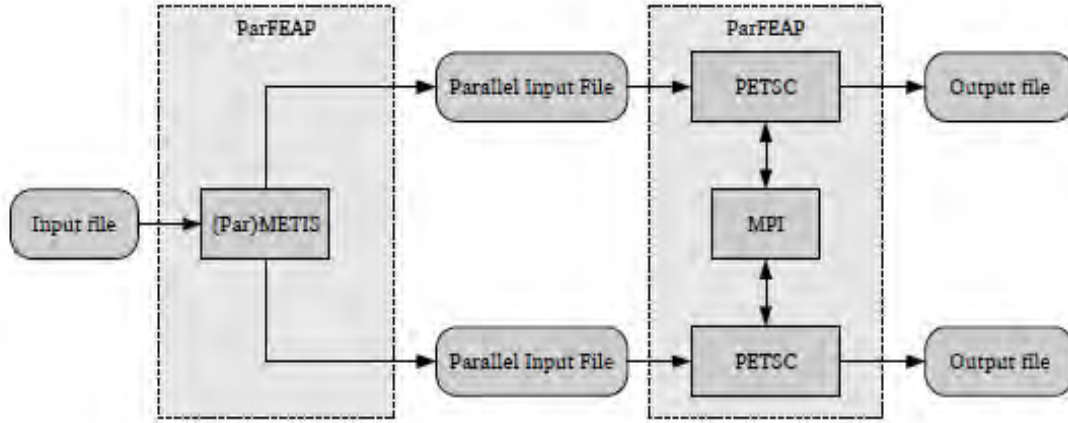


Figure 6. Schematic representation of the parallel computation with FEAP.

After implementing the parallel code, we could successfully analyze the problem for 10000 elements where as the earlier serial version used only 225 elements and was comparatively slower. The results clearly showed improvement with the increase in number of processors. The result below displays the time taken by the processors in solving the Mechanical Domain for the first 1000 time steps.

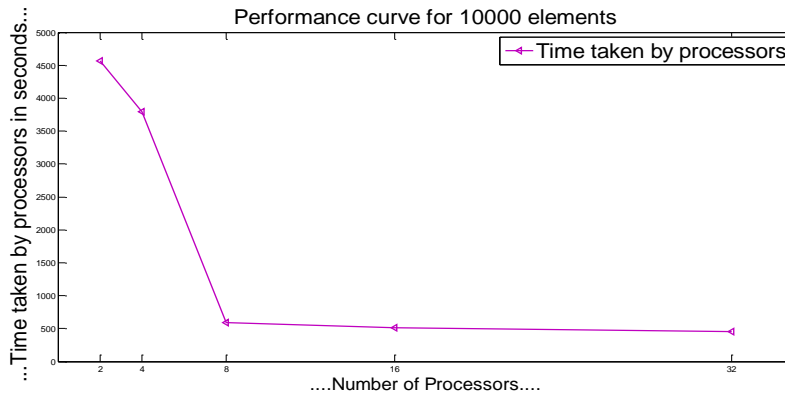


Figure 7. Performance of certain model taken out by different number of processors

We were also successful in coupling the Mechanical and Electro-Magnetic field on a common platform. The performance curve for coupled problem for 10000 elements in the first 10 steps is shown below. We are currently working on the Electro-Magnetic code to improve its performance.

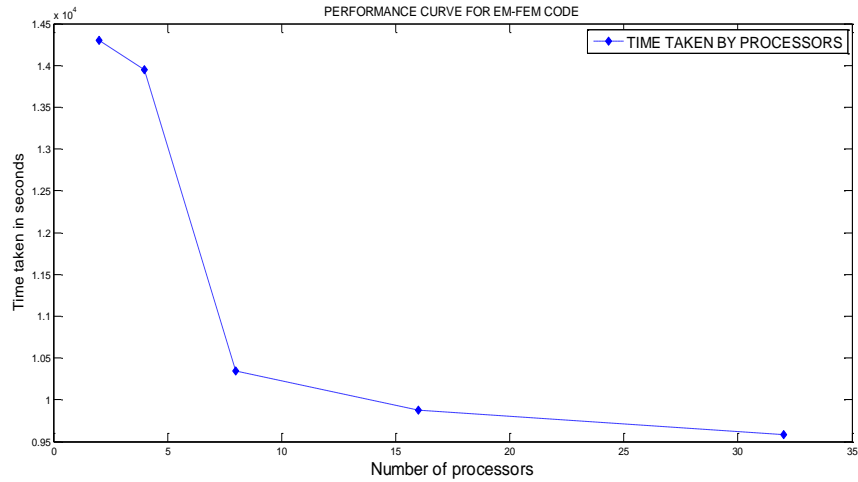


Figure 8. Performance of EM-FEM model taken out by different number of processors

For validation purpose, we had selected a particular node number and tried to compare the displacements in the Z-direction for the first five time steps. The results proved to match exactly as shown below.

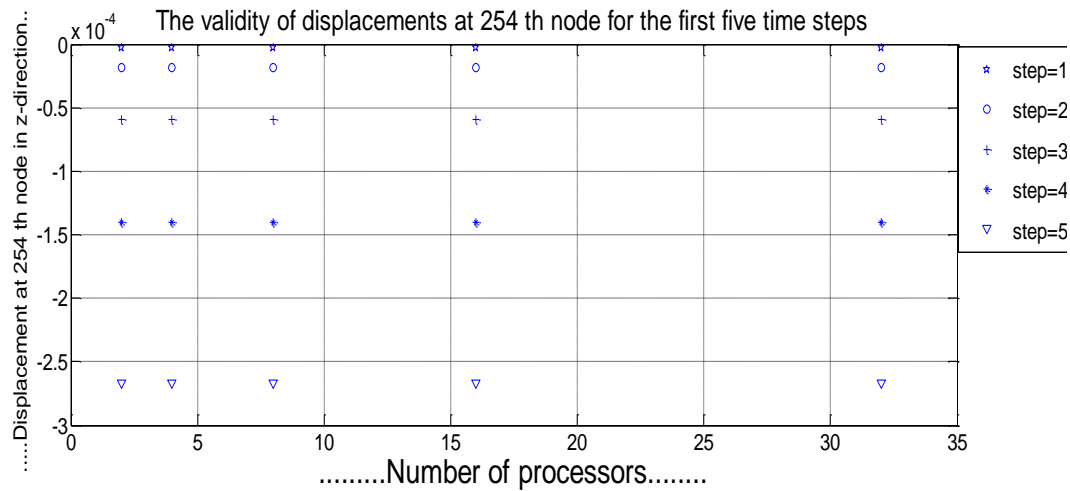


Figure 9. Finite Element simulation taken out by different number of processors

## **Prof. Bechtel 's Group Summary**

**Students:** Sushma Santapuri (Ph.D, 3<sup>rd</sup> year), Robert L. Lowe (Ph.D, 4<sup>th</sup> year), Sarvani Piratla (M.S., Graduated, Currently pursuing Ph.D at Cornell University)

### **Journal and Conference Papers Submitted/Published:**

[1] F. Ahmadkhanlou, M. Mahboob, S.E. Bechtel and G.N. Washington Experiments and Models of the Magneto Rheological Behavior of High Weight Percent Suspensions of Carbonyl Iron Particles in Silicone Oil” Journal of Fluids Engineering, 130, 121301 (2008).

[2] F. Ahmadkhanlou, M. Mahboob, G. N. Washington, and S.E. Bechtel, “An improved Model for Magnetorheological Fluid-Based Actuators and Sensors”, Journal of Intelligent Material Systems and Structures, Vol. 21, No. 1, 3-18 (2010)

[3] F. Ahmadkhanlou, M. Mahboob, G.N. Washington, and S.E. Bechtel, “Modeling and Control of Equation Chapter 1 Section 1 Multi-Degree of Freedom Magnetorheological Fluid-Based Haptic Systems for Telerobotic Surgery”, to be submitted to International Journal of Medical Robotics and Computer Assisted Surgery

[4] Farzad Ahmadkhanlou, Gregory N. Washington, and Stephen Bechtel “Variable Resistance MR Fluid- Based Knee Braces”, submitted to Medical Engineering and Physics, 2009

[5] S.Piratla, S.E. Bechtel, R.L. Lowe and M. Dapino, “ Fully-Coupled Characterization of Rate-Independent Thermo-Electro-Magneto-Mechanical Materials”, (in preparation)

[6] S.Sushma and S.E.Bechtels, “ Model-Based Optimization of Coupled Electro-Magneto-Thermo-Mechanical Behavior of Load-Bearing Antennas” Submitted to ASME International Mechanical Engineering Congress & Exposition, Vancouver, BC , November 2010

### **Research Summary:**

Load-bearing antennas are multi-functional sensing (actuating) and receiving (detecting) devices that are integrated with a load-bearing structure. These antennas are highly appealing for military applications, importantly Unmanned Aerial Vehicles. In the present work, we have developed analytical techniques and computational tools for multi-scale, multi-physics modeling of composite load-bearing antennas. The antenna structure is subjected to mechanical forces, temperature gradients, and electromagnetic fields, giving rise to highly coupled non-linear electro-magneto-thermo-mechanical (EMTM) behavior. Our model, based predominantly on first principles, employs the thermo-mechanical governing equations (i.e., conservation of mass, momentum, angular momentum, energy and second law of thermodynamics) coupled with Maxwell's equations. The macro-scale coupling terms for the thermo-mechanical and electro-magnetic interactions are deduced from micro-scale behavior. Our modeling has identified 92 non-dimensional numbers which quantify the competition between physical effects in the operation of load-bearing antenna. Depending on the design of the structure and nature of the excitation, only a subset of physical effects will be dominant, which dictates the appropriate computational model. A fixed relative ordering among all competing effects determines a “regime” of antenna/environment interaction. The mathematical structure of leading order equations for various physical regimes is

presented for use in analysis and optimization of the coupled electro-magneto-thermo-mechanical behavior of load bearing antennas. Catalog of practical regimes of behavior and corresponding model equations are presented and results are analyzed.

### Research Accomplishments:

Our model employs the thermo-mechanical governing equations (i.e., conservation of mass, linear momentum, angular momentum, energy, and the second law of thermodynamics) coupled with Maxwell's equations. The macro-scale coupling terms for the thermo-mechanical and electro-magnetic interactions are deduced from micro-scale behavior. Our first-principle modeling has identified 92 non-dimensional numbers which quantify the competition between competing physical effects in the operation of the load-bearing antenna. Based on antenna structure and environment, we have deduced a framework to optimize the coupled behavior and utilized this framework to present a catalog of all practical regimes. The mathematical structures of most relevant regimes are deduced and solutions are analyzed.

Governing equations have been presented in a non-dimensional form, for example Ampere's law:

$$\nabla \times \mathbf{e}^* = -\frac{\partial \mathbf{b}}{\partial t} - \nabla \times (\mathbf{b} \times \mathbf{v}),$$

$$B_{32} \frac{\partial e_3^*}{\partial x_2} - B_{23} \frac{\partial e_2^*}{\partial x_3} = -\frac{\partial e_1^*}{\partial t} - D_1 (\nabla \times (\mathbf{b} \times \mathbf{v}))_1$$

and the energy conservation law is:

$$\rho \dot{\epsilon} = \rho r^{ext} + \rho r^e - \nabla \cdot \mathbf{q} + \mathbf{T} \cdot \mathbf{L},$$

$$\rho \frac{\partial \epsilon}{\partial t} = \sum_j \sum_i K_{ij} \rho V_{i,j} T_{ij} - L_i \mathbf{q}_{i,i} + M \rho r^e + N \rho r^{ext}$$

where,

$$B_{3,2} = \frac{e_{3o}^* t_{eo}}{e_{1o}^* x_{2o}}, \quad D_1 = \frac{(\nabla \times (\mathbf{b} \times \mathbf{v}))_1 t_{eo}}{e_{1o}^*}, \quad K_{12} = \frac{t_{m0} T_{12o} V_{1o}}{\rho_o x_{2o} \epsilon_0}, \quad L_1 = \frac{q_{1o} t_{m0}}{\rho_o x_{1o} \epsilon_0}, \quad M = \frac{r_o^{ext} t_{m0}}{\epsilon_0} \text{ and } N = \frac{r_o^e t_{m0}}{\epsilon_0}$$

The characteristic scales corresponding to the physical quantity are defined in table.3 of [6]. For example,

Charecteristic Scales	Notation
Time scale of electromagnetic phenomena	$t_{e0}$
Time scale of thermo-mechanical phenomena	$t_{m0}$
Length scale in x-direction	$x_{1o}$

All the non-dimensional qunatities involved in the coupled problem are listed below:

$A_1 = \frac{b_{1o}x_{2o}}{b_{2o}x_{1o}}$	$S_1 = \frac{v_{1o}t_{m0}}{x_{1o}}$
$B_{23} = \frac{e_{2o}^*t_{em0}}{x_{3o}b_{1o}}$	$P_1 = \frac{f_{1o}t_{meo}}{v_{1o}}$
$E_1 = \frac{d_{1o}}{x_{1o}\sigma_o}$	$Q_1 = \frac{f_{e1o}t_{m0}}{v_{1o}}$
$G_1 = \frac{\sigma_o v_{1o}t_{em0}}{d_{1o}}$	$R_{12} = \frac{t_{m0}T_{12o}}{v_{1o}\rho_o x_{2o}}$
$J_1 = \frac{j_1t_{e0}}{d_{1o}}$	$K_{12} = \frac{t_{m0}T_{12o}v_{1o}}{\rho_o x_{2o}\varepsilon_0}$
$F_{23} = \frac{h_{2o}^*t_{e0}}{x_{3o}d_{1o}}$	$L_1 = \frac{q_{1o}t_{m0}}{x_{1o}\rho_o\varepsilon_0}$
$D_1 = \frac{[\nabla \times (b \times v)]_{1o}t_{e0}}{b_{1o}}$	$M = \frac{r_o^{ex}t_{m0}}{\varepsilon_0}$
$H_1 = \frac{[\nabla \times (d \times v)]_{1o}t_{e0}}{d_{1o}}$	$N = \frac{r_o^e t_{m0}}{\varepsilon_0}$

Table 1: Non-Dimensional Quantities

We now define a process and design for modeling of load-bearing antenna .

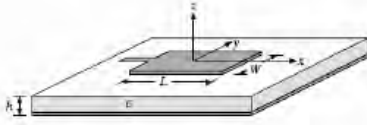


Figure 1: microstrip patch antenna

Designs of load-bearing antenna are largely microstrip antennas. We model a single layer patch antenna and it is further extended to composite layers using hybrid methods.

The following restrictions on coupled electro-magneto-thermo-mechanical behavior defines the process:

- a) A description of microstrip patch antenna is shown in Fig.1. The antenna consists of a dielectric material bounded by a ground plane at one end and a metal surface patch antenna with feedline at the other end. The patch antenna surface is on x-y plane (on the wing of airplane). We assume that the antenna dimensions along x and y  $\gg$  dimensions along z.
- b) Major duration of flight of an air-plane is the cruise mode, where velocity of the air-plane is constant. We assume that this velocity is directed along y-axis and of the order of 100m/s.
- c) Since velocity of air-plane is dominant along the direction of the flight, other components of velocity caused by deformation are of much smaller scales. Aerodynamic thrust and weight of the air-plane are of the order of 10000 N. For a small UAV the scales are smaller.
- d) In defining scales for the electro-magnetic problem it is important to note that the fields vary drastically over the entire domain, so in regime 1, we consider only the fields inside the antenna structure as they contribute to the mechanical forces. Far-fields created by the antenna and the distortions caused by antenna structure are studied in a different regime.

- e) The multi-scale coupled behavior of an LBA requires that the time scales are different for electromagnetic and mechanical problems, since EM fields vary at much faster rates than mechanical fields.

Typical values for charecteristic scales corresponding to this process are deduced as shown in table 2:

Scales	Typical Values (S.I.)
$x_o = x_{1o} = x_{2o}$	$10^{-1}m$
$x_{3o}$	$10^{-3}m = x_o \varepsilon$
$v_o = v_{2o}$	$10^2 m/s$
$v_{1o}$	$10^{-6}m/s = v_o \varepsilon^4$
$v_{3o}$	$10^{-4}m/s = v_o \varepsilon^3$
$t_{e0} = \frac{1}{\omega_o}$	$10^{-10}s$
$t_{m0} = \frac{x_o}{v_o}$	$10^{-4}s$
$e_o = e_{3o}^*$	$10^5 V/m$
$j_o = j_{3o}$	$10^7 A/m^2$
$h_o = h_{1o}^* = h_{2o}^* = \frac{e_o}{X}$	$10^3 A/m$
$d_o = d_{3o} = \epsilon_o e_{3o}^*$	$10^{-7} A/m^2$
$b_o = b_{1o} = b_{2o} = \mu_o$	$10^{-3} T$
$\rho_o$	$10^3 kg/m^3$
$f_o = f_{1o} = f_{2o}$	$100 m/s^2$
$f_{eo} = f_{e1o} = f_{e2o} = \frac{J_o b_o}{\rho_o}$	$10 m/s^2$
$T_o = \frac{F_o}{x_o}$	$10^5 Pa$

Table 2: Non-Dimensional Quantities

These scales provide a relative ordering of the non-dimensional quantities listed in table.

$$\varepsilon = \frac{z_0}{x_0} = 0.01$$

1 in terms of slenderness parameter (  $x_0$  ) and the regime corresponding to this process is defined as:

$$\begin{aligned}
 A_1 &= \bar{A}_1 \varepsilon^0, B_{31} = \bar{B}_{31} \varepsilon^0, B_{32} = \bar{B}_{32} \varepsilon^0, D_1 = \bar{D}_1 \varepsilon^3, D_2 = \bar{D}_2 \varepsilon^3 \\
 F_{21} &= \bar{F}_{21} \varepsilon^{-1}, F_{12} = \bar{F}_{12} \varepsilon^{-1}, H_3 = \bar{H}_3 \varepsilon^3, J_3 = \bar{J}_3 \varepsilon^{-2} \\
 S_{11} &= \bar{S}_{11} \varepsilon^4, S_{12} = S_{32} = \bar{S}_{12} \varepsilon^0, S_{13} = S_{31} = \bar{S}_{13} \varepsilon^2, S_{33} = \bar{S}_{33} \varepsilon^3 \\
 Q_1 &= Q_2 = \bar{Q}_i \varepsilon^{-4}, P_1 = P_2 = \bar{P}_j \varepsilon^{-5}, R_{ij} = \bar{R}_{ij} \varepsilon^{-5}
 \end{aligned}$$

$$\text{where, } \varepsilon < \bar{A}_1, \bar{B}_{31}, \bar{B}_{32}, \bar{D}_1, \bar{D}_2, \bar{F}_{21}, \bar{F}_{12}, \bar{H}_3, \bar{J}_3, \bar{S}_{ij}, \bar{Q}_i, \bar{P}_j, \bar{R}_{ij} < \varepsilon^{-1}$$

Using the scales of the physical parameters derived above, we present the optimized model considering only leading order and first order terms. The electromagnetic model simplifies to 2-D wave equation. By assuming magnetic walls boundary condition and jöt time dependence, the electromagnetic fields are approximated using a cavity resonance model. The optimized model is given by:

$$\frac{\partial^2 e_z}{\partial x^2} + \frac{\partial^2 e_z}{\partial y^2} + \mu \epsilon \omega^2 e_z = j \omega J_z$$

An analytical representation of the solution in terms of eigen-function expansion is given as:

$$e_z = j\omega\mu \sum_{m,n} \frac{1}{k^2 - k_{mn}^2} \frac{\langle J, v_{mn} \rangle}{\langle v_{mn}, v_{mn} \rangle} v_{mn}$$

As inertia effects are negligible, the mechanical model is reduced to linear elastostatic problem. The effects of gravity, electromagnetic coupling force and thrust are dominant. Deformation along z is dominant due to thin plate approximation. By using Hooke's law as the constitutive relation and applying the same procedure as above, a leading order approximation for determination of deformation along z is given by:

$$K\left(\frac{\partial^2 u_z}{\partial x^2} + \frac{\partial^2 u_z}{\partial y^2}\right) = -\rho f_z$$

where, K is a material constant.

It should be noted that these solutions work as an initial estimate to the solution. For better results we need to consider second order corrections as well. We now look into the behavior of a regime where some of the parameters are varied by order of  $\varepsilon$  and study how the governing equations change accordingly. Consider the regime where order of magnitude of electro-magnetic fields is much smaller with frequencies of the order of MHz. The wave equation governing electromagnetic waves is now modified to:

$$\frac{\partial^2 d_z}{\partial x^2} + (1 - \mu\epsilon v_y^2) \frac{\partial^2 d_z}{\partial y^2} + \omega^2 \mu \epsilon d_z - 2i\omega\mu\epsilon v_y \frac{\partial d_z}{\partial y} = i\omega\mu\epsilon J_z^* + \mu\epsilon v_y \frac{\partial J_z^*}{\partial y}$$

**Thermo-mechanical problem:** We have used second law of thermodynamics and Clausius-Duhem inequality to perform a complete combinatorial analysis of 72 possible energy functions to describe the coupled multi-physics behavior. Constitutive equations have been derived from these energy potentials in a rigorous, systematic fashion.

#### Thermo-Electro-Magneto-Mechanical (TEMM) Constitutive Equations:

The standard independent variable pairs and the corresponding potential functions for a thermo-mechanical problem are listed in the table below:

Independent Variables	Potential function
(F, $\eta$ )	$\varepsilon$ – Internal energy
(F, $\theta$ )	$\psi$ - Helmholtz free energy
(P, $\eta$ )	$\chi$ – Enthalpy

(P,  $\theta$ )

$\phi$  – Gibbs free energy

The Helmholtz free energy is a function of mechanical independent variable  $F$  and thermal independent variable  $\theta$ . There are 9 such potentials, for instance:

$$\psi = \psi(\mathbf{F}, \theta, \bar{\mathbf{e}}, \bar{\mathbf{m}})$$

where, the independent electrical and magnetic variables in this case are  $\mathbf{e}$  and  $\mathbf{m}$ , respectively. Calculating the derivative:

$$\begin{aligned}\rho_o \dot{\psi}^{F\theta em} &= \rho_o \frac{\partial \psi^{F\theta em}}{\partial \mathbf{F}} \dot{\mathbf{F}} + \rho_o \frac{\partial \psi^{F\theta em}}{\partial \eta} \dot{\eta} + \rho_o \frac{\partial \psi^{F\theta em}}{\partial \bar{\mathbf{e}}} \dot{\bar{\mathbf{e}}} + \rho_o \frac{\partial \psi^{F\theta em}}{\partial \bar{\mathbf{m}}} \dot{\bar{\mathbf{m}}} \\ \rho_o \psi^{F\theta em} &= \rho_o \varepsilon - \rho_o \eta \theta - \bar{\mathbf{p}} \cdot \bar{\mathbf{e}}, \\ \rho_o \dot{\psi}^{F\theta em} &= \rho_o \dot{\varepsilon} - \rho_o \dot{\eta} \theta - \rho_o \eta \dot{\theta} - \dot{\bar{\mathbf{p}}} \cdot \bar{\mathbf{e}} - \bar{\mathbf{p}} \cdot \dot{\bar{\mathbf{e}}}\end{aligned}$$

These equations combined with second law of thermodynamics give:

$$\begin{aligned} & -(\rho_o \frac{\partial \psi^{F\theta em}}{\partial \mathbf{F}} - (\mathbf{P} + \mathbf{F}^{-T}(\bar{\mathbf{e}} \otimes \bar{\mathbf{p}} + \mu_o \bar{\mathbf{h}} \otimes \bar{\mathbf{m}})) \cdot \dot{\mathbf{F}} - (\rho_o \frac{\partial \psi^{F\theta em}}{\partial \theta} - \rho_o \eta) \dot{\eta} \\ & - (\rho_o \frac{\partial \psi^{F\theta em}}{\partial \bar{\mathbf{e}}} - \bar{\mathbf{p}}) \cdot \dot{\bar{\mathbf{e}}} - (\rho_o \frac{\partial \psi^{F\theta em}}{\partial \bar{\mathbf{m}}} - \mu_o \bar{\mathbf{h}}) \cdot \dot{\bar{\mathbf{m}}} - \frac{Q}{\theta} \cdot \frac{\partial \theta}{\partial X} - \rho_o \xi \theta + \bar{\mathbf{j}} \cdot \bar{\mathbf{e}} = 0 \end{aligned}$$

This equation should hold for all processes, which gives:

$$\begin{aligned}\rho_o \frac{\partial \psi^{F\theta em}}{\partial \mathbf{F}} &= \mathbf{P} + \mathbf{F}^{-T}(\bar{\mathbf{e}} \otimes \bar{\mathbf{p}} + \mu_o \bar{\mathbf{h}} \otimes \bar{\mathbf{m}}), \\ \frac{\partial \psi^{F\theta em}}{\partial \theta} &= -\eta, \\ \rho_o \frac{\partial \psi^{F\theta em}}{\partial \bar{\mathbf{e}}} &= -\bar{\mathbf{p}}, \\ \rho_o \frac{\partial \psi^{F\theta em}}{\partial \bar{\mathbf{m}}} &= \mu_o \bar{\mathbf{h}}.\end{aligned}$$

The remaining dependent variables (electric displacement  $\mathbf{d}$  and magnetic flux  $\mathbf{b}$ ) are deduced from the solution via post-processing. Adherence to this framework ensures consistency of the characterization of the coupled material.

There are 8 pairs of independent variables possible for a thermo-mechanical problem. With three electric variables ( $\mathbf{e}$ ,  $\mathbf{d}$ ,  $\mathbf{p}$ ) and three magnetic variables ( $\mathbf{h}$ ,  $\mathbf{b}$ ,  $\mathbf{m}$ ), 9 combinations are possible for each of these 8 pairs.

In all, there are seventy-two potentials possible for TEMM material

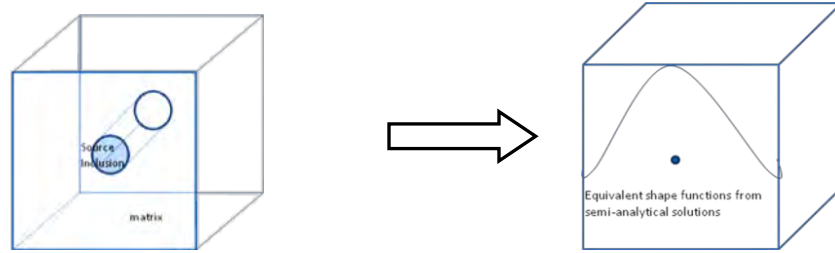
Potential functions							
Family1	Family2	Family3	Family4	Family5	Family6	Family7	Family8
$\varepsilon^{F\eta pm}$	$\eta^{F\varepsilon pm}$	$\psi^{F\theta pm}$	$\theta^{F\psi pm}$	$\chi^{P\eta pm}$	$\eta^{P\chi pm}$	$\phi^{P\theta pm}$	$\theta^{P\phi pm}$
$\varepsilon^{F\eta em}$	$\eta^{F\varepsilon em}$	$\psi^{F\theta em}$	$\theta^{F\psi em}$	$\chi^{P\eta em}$	$\eta^{P\chi em}$	$\phi^{P\theta em}$	$\theta^{P\phi em}$
$\varepsilon^{F\eta ph}$	$\eta^{F\varepsilon ph}$	$\psi^{F\theta ph}$	$\theta^{F\psi ph}$	$\chi^{P\eta ph}$	$\eta^{P\chi ph}$	$\phi^{P\theta ph}$	$\theta^{P\phi ph}$
$\varepsilon^{F\eta eh}$	$\eta^{F\varepsilon eh}$	$\psi^{F\theta eh}$	$\theta^{F\psi eh}$	$\chi^{P\eta eh}$	$\eta^{P\chi eh}$	$\phi^{P\theta eh}$	$\theta^{P\phi eh}$
$\varepsilon^{F\eta dm}$	$\eta^{F\varepsilon dm}$	$\psi^{F\theta dm}$	$\theta^{F\psi dm}$	$\chi^{P\eta dm}$	$\eta^{P\chi dm}$	$\phi^{P\theta dm}$	$\theta^{P\phi dm}$
$\varepsilon^{F\eta pb}$	$\eta^{F\varepsilon pb}$	$\psi^{F\theta pb}$	$\theta^{F\psi pb}$	$\chi^{P\eta pb}$	$\eta^{P\chi pb}$	$\phi^{P\theta pb}$	$\theta^{P\phi pb}$
$\varepsilon^{F\eta dh}$	$\eta^{F\varepsilon dh}$	$\psi^{F\theta dh}$	$\theta^{F\psi dh}$	$\chi^{P\eta dh}$	$\eta^{P\chi dh}$	$\phi^{P\theta dh}$	$\theta^{P\phi dh}$
$\varepsilon^{F\eta eb}$	$\eta^{F\varepsilon eb}$	$\psi^{F\theta eb}$	$\theta^{F\psi eb}$	$\chi^{P\eta eb}$	$\eta^{P\chi eb}$	$\phi^{P\theta eb}$	$\theta^{P\phi eb}$
$\varepsilon^{F\eta db}$	$\eta^{F\varepsilon db}$	$\psi^{F\theta db}$	$\theta^{F\psi db}$	$\chi^{P\eta db}$	$\eta^{P\chi db}$	$\phi^{P\theta db}$	$\theta^{P\phi db}$

### Task 2: A Semi-Analytical Formulation for Multi-Scale Element Development in EM Formulation:

In collaboration with Prof. Ghosh and his team we have worked on development of Multi-Scale-Super-Element for homogenization of microstructural RVE's with parametric forms of boundary conditions with the following properties:

#### Why Super Element?

- 1) Shape functions derived from analytical solutions increases accuracy of simulation
- 2) Inherently accommodates multi-scale inhomogeneity
- 3) Fine discretization of conducting wire is robust, does not take physics into consideration whereas super element method provides a superior modeling technique
- 4) Dependence on analytical solutions allows for parameter study



- 5) Super Element exploits shape functions derived from semi-analytical solutions in improving accuracy and enabling parameter studies for design and optimization problems
- 6) Two-media problem is reduced to single medium using volume equivalence and surface equivalence principles, thus accommodating multi-scale inhomogeneity

We have successfully applied the super-element to a simple 1-D and 2-D problems and deduced the integral equations governing multi-scale EM behavior and we are currently working on integrating it with 3-D problem

## **Prof. Carman's Group Summary**

### **Students:**

Scott Keller (Ph.D, 4<sup>th</sup> year), Tao Wu (Ph.D., 3<sup>rd</sup> year), Previous students involved, Gavin Chang Phd (currently at HRL), T.K. Chung PhD (currently at TSMC), Catherine Kerrigan (currently at Naval Labs)

### **Researchers:**

K. P. Mohanchandra, Alexander Bur

### **Journals Papers Submitted/Published**

1. T. Wu, T.-K. Chung, C.-M. Chang, S. Keller, and G. P. Carman. Influence of electric voltage bias on converse magnetoelectric coefficient in piezofiber/metglas bilayer laminate composites. *Journal of Applied Physics*, 106(5):054114, 2009.
2. T. Wu, M. Emmons, T.-K. Chung, J. Sorge, and G. P. Carman. Influence of mechanical load bias on converse magnetoelectric laminate composites. *Journal of Applied Physics*, 107(9):09D912, 2010.
3. T. Wu, C.-M. Chang, T.-K. Chung, and G. Carman. Comparison of effective direct and converse magnetoelectric effects in laminate composites. *Magnetics, IEEE Transactions on*, 45(10):4333–4336, oct. 2009.
4. T. K. Chung, S. Keller, and G. P. Carman, Electric Field Induced Magnetic Single-Domain Evolution in a Magnetoelectric Thin Film, *Applied Physics Letters*, vol. 94, issue 13, pp. 132501, 2009
5. C.A. Kerrigan, K.K. Ho, K.P. Mohanchandra, G.P. Carman, Sputter deposition and analysis of thin film NiTi/Terfenol-D multilaminate for vibration damping. *Smart Materials and Structures*, Volume: 18 Issue: 1, pp 2009
6. T. K. Chung, G. P. Carman, and K. P. Mohanchandra, Reversible Magnetic Domain-Wall Motion under an Electric Field in a Magnetoelectric Thin Film, *Applied Physics Letters*, vol. 92, issue 11, pp. 112509, 2008

### **Conferences Papers Submitted/Published**

1. Tao Wu, Michael Emmons, Alexandre Bur, Jian Sorge, and Gregory P. Carman, "Magnetoelectric laminate composites with prestress consideration," in *Proceedings of Behavior and Mechanics of Multifunctional Materials and Composites 2010*, San Diego, CA, USA, Mar., 2010, pp. 764415-10.
2. Tao Wu, Michael Emmons, Tien-Kan Chung, Jian Sorge, and Gregory P. Carman, "Influence of mechanical load bias on converse magnetoelectric laminate composites", 11<sup>th</sup> jointed MMM-Intermag Conference, Washington D.C., Jan. 2010
3. Tao Wu, Tien-Kan Chung, and Gregory P. Carman, "Electrical Tuning of Converse Magnetoelectric Effect in Piezo-Fiber/Metglas Laminates," in *Proceedings of the ASME 2009 Conference on Smart Materials, Adaptive Structures and Intelligent Systems (SMASIS2009)*, Oxnard, California, Sep.

- 2009, pp. SMASIS2009-1300.
4. Tao Wu, Chia-Ming Chang, Tien-Kan Chung, and Gregory P. Carman, "The Influence of Magnetic Field and Electric Voltage Bias on Converse Magnetoelectric Effect of Piezo-Fiber/Metglas Composite," in 12th International Meeting on Ferroelectricity and 18th IEEE International Symposium on Applications of Ferroelectrics (IMF-ISAF-2009), Xi'an, China, Aug. 2009, pp. KO-016.
  5. Tao Wu, Chia-Ming Chang, Tien-Kan Chung, and Gregory. P. Carman, "Comparison of Effective Direct and Converse Magnetoelectric Effect in Laminate Composite," INTERMAG09, Sacramento, CA, May, 2009
  6. S. Keller and G. P. Carman, "Homogenized Magneto-Electro-Elastic Properties of Layered Composite Materials.", ASME 2009 Conference on Smart Materials, Adaptive Structures and Intelligent Systems (SMASIS 2009), Oxnard, California, USA September 2009 (Presentation Only)
  7. T. K. Chung, S. Keller, and G. P. Carman, "Magnetoelectric Device Demonstrating Nanoscale Magnetic Domain Control", Proc. SPIE, vol. 7289, pp. 72891S, 2009
  8. T. K. Chung and G. P. Carman, Single-Domain-Transformation/Spin-Structure-Evolution under an Electric Field in a Patterned Magnetoelectric Nanostructure, 2009 IEEE International Magnetism Conference (INTERMAG 2009), Sacramento, California, USA, May 2009 (Accepted, Paper # 608369)
  9. T. K. Chung and G. P. Carman, Magnetoelectric Nanoscale Magnetic-Field Generator, The 15th International Conference on Solid-State Sensors, Actuators, and Microsystems (Transducers'09), Denver, Colorado, USA, June 2009 (Accepted, Paper # 1505)
  10. T. K. Chung, K. P. Mohanchandra, C.M. Chang, and G.P. Carman, "Electrical Control of Magnetization in a Ni/PZT Thin Film", SPIE Smart Structures/NDE Conference 2008, San Diego, California, March 2008 (Presentation Only)

### ***Research Summary***

The UCLA team focused on research to enable a new paradigm of structurally integrable antenna electronics. The concept is to use magneto-electric materials for transmission and reception surfaces (antennae) of broadcast signals. This would not only replace existing conductive materials in antenna systems but could allow phasing control circuitry to be integrated in to the antenna surfaces of an antenna array. Magneto-electric (ME) materials exhibit unique behavior in a number of aspects due to an inherent cross coupling of electric and magnetic fields with the material structure. Due to this cross coupling, ME materials will become electrically polarized in an applied magnetic field and conversely will exhibit magnetization when exposed to an electric field.

Among the interesting phenomena seen in ME materials are strong dependence on propagation direction for the determination of a waves phase velocity and its modes of propagation. The speed modulation capability of the materials may prove useful in the development of electrically small antennas. Further, since the phase velocity can vary

significantly for each propagation mode, polarization rotation commonly occurs in ME materials, providing the potential for polarization modifying devices. Also, due to the anisotropy of the materials, wave polarization can be measured directly with an appropriate electrode configuration as opposed to the need to filter polarization components and then measure intensity. Another significant factor of typical ME materials is that they respond to various field biases. For example, the magnitude of cross-coupling parameters changes under the application of a static electric field. Consequently, ME materials are considered “active materials” which can be tuned on the fly by application of an appropriate bias. This increases the possible applications of the materials and may prove useful for phase matching/altering of electrical signals.

The applications indicated above depend on the ability to produce ME materials with sufficient cross-coupling. Since single phase ME materials generally possess weak cross-coupling parameters their use at this time is impractical. However, strain coupled composite laminates show relatively large magneto-electric coupling effects. In addition to providing sufficient coupling characteristics, laminate construction works well for the thin plate and thin film type applications envisioned for these materials. Therefore, the work conducted under this program focused on evaluating the coupling effects in a wide range of laminate constructions both theoretically and experimentally.

To facilitate use of ME materials in the previously described applications, research efforts at UCLA have focused on three main areas: Analytical Wave Propagation Modeling, Development of the Effective (Homogenized) ME Material Parameters for Laminates, and the Fabrication Testing and Characterization of ME structures (including single domain entities). Below a brief synopsis of each area is provided.

### ***Analytical Wave Propagation Modeling:***

#### **Wave propagation in extended media**

Our work has focused on electro-magnetic behavior of single-phase homogenized structures with direct cross-coupling of both E and H fields. The materials analyzed are assumed to be lossless although the formulations used for calculations work for general frequency dependent materials. Utilizing the source free Maxwell's Equations

$$\vec{\nabla} \times \vec{E} = -\dot{\vec{B}} \quad \vec{\nabla} \times \vec{H} = \dot{\vec{D}} \quad \Rightarrow \quad \vec{k} \times \vec{E} = \omega \vec{B} \quad \vec{k} \times \vec{H} = -\omega \vec{D}$$

$$\vec{\nabla} \cdot \vec{B} = 0 \quad \vec{\nabla} \cdot \vec{D} = 0 \quad \vec{k} \cdot \vec{B} = 0 \quad \vec{k} \cdot \vec{D} = 0$$

and lossless linear magneto-electric constitutive relations for electric flux density D and magnetic flux density B,

$$\vec{E} = \bar{\kappa} \vec{D} + \bar{\chi} \vec{B} \quad \text{and,} \quad \vec{H} = \bar{\chi}^T \vec{D} + \bar{\nu} \vec{B}$$

where  $\chi$  represents the second order magneto-electric tensor. Using these equations we developed a generalized wave equation that allows for the analytic solution of plane wave propagation modes.

$$\begin{aligned} & \left[ \left( \frac{\omega}{k} \begin{bmatrix} 0 & -1 \\ 1 & 0 \end{bmatrix} - \hat{\gamma} \right) \hat{\kappa}^{-1} \left( \frac{\omega}{k} \begin{bmatrix} 0 & 1 \\ -1 & 0 \end{bmatrix} - \hat{\chi} \right) - \hat{v} \right] \begin{bmatrix} B_1 \\ B_2 \end{bmatrix} = \begin{bmatrix} 0 \\ 0 \end{bmatrix} \\ & \begin{bmatrix} D_1 \\ D_2 \end{bmatrix} = \hat{\kappa}^{-1} \left[ \frac{\omega}{\kappa} \begin{bmatrix} 0 & 1 \\ -1 & 0 \end{bmatrix} - \hat{\chi} \right] \begin{bmatrix} B_1 \\ B_2 \end{bmatrix} \end{aligned}$$

By reducing the three dimensional problem to two dimensions, the problem is made more tractable and the dispersion relation can be obtained in an analytic form. Once values are determined for  $\frac{\omega}{k}$  the system of equations can be solved to determine the modes for B. The B solutions then determine D from the second system of equations.

The dispersion relation is a 4<sup>th</sup> order polynomial in the inverse of the index of refraction. For special cases, i.e. when the material cross-coupling goes to zero, the dispersion relation can be reduced to an effective 2<sup>nd</sup> order equation which is representative of conventional material systems. However, for general ME material, four distinct roots, i.e. wave phase velocities, can exist for a given propagation vector. Generally this translates to two modes of propagation in the forward direction and two different modes of propagation in the opposite direction, which is quite different from the behavior of conventional materials. That is the material is non-reciprocal and forward velocity propagation speeds are distinctly different from backward velocity propagation speeds.

For the case of a “homogeneous” magnetoelectric material, we have examined the phase velocity profiles for the archetypal cases. Figure 1 shows plots of phase velocity with angle of propagation through the material indicating asymmetry between forward and backward travel, a characteristic of the non-reciprocal ME materials. For each propagation direction there are two modes of propagation found, as exhibited by the two phase velocity surfaces shown. For a general propagation vector it can be seen that the phase velocity of each mode is different. This velocity difference causes a polarization rotation of the wave as it propagates through an ME material. The forward and reverse rotations are different in general as can be seen from the asymmetry in each plot. At some corresponding points on the surfaces (i.e. at the same angles), we see the velocities are the same. At these directions the waves propagate without rotation and the incoming mode is unaltered.

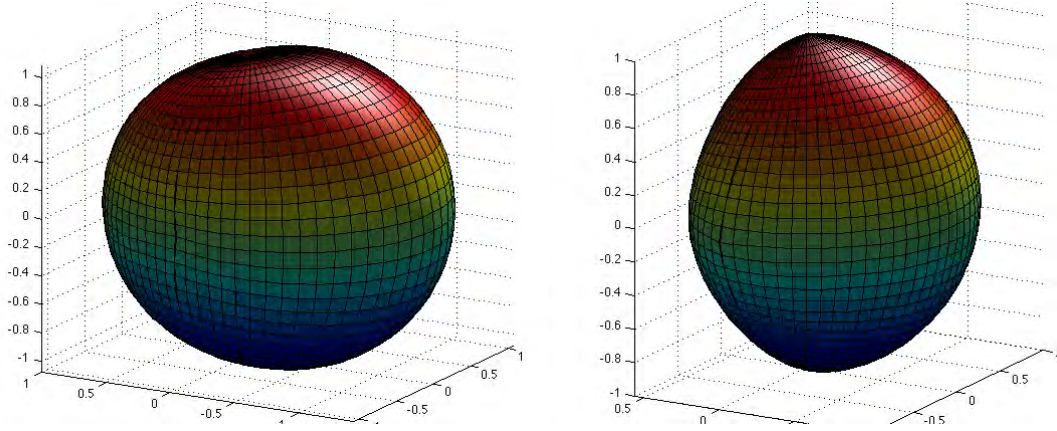


Figure 1 Phase velocity profiles as a function of wavevector direction for a material with  $\chi_{13}$  coupling. Each surface represents the phase velocity of one propagation mode.

The previous plot showed a basic illustration of the non-reciprocal nature of magnetoelectric laminates. However, more interesting situations have been observed in the parameter space, such as zero velocity modes like the one shown in figure 2. For large cross-coupling parameters, the phase velocity in a certain direction will approach zero. Thermodynamic limits prevent the cross-coupling from actually achieving the zero point; however, it should be theoretically possible to get infinitesimally close. For real materials it is uncertain how close but large velocity ratios should be realistic.

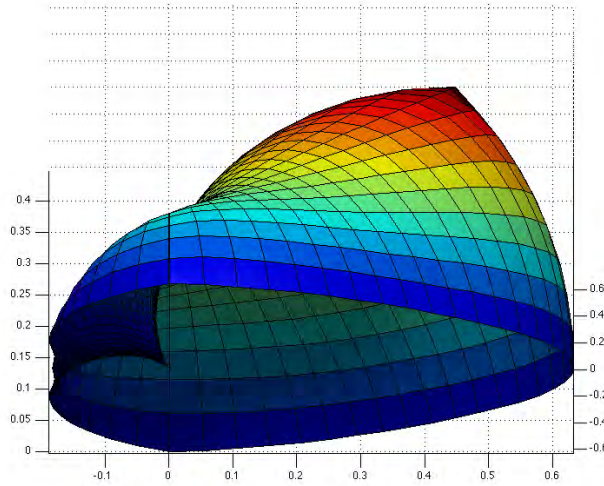


Figure 2 Phase velocity profile for a material with  $\chi_{12}$  and  $\chi_{13}$  coupling. The point structure shown in the plot indicates a region in which the phase velocity decreases to zero. The zero velocity point corresponds to a theoretical limit but arbitrarily small velocities are theoretically possible.

Our work shows that phase shifting and polarization rotation applications are possible. The separation of polarization components is more direct with magneto-electric materials than with “conventional” materials since field polarization components may be separated by using material coupling rather than filtering a specific polarization and then measuring the component amplitude.

### Interface behavior of ME materials

The previous work was extended to examine the behavior of waves at the interface of two ME materials or the interface between an ME and a conventional material. While Snell’s law still holds for ME materials, the fact that the wave vector is dependent on transmission angles through the material creates additional interesting behavior not normally observed. The propagating EM wave is split on reflection (ME–ME interface only) and transmission, although for some materials parameters there are propagation directions which do not result in birefringent behavior on transmission (See Figure 3). Our current work has been to develop a model that calculates the wave vectors, reflection/transmission coefficients, and field components of an incident plane wave onto an ME interface with an emphasis on identifying interesting “propagation” modes that either rapidly disperse wave energy or allow forward propagation without significant modification.

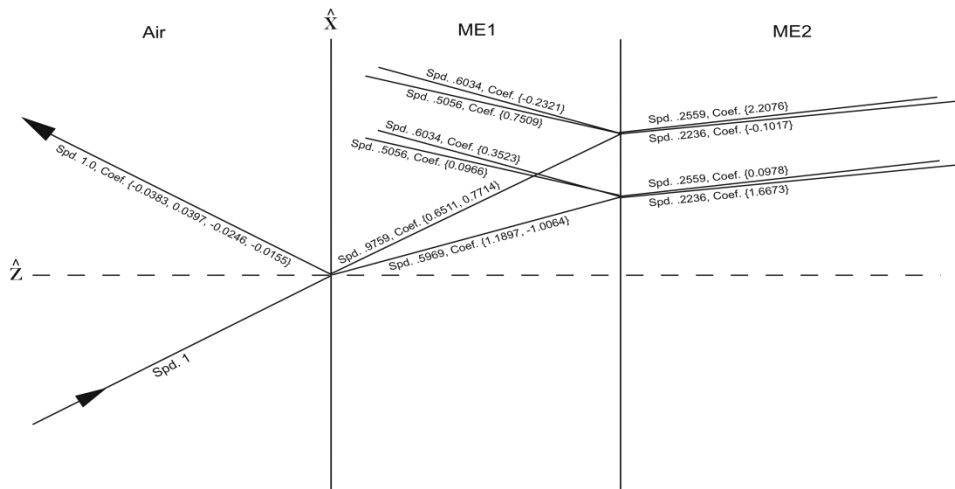


Figure 3 Typical Transmission/Reflection characteristic at ME interface.

### Wave behavior in constituent phases of ME laminates

To better understand the direct elastic interaction effects of the proposed ME laminates the wave equation and techniques used above were applied to the piezoelectric and

magnetoelectric phases individually. Using the mechanical equilibrium equation and small strain approximation in spatial and time frequency domain:

$$\underline{\underline{\varepsilon}} = \frac{k^2}{\rho\omega^2} \underline{\underline{N}}^T \underline{\underline{N}} \underline{\underline{\sigma}},$$

where epsilon is the strain, sigma is the stress (both in Voigt notation), k is the magnitude of the wavevector, omega the angular frequency and N relates to the direction cosines of the unit vector in the direction of wave propagation,

$$\underline{\underline{N}} = \begin{bmatrix} n_1 & 0 & 0 & n_3 & 0 & n_2 \\ 0 & n_2 & 0 & 0 & n_3 & n_1 \\ 0 & 0 & n_3 & n_1 & n_2 & 0 \end{bmatrix} \text{ with the } n_i \text{ the direction cosines of the wavevector to}$$

coordinate axis. Using the piezoelectric constitutive equations as an example,

$\underline{\underline{\varepsilon}} = \underline{\underline{s}} \underline{\underline{\sigma}} + \underline{\underline{d}}^T \underline{\underline{E}}$ ,  $\underline{\underline{D}} = \underline{\underline{d}} \underline{\underline{\sigma}} + \underline{\underline{\varepsilon}} \underline{\underline{E}}$ , and  $\underline{\underline{B}} = \underline{\underline{\mu}} \underline{\underline{H}}$ , we combine the equilibrium equation above with the first constitutive equation to obtain:

$$\left( \frac{k^2}{\rho\omega^2} \underline{\underline{N}}^T \underline{\underline{N}} - \underline{\underline{s}} \right) \underline{\underline{\sigma}} = \underline{\underline{d}}^T \underline{\underline{E}}.$$

The matrix on the left hand side is invertible exactly when the ratio of  $\frac{k}{\omega}$  is not the speed of a mechanical wave, which we would have if the d matrix was zero. This can now be used to eliminate  $\sigma$  from the other constitutive equation to form:

$$\underline{\underline{D}} = \underline{\underline{\tilde{e}}} \underline{\underline{E}} \text{ with } \underline{\underline{\tilde{e}}} = \left[ \underline{\underline{e}} + \underline{\underline{d}} \left( \frac{k^2}{\rho\omega^2} \underline{\underline{N}}^T \underline{\underline{N}} - \underline{\underline{s}} \right)^{-1} \underline{\underline{d}}^T \right].$$

This effectively converts the electromagnetic-mechanical problem to a strictly electromagnetic problem which can be handled as a normal eigenvalue problem. The piezomagnetic case can be handled directly by duality, switching the roles of  $\underline{\underline{\mu}}$  and  $\underline{\underline{e}}$ , etc.

Once the field quantities are solved in their respective piezoelectric and piezomagnetic materials, boundary conditions can be applied at an interface to solve for any propagating wave modes. Solutions for propagating waves are analytic or at least soluble to arbitrary precision and can also be used to test the homogenization models for ME laminates proposed below.

### *Development of effective laminate properties:*

A survey of available ferroelectric and ferromagnetic materials was performed to identify optimal combinations to maximize the magnetoelectric coupling. The primary purpose of the survey was to identify ferroelectric material with large electromechanical coupling and ferromagnetic material with large magnetomechanical coupling as well as the permittivity and permeability of the respective materials. Following this survey, an analytic method was developed to determine the effective material properties of magnetoelectric laminate structures.

The constitutive equations of any given layer can be expressed in the following form. Where  $\gamma$  is strain,  $D$  is electric flux,  $B$  is magnetic flux,  $\sigma$  is stress,  $E$  is electric field,  $H$  is magnetic field,  $S$  is the compliance matrix,  $d$  is the piezoelectric tensor,  $q$  is the piezomagnetic tensor,  $\epsilon$  is permittivity,  $\mu$  is permeability, and  $m$  is the magnetoelectric tensor.

$$\begin{aligned}\{\gamma\} &= [S]\{\sigma\} + [d]^T \{E\} + [q]^T \{H\} \\ \{D\} &= [d]\{\sigma\} + [\epsilon]\{E\} + [m]\{H\} \\ \{B\} &= [q]\{\sigma\} + [m]\{E\} + [\mu]\{H\}\end{aligned}$$

Rearranging the equations allows us to relate stress, electric flux, and magnetic flux to strain, electric field and magnetic field in each layer.

$$\begin{Bmatrix} \{\sigma\} \\ \{D\} \\ \{B\} \end{Bmatrix} = \begin{bmatrix} [Q] & [Q][d]^T & [Q][q]^T \\ [d][Q] & [\epsilon] - [d][Q][d]^T & [m] - [d][Q][q]^T \\ [q][Q] & [m] - [q][Q][d]^T & [\mu] - [q][Q][q]^T \end{bmatrix} \begin{Bmatrix} \{\gamma\} \\ \{E\} \\ \{H\} \end{Bmatrix}$$

By integrating through the thickness of the layered structure ( $z$ ) an expression is found to relate mid-plane strain ( $\gamma^0$ ), curvature ( $\kappa$ ), electric field and magnetic field of the laminate to the resultant forces ( $N$ ), resultant moments ( $M$ ), electric flux and magnetic flux.

$$\begin{Bmatrix} \{\gamma^0\} \\ \{\kappa\} \\ \{E\} \\ \{H\} \end{Bmatrix} = \begin{bmatrix} \sum [Q]_i t_i & \sum [Q]_i (z_i^2 - z_{i-1}^2) & \sum [Q]_i [d]_i^T t_i & \sum [Q]_i [q]_i^T t_i \\ \sum [Q]_i (z_i^2 - z_{i-1}^2) & \sum [Q]_i (z_i^3 - z_{i-1}^3) & \sum [Q]_i [d]_i^T (z_i^2 - z_{i-1}^2) & \sum [Q]_i [q]_i^T (z_i^2 - z_{i-1}^2) \\ \sum [d]_i [Q]_i t_i & \sum [d]_i [Q]_i (z_i^2 - z_{i-1}^2) & \sum ([\epsilon]_i - [d]_i [Q]_i [d]_i^T) t_i & \sum ([m]_i - [d]_i [Q]_i [q]_i^T) t_i \\ \sum [q]_i [Q]_i t_i & \sum [q]_i [Q]_i (z_i^2 - z_{i-1}^2) & \sum ([m]_i - [q]_i [Q]_i [d]_i^T) t_i & \sum ([\mu]_i - [q]_i [Q]_i [q]_i^T) t_i \end{bmatrix}^{-1} \begin{Bmatrix} \{N\} \\ \{M\} \\ \{D^{eff}\} \\ \{B^{eff}\} \end{Bmatrix}$$

The matrix in the above relation represents the effective material properties for the laminate as a whole. These effective laminate properties are used in Maxwell's Equations (previous sections) to determine EM wave propagation in the laminate.

There is a problem with the above formulation in that it essentially ignores out of plane strain components which may be important, particularly for wave propagation applications. UCLA is working on an alternative formulation which may better approximate the homogenized material parameters by taking into account the out of plane interactions that arise from piezoelectric and piezomagnetic coupling.

If we take the z axis as the out of plane for a laminate ME material we find that half of the field components are continuous across all layers of the composite as required by boundary conditions of the respective mechanical or electromagnetic governing equations. For the current situation this implies  $(\gamma_1, \gamma_2, \sigma_3, \sigma_4, \sigma_5, \gamma_6, E_1, E_2, D_3, H_1, H_2, B_3)$  are continuous quantities across all interfaces while  $(\sigma_1, \sigma_2, \gamma_3, \gamma_4, \gamma_5, \sigma_6, D_1, D_2, E_3, B_1, B_2, H_3)$  generally change discontinuously across the interfaces.

For linear materials it is straightforward to rearrange the  $\left\{ \begin{matrix} \sigma & D & B \end{matrix} \right\}^T = [S] \left\{ \begin{matrix} \gamma & E & B \end{matrix} \right\}^T$  constitutive form shown above to a hybrid form such that :

$$\left\{ \sigma_1, \sigma_2, \gamma_3, \gamma_4, \gamma_5, \sigma_6, D_1, D_2, E_3, B_1, B_2, H_3 \right\}^T = [M] \left\{ \gamma_1, \gamma_2, \sigma_3, \sigma_4, \sigma_5, \gamma_6, E_1, E_2, D_3, H_1, H_2, B_3 \right\}^T$$

where  $[M]$  represents the rearranged constitutive parameter matrix. For a layered material we have constitutive equations of the above form for each layer where  $[M]$  contains the material specific dependencies for each layer. If we denote the above equation for the nth layer as

$$\underline{Y}^{(n)} = [M]^{(n)} \underline{X}^{(n)}$$

where

$$\underline{Y}^{(n)} \equiv \left\{ \sigma_1, \sigma_2, \gamma_3, \gamma_4, \gamma_5, \sigma_6, D_1, D_2, E_3, B_1, B_2, H_3 \right\}^T \text{ for the nth layer and}$$

$$\underline{X}^{(n)} = \left\{ \gamma_1, \gamma_2, \sigma_3, \sigma_4, \sigma_5, \gamma_6, E_1, E_2, D_3, H_1, H_2, B_3 \right\}^T$$

then the integral through the thickness of the material becomes

$$\int_{h^-}^{h^+} dz \underline{Y}^{(n)} = \int_{h^-}^{h^+} dz [M]^{(n)} \underline{X}^{(n)}.$$

Assuming each layer is homogeneous, dividing by the thickness of the composite  $t = h^+ - h^-$  gives

$$\langle \underline{Y} \rangle = \frac{1}{t} \sum_{n=0}^N [M]^{(n)} \int_{z^n}^{z^{n+1}} dz \underline{X}^{(n)}.$$

The angle brackets indicate the average in  $z$  of the field quantities contained in  $\underline{Y}$ . We note that for a 1<sup>st</sup> order estimate where each field quantity is constant for each layer, the above simplifies to

$$\langle \underline{Y} \rangle = \left( \sum_{n=0}^N v_f^{(n)} [M]^{(n)} \right) \underline{X}, \quad v_f^{(n)} = \text{volume fraction of the } n\text{th layer}.$$

Since the field variables on the right side are continuous they must be constant throughout the laminate thickness to first order. If we then rearrange the resulting matrix equation into  $\left\{ \begin{matrix} \sigma & D & B \end{matrix} \right\}^T = [\tilde{S}] \left\{ \begin{matrix} \gamma & E & B \end{matrix} \right\}^T$  format,  $[\tilde{S}]$  being a fairly involved mixture of constitutive parameters from each layer, we reduce to the cross-coupling estimations seen commonly in the literature for bi- or tri-layer structures when  $N=2$  or  $3$ . The form suggested above provides a convenient manner for calculating the cross-coupling for multi-layer systems compared with the approach conventionally employed.

Additionally, for higher order estimates, the field quantities contained on the right side of the integral equation can be estimated by series expansions compatible with the continuity of the underlying fields. In particular, we should be able to express  $\underline{X} = \underline{X}(K_1(x,y), K_2(x,y), z)$  where  $K_1$  and  $K_2$  represent the local curvatures at a reference plane in the laminate and express the constitutive relations for the plate as a function of the resultant stresses, moments, curvature, and averaged field quantities of the composite.

### ***Fabrication, Characterization and Testing of ME materials***

#### **Comparison of Effective Direct and Converse Magneto-electric Effects in Laminate Composites**

There is a good deal of confusion in the general literature describing direct and converse magneto-electric effects. This stems largely from a lack of standardization in what physical quantities are reported and the specific methods of measurement (ie – whether the entire laminate response is reported or only the response in say the piezomagnetic phase). Theoretically from thermodynamic considerations one should expect that the direct magneto-electric effect (DME) defined as  $\frac{\partial D}{\partial H}$  and the converse magneto-electric

effect (CME) defined by  $\frac{\partial B}{\partial E}$  should be equivalent. An experiment was conducted on a tri-layer PZT-TerfenolD-PZT plate to compare actual DME and CME coefficients with expected results from an analytic model based on the constituent phases indicated above.

Our analysis on the tri-layer structure predicts a CME coefficient,  $\alpha_C$ , and a DME coefficient,  $\alpha_C$ , as follows;

$$\alpha_D = \left| \frac{\partial D_3}{\partial H_1} \right| = \left| \frac{d_{31,p} d_{11,m}}{s_{11}^E t_m + 2s_{11}^H t_p} \right| \cdot t_m \text{ and } \alpha_C = \left| \frac{\partial B_1}{\partial E_3} \right| = \left| \frac{d_{31,p} d_{11,m}}{s_{11}^E t_m + 2s_{11}^H t_p} \right| \cdot 2t_p.$$

$D_3$  and  $E_3$  are the electric displacement and electric field along the piezoelectric thickness direction, respectively.  $B_1$  and  $H_1$  are magnetic flux density and magnetic field strength along the length direction, respectively.  $s_{11}^E$  and  $s_{11}^H$  are the compliance coefficients at constant electric field and constant magnetic field, respectively.  $d_{31,p}$  and  $d_{11,p}$  are the piezoelectric and piezomagnetic coefficients, respectively.

To evaluate the theoretical analysis, a trilayer magnetoelectric laminate was fabricated. The laminate consisted of a single layer of (112)-oriented  $\text{Tb}_{0.3}\text{Dy}_{0.7}\text{Fe}_{1.92}$  (Terfenol-D) magnetostrictive alloy plate (i.e., oriented along the 1-direction) between two layers of oppositely poled  $\text{Pb}(\text{Zr}_x\text{Ti}_{1-x})\text{O}_3$  (PZT-5H) piezoelectric plates. The (112)-oriented Terfenol-D plate was obtained from ETREMA Inc. (Ames, IA), and had a dimension of  $24.45 \times 6.7 \times 1.6 \text{ mm}^3$ . The piezomagnetic coefficient,  $d_{11,m}$ , of the (112)-oriented Terfenol-D plate was measured to be 5–7 nm/A under optimum magnetic bias field and the elastic compliance coefficient was 30–40  $\text{pm}^2/\text{N}$ . The PZT-5H plates were obtained from Piezo Systems, Inc. (Cambridge, MA), and had a dimension of  $24.5 \times 6.7 \times 0.267 \text{ mm}^3$ . The piezoelectric coefficient,  $d_{31,p}$ , and elastic compliance coefficient,  $s_{11}^E$ , of the PZT-5H plate are -320 pC/N and 16.5  $\text{pm}^2/\text{N}$ , respectively. The Terfenol-D plate was sandwiched between PZT-5H plates with a 76  $\mu\text{m}$  thick silver conductive film (CF3350, Emerson & Cuming). The laminate was cured at 125 C for 2 h with mechanical load to enhance the bonding.

The DME effect of the laminate sample was characterized by measuring magnetic-field-induced electric polarization (MIE). An electromagnet was employed to provide a DC magnetic field bias ranging from 0 to 3000 Oe. A small custom made solenoid coil applies a small AC magnetic field (0.1 to 2 Oe). The induced out of plane ME voltage, through the thickness of the PZT layers, was measured. The CME effect was characterized by measuring electric-field-induced magnetization (EIM). A sine wave reference source coupled with a voltage amplifier applied an AC electric voltage, from 1 to 100 V, across the PZT layers. The induced magnetization in the Terfenol-D layer is calculated from the *emf* voltage induced in a search coil, which was measured with a lock-in amplifier. It is important to note that the search coil was wrapped around the entire laminate and not just the magnetostrictive layer. This approach is typically used in reporting CME response.

We found the effective DME and CME coefficients to be of the same order of magnitude, but were significantly different (see Figure 4). The measured values were also significantly smaller than predicted by analysis.

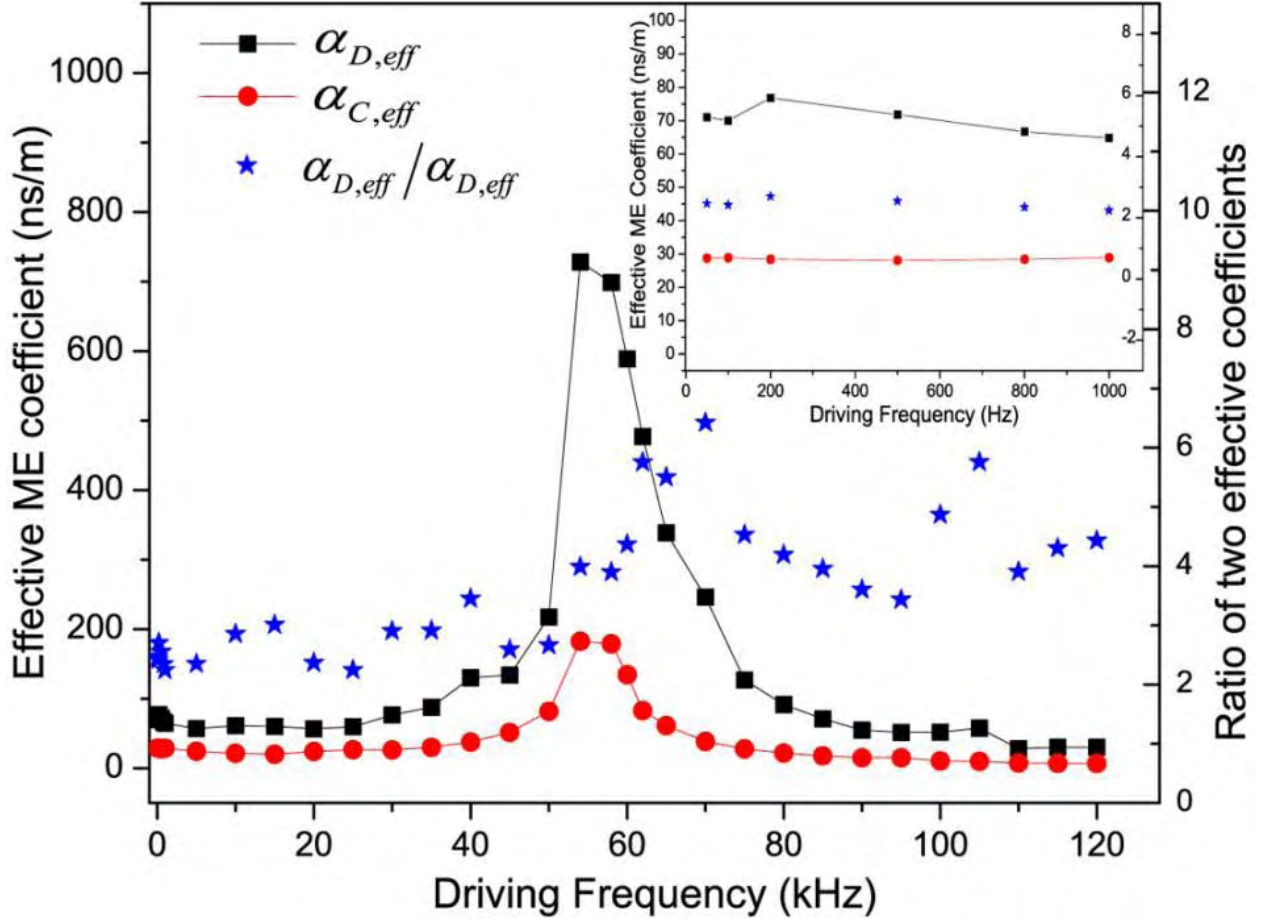


Figure 4 Effective DME and CME coefficients and the ratio of two effective coefficients as a function of excitation frequency. The inset shows details of low-frequency data.

The experimental results suggest that closer scrutiny of these results and other data in the literature is needed to better report measurement values that can be compared.

### Influence of electric voltage bias on converse magnetoelectric coefficient in piezofiber/Metglas bilayer laminate composites

Magneto-electrics are active materials whose behavior is strongly influenced by bias fields applied to the materials under test. For example magnetic fields, electric fields and stress/strain fields all can be used to control/adjust ME material properties. However results in the literature have only focused on the influence of magnetic fields and there is a virtual absence of experimental data on the influence of either electric fields or stress/strain bias fields. Therefore, experiments were conducted on a piezofiber/Metglas bilayer (PFM) composite subjected to both a dc electric voltage bias and subsequently a mechanical bias.

The tests done here focused on evaluating the optimum electric bias fields on a PFM fabricated at UCLA. The piezofiber layer is a macrofiber composite (MFC) from Smart Material Corp., with dimensions of 28x7x0.3 mm<sup>3</sup>. The piezoelectric constant  $d_{33}$  value is

approximately 0.75 ppm/V and the Young's modulus is 30 GPa in the fiber direction. The Metglas layer is a 2826MB type iron nickel based alloy (Metglas Inc.), with dimensions of 28x7x0.025 mm<sup>3</sup>. The PFM layers are bonded together with Loctite® Epoxy. The measured thickness of the entire sample is approximately 0.375 mm.

To characterize the CME response, a dc magnetic field bias  $H_{bias}$ , up to 40 Oe, is applied along the longitudinal direction of the sample with a Helmholtz coil. A separate dc electric voltage bias  $V_{bias}$ , -300 to 700 V, is applied with a dc source coupled with a voltage amplifier. An ac electric voltage  $V_{ac}$ , 0.1–60 V<sub>rms</sub>, is applied using a sine wave generator coupled to the voltage amplifier. The induced magnetic field is measured with a coil wrapped around the sample.

Previous studies on similar materials show that a dc magnetic field bias can be used to maximize the CME coefficient. Our experimental data also show that the optimum dc magnetic field bias is a function of applied dc electric voltage (see Figure 5). Furthermore, an optimum dc electric voltage bias exists which maximizes the converse magnetoelectric coefficient.

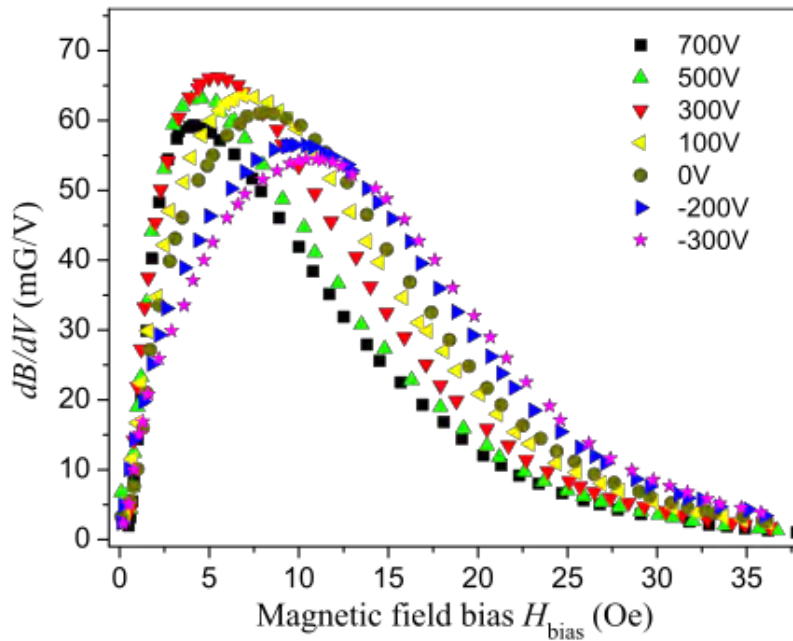


Figure 5 Measured magnetic flux density  $B$  as a function of magnetic field bias  $H_{bias}$  with different electric voltage biases.

Our data indicates that the CME effect is strongly dependent on dc electric voltage bias with the value changing by up to 70% over the dc electric voltage bias values studied.

### Influence of mechanical load bias on CME effect in ME laminates

UCLA's previous studies have focused primarily on the bias effects of electric and magnetic fields on the performance of ME materials. Of equal or greater importance is

understanding the influence of mechanical loading on ME laminates. In real world settings, ME laminates will undergo mechanical biasing both from intended application of loads as well as in response to environmental factors. Consequently, data is needed to characterize ME materials under diverse loading conditions.

Here a piezofiber/Metglas (PFM) ME laminate has been integrated into a graphite epoxy composite (GEC) to study the CME effect. Experimental data on a PFM/GEC driven with an ac electric voltage subjected to both a dc magnetic field bias and a dc mechanical load bias are presented. Results of these tests indicate that both the mechanical load and the dc magnetic field strongly influence the CME response. Furthermore, an optimum mechanical load exists to maximize the CME coefficient. These results reveal that the CME coefficient can be further increased with a proper mechanical load bias. Therefore, the selection of an appropriate mechanical preload as well as dc magnetic bias will maximize the CME response and sensitivity in ME laminates as well as integrated structural systems.

A PFM/GEC laminate composite was fabricated for the tests performed. The piezofiber layer is a macrofiber composite (Smart Material Corp.) with dimensions of  $28 \times 7 \times 0.3 \text{ mm}^3$ . The piezoelectric constant  $d_{33}$  value is approximately 0.75 ppm/V, and Young's modulus is 28 GPa in the fiber direction. The Metglas layer is a 2826MB type iron nickel based alloy (Metglas Inc.), with dimensions of  $28 \times 7 \times 0.025 \text{ mm}^3$ . The Young's modulus of Metglas is 110 GPa. The graphite epoxy AS4/ 3501-6 composite (GEC) is a  $[(0^\circ / \pm 45^\circ / 90^\circ)_s]_3$  quasi-isotropic layup with an effective in-plane Young's modulus of 50 GPa. The GEC dimensions are  $160 \times 49 \times 7 \text{ mm}^3$ . The PFM ME laminate is attached to the center of one side of the GEC using Loctite® epoxy. For analytical modeling, the in-plane Poisson's ratio for the MFC is 0.36 and for GEC layer is 0.3.

The PFM/GEC composite sample was mounted in a load frame, and both tensile and compressive static loads applied. The PFM bilayer is approximately 40 cm away from the gripped region of the GEC. Two strain gauges are attached on both sides of the PFM/GEC sample. To characterize the CME response, an ac electric driving voltage  $V_{ac}$  is applied on the MFC layer using a sine wave source fed to a voltage amplifier. A dc magnetic field bias, up to 40 Oe, is applied along the longitudinal direction of the sample using a Helmholtz coil. The induced magnetization in the PFM/GEC sample is measured using a 120-turn search coil wrapped around the entire PFM/GEC composite.

A plot of obtained magnetization data at seven different mechanical loads/strain values is shown in Figure 6. Our experimental results indicate that the mechanical load bias strongly influences the value of the optimum  $H_{bias}$ . A proper preload should be selected to optimize the CME response and sensitivity for magnetic field detection in both ME laminates as well as integrated structural systems.

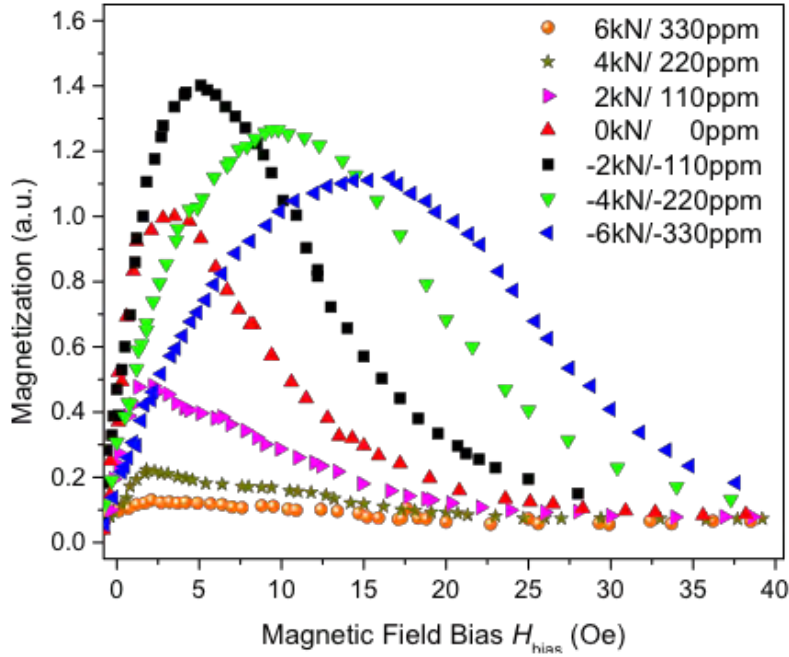


Figure 6 Normalized electric-field-induced magnetization (CME effect) as a function of dc magnetic field bias under different mechanical loads/strains.

### Nanostructure Fabrication

To better understand the response of magnetoelectric in the small scale and thin film structure, we fabricated an ME thin film material. As previously reported the deposition of both Ni on PZT thin film were on silicon substrates with the Ni film is approximately 100 nm thick and the PZT film is about 1.28 micron. A number of tests were conducted on the structure below we describe the magnetic force microscope MFM results when a voltage is applied to the PZT. During this test the surface of the ME thin film was monitored with an MFM and a typical stripe domain pattern on the Ni phase of the bilayer film appeared without an applied voltage. After application of 10V to the PZT phase of the structure MFM imaging reveals significant differences in the stripe domain patterns (see Figure 7 below). These images confirm significant ME effects in nano-structured materials using strain coupled piezoelectric and piezomagnetic phases. When an electric field is applied to the PZT-film, mechanical coupling between the PZT-film and the Ni-film induces strain in the Ni. The magnetostrictive properties of the Ni then induce changes in the observed domain pattern. The

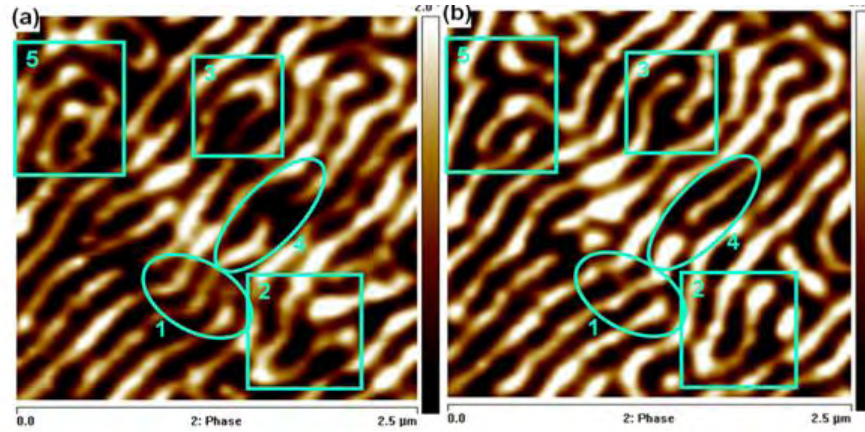


Figure 7. Magneto-electric effect in a Ni/PZT thin film material. Image at left shows sample with no voltage applied. The image at right is the same sample with 10V (approx. 1MV/m field). Changes in stripe domain pattern is evident by comparison of labeled regions.

Next we fabricated a magnetoelectric nanostructure and demonstrated that electric control of the magnetic spin structure is possible. An illustration of the magnetoelectric nanostructure, a layered Ni nanobar on a PZT thin film structure, is shown in Figure 8.

The MFM images indicate substantial change in the magnetization of the nanobar with the application of voltage to the piezoelectric phase of the ME structure. The length and width of the Ni nanobar is approximately 380 nm x 150 nm. As in the previous structure, strain coupling between phases produces the changes in magnetization seen in the Ni.

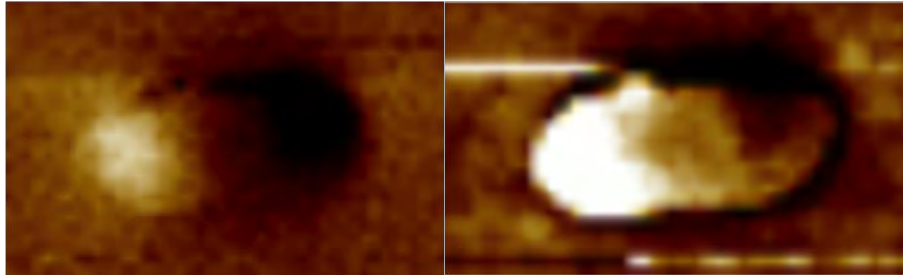


Figure 8. Illustration of change in magnetization structure seen with MFM. The image on the left is with zero volts and the image on the right shows 1.5V applied to the PZT phase of the ME nanostructure.

## Prof. James' Group Summary

**People:** Amartya Banerjee (Graduate Student). Partial support of Shankar Krishnan.

### Journal Papers Published/Submitted

1. Liping Liu, Richard James and Perry Leo, "*New extremal inclusions and their applications to two-phase composites.*" Archive for Rational Mechanics and Analysis, in press (2009).
2. Zhiyong Zhang, Richard D. James and Stefan Muller, "*Energy barriers and hysteresis in martensitic phase transformations*", Acta Materialia (Overview # 147) 57 4332–4352 (2009)
3. Kaushik Dayal, Ryan Elliott and Richard D. James, "*Objective formulas*", preprint.
4. Rémi Delville, Dominique Schryvers, Jan Van Humbeeck, Sakthivel Kasinathan, Zhiyong Zhang and Richard D. James, "*A transmission electron microscopy study of phase compatibility in low hysteresis shape memory alloys*", 90, 177–195 (2010)
5. D.B. Zhang, R.D. James, and T. Dumitrica, *Electromechanical characterization of carbon nanotubes in torsion via symmetry-adapted tight-binding objective molecular dynamics*, Physical Review B 80, 115418 (2009)
6. Kaushik Dayal and Richard D. James, *Nonequilibrium molecular dynamics for bulk materials and nanostructures*, Journal of the Mechanics and Physics of Solids 58, 145 (2010)
7. Nikiforov, D.-B. Zhang, R. D. James, and T. Dumitrică, *Wavelike Rippling in Multiwalled Carbon Nanotubes under Pure Bending*, Appl. Phys. Lett. 96, 123107 (2010)
8. D.B. Zhang, R.D. James, and T. Dumitrica, *Dislocation Onset and Nearly Axial Glide in Carbon Nanotubes under Torsion*, Journal of Chemical Physics [Communication] 130, 071101 (2009)
9. Vijay Srivastava, Xian Chen, and Richard D. James, *Hysteresis and unusual magnetic properties in the singular Heusler alloy Ni<sub>45</sub>Co<sub>5</sub>Mn<sub>40</sub>Sn<sub>10</sub>*, Appl. Physics Letters, accepted.

### Theses:

- 1) Amartya Sankar Banerjee, A Density Functional Theory for Objective Structures and its Applications (M.S., in preparation), August 2010.
- 2) Krishnan Shankar Narayan, Stability of the Single Domain State in Magnetic Nanowires (M.S. Thesis), December 2008

Our tasks for the GameChanger project were in two areas, one short term that concerns the use of magnetic nanowires in antenna systems and one long term that seeks to develop general methods to calculate the properties of magnetic and ferroelectric properties of nanostructures from first principles. The former concerns the use of nanowires to increase  $\epsilon_r$  and  $\mu_r$  proportionately to slow the wave while matching impedance. The key point about the use of nanowires is that they can exist in the single domain state, without domain walls. The

presence of domain walls has previously been linked to loss in ferromagnetic elements. Thus, it is critical to make predictions of the critical radius of a nanowire at which the single domain state loses stability, and especially to understand how this depends on the material constants. This will guide the selection of the best kind of magnetic material for this possible application. The second thrust of our research is a long term effort to develop a first principles method for the systematic calculation of properties of nanostructures, and to use this to seek new nanostructures with desirable properties for antennas.

On the first area of research, we have developed general methods for calculating the breakdown of the single domain state in nanowires. It is based on a mathematical analysis of the full energy of micromagnetics including exchange, anisotropy, demagnetization, magnetostrictive and applied field contributions to the energy. For this we have given upper and lower bounds, and we have also developed a code for direct calculation of the eigenfunction at breakdown.

Typical calculated values are shown in Figure 1. Typical diameters for breakdown of the single domain state in nanowires are 25-150 nm with little dependence on aspect ratio for wire-like structures.

Alloy	Anisotropy constant $K1 \times 10^3$ erg/cc	Saturation magnetization $M_s$ emu	Exchange constant C	Aspect Ratio	lower bnd $R_{lb}$ $10^{-9}$ m	upper bound $R_{ub}$ $10^{-9}$ m
Fe	420	1700	$1.8 \times 10^{-6}$	q=50	14.6	29.2
				q=100	14.9	29.8
Fe+3%Si	350	1580	$1.8 \times 10^{-6}$	q=50	15.9	31.8
				q=100	16.8	33.6
Fe+3%Si	225	1420	$1.8 \times 10^{-6}$	q=50	19.6	39.2
				q=100	20.9	41.8
50%Fe- 10%Co- 40%Ni	61	900	$1.8 \times 10^{-6}$	q=50	37.9	75.9
				q=100	39.2	78.4
70%Fe- 30% Co	102	1900	$1.8 \times 10^{-6}$	q=50	29.5	58.9
				q=100	30.2	60.4

Fig. 1 Rigorous upper and lower bounds for radius at breakdown of the single domain state.

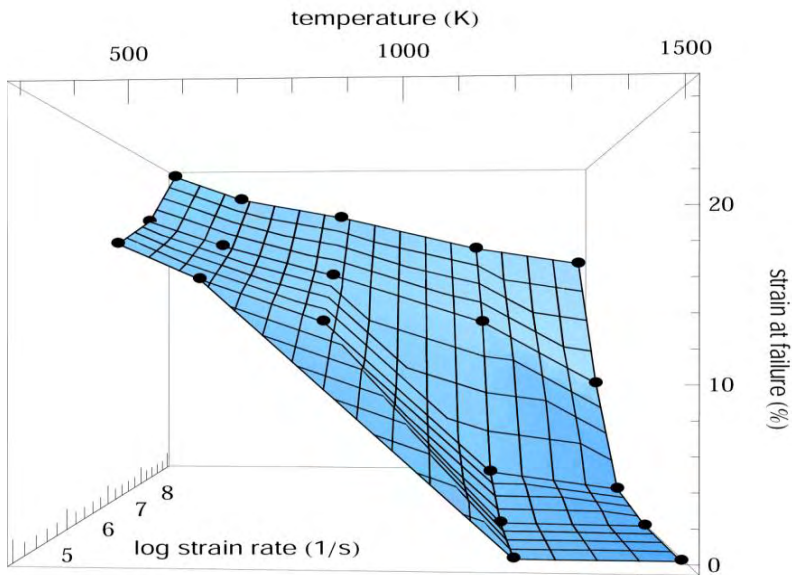
We noticed that many nanostructures are “objective structures”, that is, they are composed of molecules such that corresponding atoms in each molecule see the same environment up to orthogonal transformation. For example, a single-walled carbon nanotube (of any chirality) is such a structure with one atom per molecule.

During the past year we have made major progress on these long term issues. Our main advances have been:

1. Major progress on a DFT strategy for objective structures, including advances of the basic theory. Our methods have concentrated on the development of an analog of the Kohn-Sham iterations. For objective structures such as buckyballs and rings of atoms, we have developed a real-space finite difference algorithm that computes the electronic structure while taking into account the symmetry that underlies these structures. For objective structures such as helical rods and nanotubes, we have decided not to design a real space strategy, but rather to develop a method that more precisely uses the isometry groups associated with these objective structures through a spectral method. We have developed an analog of the Bloch theorem for objective structures for some of the groups describing objective structures. We have also developed an efficient method for generating fundamental domains and discretizing them as well as a pseudo-spectral code that has been used for producing some results. A description of this work will be given at the review.

2. We have developed a method of objective molecular dynamics (OMD). This is an exact method of molecular dynamics -- every atom (typically infinitely many) satisfies exactly  $F=ma$  -- but only a few atoms need be simulated. (The time-dependent positions of other atoms are given by an explicit formula.) Certain kinds of macroscopic motions can be simulated. As an application of the method we have simulated the behavior of a (6,6) carbon nanotube pulled at constant macroscopic strain rate, one of the possibilities allowed by OMD. For the atomic forces we have used Tersoff potentials for carbon. We have been able to reach strain rates that are experimentally accessible, a rarity in molecular dynamics simulations. From a series of 50 simulations at various strain rates, we have obtained the following unexpected results:

Several modes of failure were observed, including fibrous fracture (the nanotube splits along its length), cavitation (holes open up in the side of the nanotube), cross-sectional collapse (the tube collapses into two parallel graphene strips), but in no cases have we observed the expected mode of failure of the propagation of Stone-Wales defects. Increasing strain rate and initial temperature paradoxically led to lower ductility, Figure 2. In those cases exhibiting failure at low strains ( $\sim 1\%$ ), failure was preceded by large amplitude vibrations of the cross-section at a frequency of about 100GHz.



4  
Fig 2. Strain at failure of (6,6) carbon nanotubes as a function of strain rate and temperature from 38 simulations

Examples of these large amplitude vibrations of the cross-section are seen in Figure 3 in two snapshots from a simulation at high strain rate and initial temperature of 500K. This also shows what could be called Stone-Wales partials, which however quickly healed and did not seem to contribute to plasticity or failure.

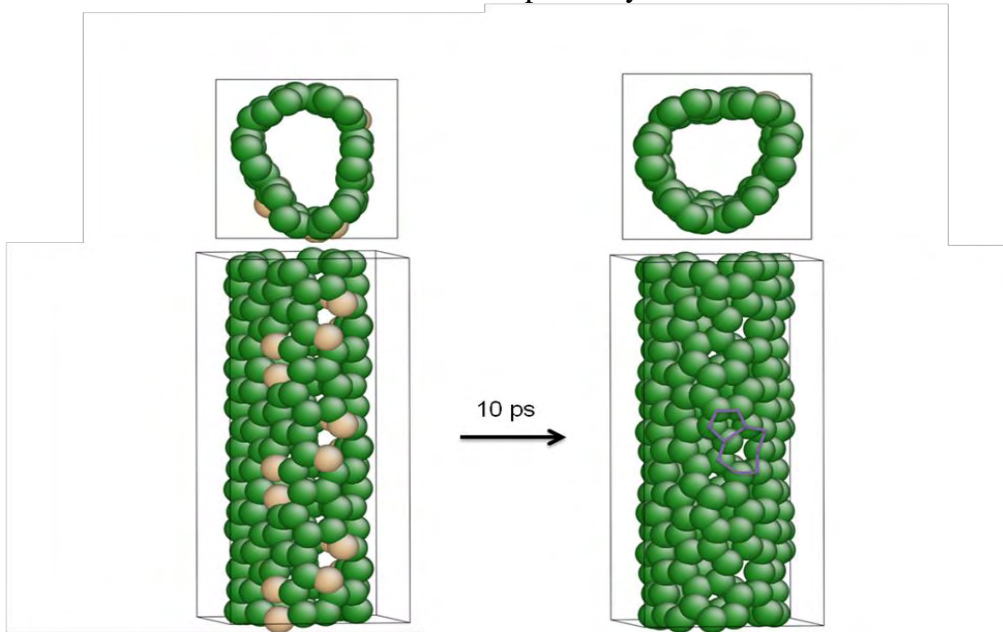


Fig. 3. Large amplitude vibrations of the cross-section of a carbon nanotube pulled at constant strain rate and initial temperature of 500K. The tan atoms show a loss of coordination and the formation of a 7-5 defect (Stone-Wales partial) which healed in 10ps.

Some results from our Objective Density Functional Theory codes are presented below. Fig 4 shows the electronic density of a structure which has reflection symmetries about the 3 principal planes. A 6<sup>th</sup> order differencing scheme, with a grid size of 0.2 a.u. and  $60^3$  gridpoints was used to solve the problem. Results (ground state energies, etc) compare well with KSSOLV (Planewave DFT Code developed at LBNL). For similar convergence parameters, CPU Times used by our code are significantly lesser compared to standard finite difference and plane-wave DFT codes.

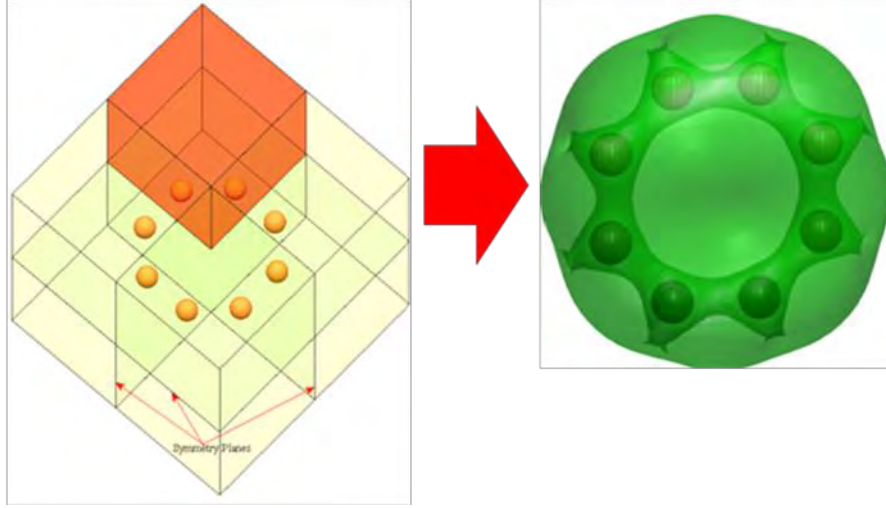


Fig 4: “Proof Of Concept” computation of electronic structure using the Objective DFT algorithm: Ring of 8 aluminum atoms using Heine Abarenkov Pseudopotential for Aluminum. The objective domain and two iso-surface levels of electronic density have been plotted.

Some results for the Objective Density Functional Theory algorithm for helical rods and nanotubes are also shown below in Fig 5. The results are from a pseudo-spectral code that was used for integrating the governing equations. We have developed techniques for automatically generating fundamental domains for these objective structures and our recent success has been the development of a spectral method that systematically exploits the underlying symmetries of these structures.

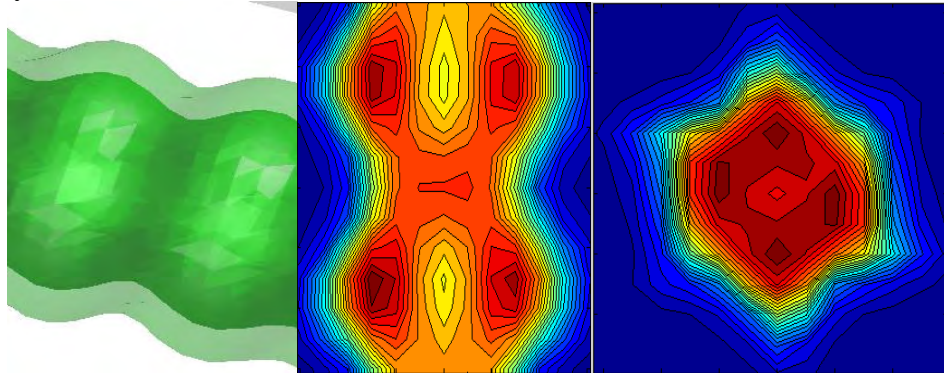


Fig 5: Left and Middle Images: Electronic charge density (two levels of iso-surfaces) and contours plotted over two fundamental domains for an Aluminum nanotube with a 5 degree angle of twist. Right Image: Charge density plot across the cross section of the same tube shows a large delocalized body of electrons. The results are from a pseudo-

spectral code that was used to solve Kohn-Sham equations with Bloch-like boundary conditions.

Our theoretical work on magnetic materials for the GameChanger project has suggested an interesting new material that achieves unusually strong magnetism as a consequence of a phase transformation. It is an alloy of NiCoMnSn realized recently in James' laboratory. A plot of magnetization vs. temperature is shown in Figure 4. Note the unusually strong magnetization in this alloy, nearly the strength of iron, in the high temperature austenite phase. A few degrees temperature change leads to a dramatic turning on/off of strong magnetism.

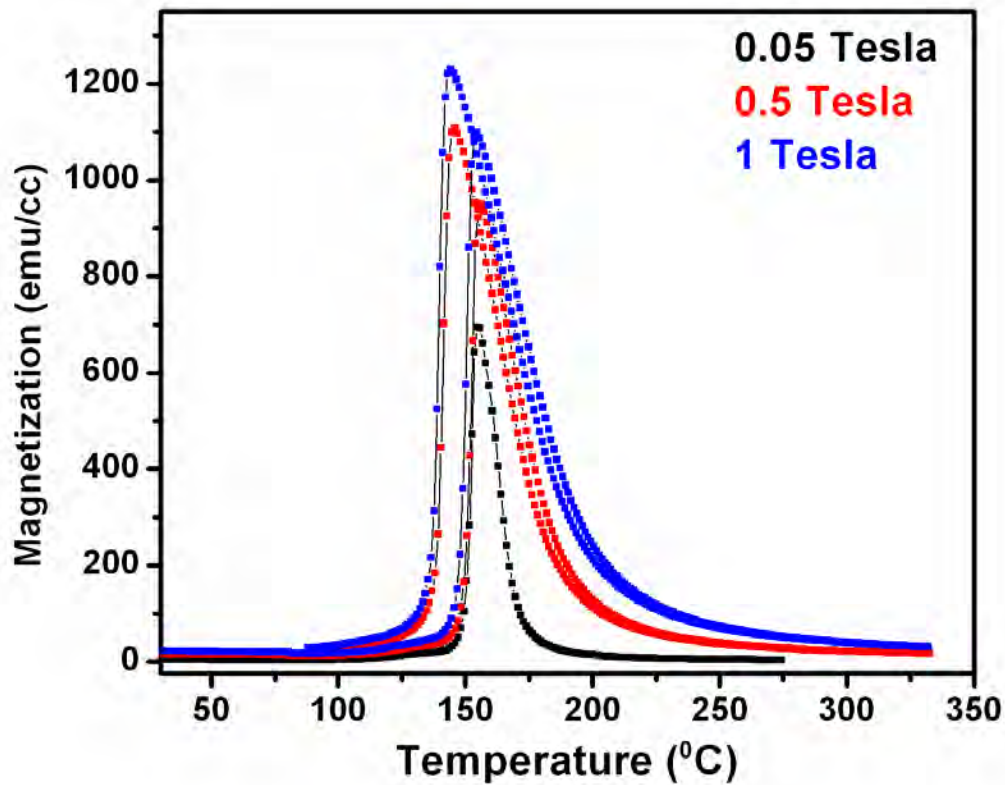


Fig. 6. Magnetization vs. temperature in an alloy of NiCoMnSn.